IS-T 1723

Magnetization studies of oxides related to the high temperature cuprate superconductors

by

Wang, Zhaorong

PHD Thesis submitted to Iowa State University

Ames Laboratory, U.S. DOE

Iowa State University

Ames, Iowa 50011

Date Transmitted: June 19, 1995

PREPARED FOR THE U.S. DEPARTMENT OF ENERGY

UNDER CONTRACT NO. W-7405-Eng-82.

DISCLAIMER

Magnetization studies of oxides related to the high temperature cuprate superconductors

by

Zhaorong Wang

A Dissertation Submitted to the

Graduate Faculty in Partial Fulfillment of the

Requirements for the Degree of

DOCTOR OF PHILOSOPHY

Department: Physics and Astronomy
Major: Condesed Matter Physics

Approved:

David C. Johnston
In Charge of Major Work

D K Finnemore
For the Major Department

For the Graduate College

Iowa State University
Ames, Iowa
1994

Magnetization studies of oxides related to the high temperature cuprate superconductors

Zhaorong Wang

Major Professor: David C. Johnston
Iowa State University

An Oxford Instruments Faraday magnetometer, capable of operating in the temperature range between 1.5 K and 1000 K, and magnetic field range between 0 T to 8 T, with a sensitivity of 3×10^{-8} cm^3G, was assembled and calibrated. The pumping station which supported this magnetometer was designed and built. Software for reducing the raw data and generating calibration files was written. The magnetic properties of several oxides related to the high temperature cuprate superconductors $BaCuO_{2+x}$, La_2CuO_4, Sr_2IrO_4, Sr_2RhO_4, Sr_2VO_4, and Sr_2CuO_3 were measured using the Faraday magnetometer.

AC and DC magnetization, neutron diffraction, and heat capacity measurements on polycrystalline $BaCuO_{2+x}$ revealed a combination of magnetic behaviors. The Cu_6 ring clusters and Cu_{18} sphere clusters in this compound were found to have ferromagnetic ground states with large spins 3 and 9, respectively. The Cu_6 rings ordered antiferromagnetically below the Néel temperature $T_N = 15 \pm 0.5$ Kelvin, whereas the Cu_{18} spheres remained paramagnetic down to 2 Kelvin. The ordered moment below T_N was 0.89(5) Bohr magnetons per Cu in the Cu_6 rings, demonstrating that quantum fluctuation effects are small in these atomic clusters. The Cu_{18} clusters are predicted to exhibit ferromagnetic intercluster order below about 1 Kelvin. Heat capacity C_P data for $BaCuO_{2+x}$ show a sharp second order transition at the Néel

temperature. The value of the discontinuity in the heat capacity at Néel is close to that expected for antiferromagentic ordering of the ring clusters, according to the mean field theory. An additional maximum in C_P at about 0.8 K may correspond to the ferromagnetic ordering of the sphere clusters postulated above. Understanding the magnetic behavior of $BaCuO_{2+x}$ is relevant to the pairing mechanism in high T_c cuprates.

Magnetic susceptibility measurements for $Sr_2CuO_{3\pm\delta}$ were made from 2 K to 800 K, and a strong dependence upon oxygen content (δ) was observed. High temperature magnetic susceptibility measurements for the sample with the smallest Curie-Weiss-type term clearly show the increase with temperature expected from the Bonner-Fisher model for a spin-1/2 one dimensional (1-D) Heisenberg antiferromagnet. This is the first direct experimental observation of 1-D magnetic behavior in this system. Estimates of the interchain magnetic magnetic interaction and low temperature neutron and synchrotron x-ray powder diffraction studies of Sr_2CuO_3 indicate that this material may be the best (nearly ideal) realization of a 1-D spin 1/2 Heisenberg antiferromagnet reported to date.

Magnetization studies of

oxides related to the high temperature cuprate superconductors

by

Zhaorong Wang

A Dissertation Submitted to the

Graduate Faculty in Partial Fulfillment of the

Requirements for the Degree of

DOCTOR OF PHILOSOPHY

Department: Physics and Astronomy
Major: Condesed Matter Physics

Approved:

_____
In Charge of Major Work

_____
For the Major Department

_____
For the Graduate College

Iowa State University
Ames, Iowa
1994

TABLE OF CONTENTS

LIST OF FIGURES

LIST OF TABLES

ACKNOWLEDGMENTS

I would like to express my deepest appreciation to my advisor Professor David C. Johnston for his guidance, patience, and understanding. His attitude of pursuing perfection as an experimentalist has had a revolutionary influence on both my professional and daily life.

I would also like to thank Dr. David Vaknin for introducing me to the $BaCuO_{2+x}$ problem, thank Drs. X.-L Wang and J. A. Fernandez-Baca for their support on neutron experiments, and thank all of them for many stimulating discussions.

I would also like to thank Drs. M. K. Crawford, T. Ami and their associates for their Sr_2CuO_3 and Sr_2IrO_4 samples and for stimulating discussion in analyzing the magnetic data.

I would also like to thank Dr. Norman E. Phillips, Dr. Robert A. Fisher and their associates for specific heat measurments of my $BaCuO_{2+x}$ sample, and their stimulating discussion.

I would also like to thank Dr. E. J. Ansaldo and Dr. T. Riseman for their measurement of my $Ba_{0.625}K_{0.375}BiO_3$ sample, and thank Drs. J. H. Cho, Z. D. Hao, J.R. Clem, V. Kogan, S. Mitra, and O. B. Hyun for stimulating discussion in analysis of magnetic data of that sample.

I would also like to thank Drs. H. Takeya, J. Moorman and K. A. Gschneidner,

Jr for making it possible for me to make AC susceptibility measurements in their group.

I would also like to thank A. V. Mahajan, J. H. Cho, F. Chou, L. L. Miller, and W. Lee for teaching me many basic experimental techniques, and thank B. K. Cho, S. Kondo, and S. Pace for numerous helpful discussions.

I would also like to thank K. M. Ho and C. T. Chan to let me use their work-station and softwares.

I would also like to thank Ames Lab. service department and Physics machine shop in helping me build the pumping station for the Faraday Magnetometer.

Ames Laboratory is operated for the U.S. Department of Energy by Iowa State University under Contract No. W-7405-Eng-82. This work was supported by the Director for Energy Research, Office of Basic Energy Sciences.

This thesis is dedicated to my father who passed away last year, my wife and our first baby who was born this year.

This work was performed at Ames Laboratory under Contract No. W-740t-eng-82 with the U.S. Department of Energy. The United States gavement has assigned the DOE Report number IS-T1723 to this thesis.

CHAPTER 1. INTRODUCTION

Due to the discovery of high temperature superconductivity [1] in 1986 in the La-Ba-Cu-O system and many related materials, for example the Y-Ba-Cu-O system [2], the traditional interpretation for the mechanism of superconductivity (electron-phonon interaction) is no longer clearly applicable. So it is a time to review basic properties and the existing theory of superconductors, a time to test these new superconductors with new ideas and new technologies, a time to try to find more new types of superconductors and find new properties and interpretation associated with these new materials.

This dissertation is designed to make an attempt to study some of these points, and is composed of three basic components: First the new technology, which is described in Chapter 2 (the Faraday Magnetometer chapter); second the new ideas, described in the Chapter 1 (introduction chapter); third the new materials, described in Chapter 4 (the $BaCuO_{2+x}$ chapter), 5 (the Sr_2CuO_3 chapter), and 6 (the Sr_2IrO_4 chapter).

This chapter includes a basic introduction to the thesis and a review of the basic properties of superconductors and the Ginzburg-Landau theory for superconductivity.

The superconductive state is characterized by several parameters, for example the penetration depth, correlation length, critical temperature, and critical field.

High temperature superconductors have distinctive parameters, such as high critical field, small coherence length, large penetration depth, and of course high critical temperature. Furthermore the temperature dependence of the penetration depth will give us information on whether a material is in the BCS clean limit, dirty limit, or follows the two-fluid model, or must be described by a non-BCS theory: the low temperature behaviour of the penetration depth versus temperature gives us information about whether the material is in an s-wave or d-wave state, which reflects the symmetry of the superconducting order parameter.

The magnetic penetration depth λ of $Ba_{0.625}K_{0.375}BiO_3$ was measured using both DC magnetization and μSR measurements. The temperature dependence of the magnetic penetration depth for both methods indicates conventional s-wave pairing with the isotropic extrapolated value $\lambda(0) = 3400$ $\AA$, similar to that of $La_{2-x}Sr_xCuO_4$ samples of the same superconducting transition temperature. However, as the temperature approaches the transition temperature, there is a significant difference between the magnetic penetration depth from these two methods, and a possible origin for the difference was postulated to be the magnetic field dependence of the penetration depth.

On the other hand, high temperature superconductors have their unique normal state behavior, spin one-half two-dimensional antiferromagnetism, and the structures of all known high transition temperature T_c cuprate superconductors contain CuO_2 planes. The strong antiferromagnetic (AF) coupling between the Cu spins in the CuO_2 planes of the undoped parent compounds of the high transition temperature cuprate superconductors results from an indirect 180^o bond angle Cu^{+2}-O^{-2}-Cu^{+2} superexchange interaction (J $\approx$ 500 K). It was argued that upon doping, an inter-

vening O^{-1} ion produced by a localized doped hole on the O^{-2} ion results instead in an indirect *ferromagnetic* (FM) interaction between the two adjacent Cu spins. The *ferromagnetic* interaction would result in magnetic frustration which may be relevant to the superconducting pairing mechanism in the high T_c cuprates. An alternative cause of the FM interaction has been predicted to be a change in the Cu^{+2}-O^{-2}-Cu^{+2} bond angle from 180^o to 90^o; however, the intermediate angle at which the crossover from AF to FM coupling occurs is unknown. Thus it is important to futher clarify the conditions under which FM versus AF Cu^{+2}-Cu^{+2} interactions occur in copper oxides.

Herein, we describe a detailed study of the magnetic properties of the compound $BaCuO_{2+x}$. The compound has a large body-centered-cubic unit cell ($a = 18.25$ Å) with a 90 formula units per unit cell. The cell contains 6 lone CuO_4 units, 8 Cu_6O_{12} ring clusters and 2 $Cu_{18}O_{24}$ sphere clusters formed from edge-shared CuO_4 units. From unpolarized and polarized neutron diffraction measurements combined with magnetization measurements, we find that $BaCuO_{2+x}$ exhibits a remarkable combination of novel magnetic behaviors. The Cu_6 and Cu_{18} clusters have ferromagnetic ground states with large spins $S_r = 3$ and $S_s = 9$, respectively. The Cu_6 rings exhibit long range antiferromagnetic intercluster order below $T_N = 15$ K, with no apparent magnetic coupling to the lone Cu ions or the Cu_{18} clusters. In contrast, these latter two species remain paramagnetic down to 2 K and interact antiferromagnetically. Extrapolation of the magnetic susceptibility $\chi(T)$ data below 2 K predicts that the Cu_{18} clusters should exhibit ferromagnetic intercluster order below ~ 1 K. Our results are relevant to many cuprate superconductors which show buckling of the CuO_2 planes and significant deviations of the Cu-O-Cu bond angle from 180^o.

By using a generalized ferrimagnetic model, the interaction strength between a sphere cluster ball and lone ion is found to be 1.2 meV. By applying the Van Vleck approximation to the Heisenberg model, a fit to the high temperature susceptibility data yielded the intrasphere coupling constant J_s = 38 K and intraring coupling constant J_r = 148 K. The exact magnetic susceptibility of the Cu_6 ring cluster was calculated by solving the Heisenberg model numerically, and the error bars for J_s and J_r gotten from the previous model were estimated.

The dimensionality appears to play an important role in high temperature superconducivity: all the high temperature cuprate superconductors contain two dimensional (2-D) CuO_2 planes. It is natural to ask if 1-D cuprates exhibit superconductivity. If they do, what is the T_C of these systems, and if they donot, why not? Sr_2CuO_3, which has CuO chains with no CuO_2 planes, becomes a superconductor after doping with a small amount of oxygen under pressure. Therefore it will be interesting to study in detail the magnetic behavior of this pure CuO chain material Sr_2CuO_3. Hopefully it will help us to understand the role of dimensionality in the magnetic properties of cuprates and its relation to the high T_C superconducting mechanism.

Therefore magnetic susceptibility measurements for $Sr_2CuO_{3\pm\delta}$ were made from 2 K to 800 K, and a strong dependence upon oxygen content (δ) was observed. Samples synthesized under oxygen, followed by various nitrogen treatments, exhibited markedly different Curie-Weiss-type terms, and we discuss possible origins for this behavior. High temperature magnetic susceptibility measurements for the sample with the smallest Curie-Weiss-type term clearly showed the increase with temperature expected from the Bonner-Fisher model for a spin-1/2 one-dimensional Heisenberg

antiferromagnet. This is the first direct experimental observation of 1-D magnetic behavior in this system. The in-chain superexchange coupling constant, as determined by a fit to the Bonner-Fisher model, is $|J|/k_B \approx 1300 \pm 200$ K, comparable to the values observed in the two dimensional layered cuprates. Estimates of the interchain magnetic interaction strength indicate that this material may be the best realization of a 1-D spin 1/2 Heisenberg antiferromagnet reported to date. Low temperature neutron and synchrotron x-ray powder diffraction studies of Sr_2CuO_3 indicate that the low temperature structure of this system has Immm space group symmetry, the same structure reported at room temperature, indicating that this material, in contrast to La_2CuO_4, does not ungergo any structural transformations upon cooling. The absence of crystallographic distortions precludes a magnetic anisotropy contribution from a Dzyaloshinsky-Moriya interaction, implying that Sr_2CuO_3 should be a nearly ideal spin 1/2 antiferromagnetic Heisenberg chain compound, in agreement with the magnetic susceptibility results. A search for the presence of long range three dimensional antiferromagnetic order by magnetic neutron powder diffraction at temperatures as low as 1.5 K was not successful, although we estimate an upper limit for the size of the ordered moment which could have been detected to be $\sim 0.1\ \mu_B$ per Cu^{+2} ion.

The discovery of high-temperature superconductivity in doped copper oxides, which in their insulating forms are nearly ideal two-dimensional spin-1/2 Heisenberg antiferromagnets, has stimulated great interest in finding additional examples of such magnetic systems. We find that Sr_2IrO_4, which has the K_2NiF_4 structure and should have a $5d^5$ low-spin (S = 1/2) electronic configuration, develops a ferromagnetic moment near 250 K. The small size of the remanent moment ($10^{-2}\ \mu_B$), and our

structural studies, however, imply that this is weak ferromagnetism which appears at the Néel temperature due to a Dzyaloshinsky-Moriya interaction, in a manner analogous to that seen in La_2CuO_4.

Basic Properties of Superconducting Materials

There are usually five basic properties associated with superconducting materials: zero resistivity, critical field, Meissner effect, isotope effect, and the Josephson effect, as follows.

1) The resistivity of a superconducting material drops to zero when the temperature goes below a certain point called the transition temperature T_c.

2) If an ellipsoidal shaped superconductor is placed into a magnetic field, the field not only will be excluded from superconductor, but also that field is expelled from an originally normal sample as it is cooled through the critical temperature. This latter phenomenon is called the Meissner effect.

3) If we increase the magnetic field in the superconducting state, after a critical point, the sample resistivity will become nonzero. That critical point is called the critical magnetic field, satisfying $H_C = [1 - (\frac{T}{T_c})^2]$. When the current density is above a critical value J_c the sample will also become normal because of the field generated by the current, where $J_c = J_0[1 - (\frac{T}{T_c})^2]$. These are the behaviors of a so-called type I superconductor and the critical magnetic field is also called the thermodynamic critical field. However there are three different critical fields of type II superconductors: H_{c1}, H_{c2}, and H_{c3}. In the range $H < H_{c1}$, the field is excluded from the superconductor except for close to the surface; when $H_{c1} < H < H_{c2}$, the field penetrates the superconductor in the form of quantized flux; when H_{c2}

$< H < H_{c3}$, the field completely occupies the superconductor except for near the surface. The thermodynamic critical field in a type II superconductor H_c is equal to $H_{c2}/(\sqrt{2}\kappa)$, where $\kappa = \frac{\lambda}{\xi}$, λ is the penetration depth and ξ is the coherence length as defined below.

4) Another important property of superconductors is the isotope effect, which says that the critical temperature T_c and the atomic mass M has the following relation: $T_c \propto M^{-\frac{1}{2}}$ (this is only followed by s-p metals, not by transition metals).

5) Josephson predicted [3] macroscopic quantum effects called Josephson effects. In the DC Josephson effect, the total tunneling current I across a SIS (superconductor-insulator-superconductor) junction would be determined by the change in phase of the order parameter across the junction. That leads to an important coherent behavior of the junction $I = I_0 \frac{sin(\pi\Phi/\Phi_0)}{\pi\Phi/\Phi_0}$ where Φ is the total magnetic flux in the junction, Φ_0 is the flux quantum $hc/2e$, and I_0 depends on the temperature and structure of the junction.

Many physical properties of a superconductor can be simply explained by using Maxwell's equations and the two fluid model yielding, for example, the London equations. The two fluid model treats a superconductor as a perfect conductor with magnetic permeability $\mu = 1$ and dielectric constant $\epsilon = 1$. One assumes that there are two kinds of current density in a superconductor, the normal electron current density $\mathbf{j_n}$ and the supercurrent density $\mathbf{j_s}$. Then the total current density will be $\mathbf{j} = \mathbf{j_n} + \mathbf{j_s}$. In this case, Maxwell's equations are:

$$\nabla \cdot \mathbf{E} = \frac{4\pi}{c}\rho \tag{1.1}$$

$$\nabla \times \mathbf{E} = -\frac{1}{c}\frac{\partial \mathbf{B}}{\partial \mathbf{t}} \tag{1.2}$$

$$\nabla \cdot \mathbf{B} = 0 \tag{1.3}$$

$$\nabla \times \mathbf{H} = \frac{4\pi}{c}(\mathbf{j}_n + \mathbf{j}_s) + \frac{1}{c}\frac{\partial \mathbf{E}}{\partial t} \tag{1.4}$$

and the continuity equation is

$$\frac{\partial \rho}{\partial t} + \nabla \cdot (\mathbf{j}_n + \mathbf{j}_s) = 0 \, . \tag{1.5}$$

The normal current should satisfy Ohm's law

$$\mathbf{j}_n = \sigma_n \mathbf{E} \, . \tag{1.6}$$

The supercurrent velocity $\mathbf{v_s}$ must satisfy Newton's second law

$$m\frac{d\mathbf{v}_s}{dt} = -e\mathbf{E} \, . \tag{1.7}$$

The supercurrent density can be written:

$$\mathbf{j}_s = -n_s e \mathbf{v}_s \tag{1.8}$$

where n_s is the number density of superconducting electrons. Using the following relation for the time derivative

$$\frac{d\mathbf{v}_s}{dt} = \frac{\partial \mathbf{v}_s}{\partial t} + \mathbf{v}_s \cdot \nabla \mathbf{v}_s \tag{1.9}$$

and by omitting the nonlinear terms and combining Eq. (1.7) - (1.9), we get

$$\frac{\partial \mathbf{j_s}}{\partial \mathrm{t}} = \frac{n_s e^2}{m}\mathbf{E} \, . \tag{1.10}$$

This is called the first London equation. By substituting this equation into Maxwell equation (1.2) we get

$$\nabla \times \mathbf{j}_s = -\frac{n_s e^2}{mc}\mathbf{B} \, . \tag{1.11}$$

This is called London's second equation. If we let $\alpha^2 = \frac{n_s e^2}{4\pi mc}$ and assume $\mathbf{j}_s$ is independent of time, use Maxwell equation (1.4) Eq. (1.11) and consider the $\mathbf{j}_n = 0$ case, one gets

$$\nabla^2 \mathbf{B} - \alpha^2 \mathbf{B} = \mathbf{0} \,. \tag{1.12}$$

By assuming that $\mathbf{B} = \mathbf{B}(\mathbf{z})$, we get $\frac{d^2\mathbf{B}}{d^2 z} - \alpha^2 \mathbf{B} = 0$. The solution for that equation is $\mathbf{B} = \mathbf{B}_0 \exp(-\alpha z)$. This says that the magnetic field cannot penetrate into the superconductor, except for a surface layer. The thickness of this layer $\frac{1}{\alpha}$ is called the London penetration depth λ_l.

There are two weak points in this model. λ_l is not dependent on external field, and λ_l is not dependent on the size of the sample. In order to overcome these two weaknesses, Ginzburg-Landau theory was introduced.

Ginzburg-Landau Theory for Superconductivity

Landau Theory

Landau theory [4] for second-order phase transitions said that the Gibbs free energy near T_c can be expanded in a power series in the order parameter ψ,

$$G(T, P, \psi) = G_o(T, P) + \alpha(P)(T - T_c)\psi^2 + C\psi^4 \,. \tag{1.13}$$

The equilibrium value of the order parameter can be obtained by minimizing the free energy with respect to ψ: $\psi = \sqrt{\frac{\alpha(T_c - T)}{2C}}$ for $T < T_c$ and $\psi = 0$ for $T > T_c$. Then

$$G = G_o - \frac{\alpha^2}{4C}(T_c - T)^2 \,, \; T > T_c \tag{1.14}$$

$$= G_o \,, \; T > T_c \,. \tag{1.15}$$

According to the definition of entropy $S = -(\frac{\partial G}{\partial T})$, one obtains $S = S_o$ $(T > T_c)$ and $S = S_o - \frac{\alpha^2}{2C}(T_c - T)$ (T < T_c). From thermodynamic theory we also get an expression for the specific heat C_p

$$C_p = T\left(\frac{\partial S}{\partial T}\right)_p = C_o(T)\,,\ T > T_c \tag{1.16}$$

$$= C_o(T) + \frac{\alpha^2 T}{2C}\,,\ T < T_c\,. \tag{1.17}$$

By subtracting these two formulae Landau theory predicts a discontinuity in specific heat at T_c given by

$$(C_p)_s - (C_p)_n = \frac{\alpha^2 T_c}{2C}\ . \tag{1.18}$$

In the presence of a magnetic field H, the free energy becomes $G' = G - H\psi$. By minimizing G' respect to ψ and neglecting the ψ^3 term, one obtains $H = 2\alpha(T - T_c)\psi$. From the definition of susceptibility, $\chi = \frac{\psi}{H}$, we get

$$\chi = \frac{1}{2\alpha(T - T_c)}\,. \tag{1.19}$$

Ginzburg-Landau Theory for Superconductivity

In order to extend Landau theory to the superconducting phase transition, Ginzburg and Landau [5] argued that the order parameter $\psi(r)$ corresponds to the superconducting wave function and therefore its square should be normalized to the density n_s of superconducting electrons. That is, $\psi^*(\mathbf{r})\psi(\mathbf{r}) = n_s(\mathbf{r})$, where $\mathbf{r}$ is the position. Ginzburg-Landau theory assumes that the free energy in the superconducting state G_s is

$$G(\mathbf{r})_s = G_n - \alpha'|\psi|^2 + (1/2)\beta|\psi|^4 + \frac{1}{2m^*}|(-i\hbar\nabla - \frac{q^*A}{c})\psi|^2 - \int_0^{Ba} M\cdot dB_a\ , \tag{1.20}$$

where G_n i sthe normal state free energy, according to the BCS theory, a Cooper pair has $m^* = 2m$, $n_s^* = n_s/2$, $e^* = 2e$, A is the vector potential which is defined as

$$\mathbf{B} = \nabla \times \mathbf{A} \,, \tag{1.21}$$

c is the speed of light and $\alpha' = \alpha(T_c - T)$. The gradient term comes from an increase in energy caused by a spatial variation of the order parameter. The integral term represents the increase in the superconducting free energy caused by the expulsion of magnetic flux from the superconductor.

The total superconducting free energy is

$$G_s = \int G_s(\mathbf{r}) d\mathbf{r} \,. \tag{1.22}$$

To minimize the free energy with respect to $\psi(\mathbf{r})$, one sets $\frac{\delta G_s}{\delta \psi} = 0$, yielding

$$[\frac{1}{2m^*}(-i\hbar\nabla - \frac{q^* A}{c})^2 - \alpha' + \beta|\psi|^2]\psi = 0 \,. \tag{1.23}$$

Also according to the usual quantum-mechanical definition,

$$j_s(r) = q^* v_s(\mathbf{r}) = -\frac{iq^*\hbar}{2m^*}[\psi^*\nabla\psi - \psi\nabla\psi^*] - \frac{q^{*2}}{m^2 c}\psi^*\psi A \,. \tag{1.24}$$

These are called the first and second Ginzburg-Landau equations.

Coherence Length

Now let us study the first Ginzburg-Landau equation for $\mathbf{B} = 0$, and $\mathbf{A} = 0$. If ψ only depends on z, this equation becomes:

$$-\frac{\hbar^2}{2m^*}\frac{d^2\psi}{dz^2} - \alpha'\psi + \beta|\psi|^2\psi = 0 \,. \tag{1.25}$$

If we assume that a real solution for ψ exists where ψ does not vary in space for $z \rightarrow \pm \infty$, we get $\psi_{\infty}^2 = \alpha'/\beta$. Defining $f = \frac{\psi}{\psi_{\infty}}$, the previous equation becomes

$$-\frac{\hbar^2}{2m^*\alpha'}\frac{d^2f}{dz^2} - f + f^3 = 0 \ . \tag{1.26}$$

Let $\xi = \sqrt{\frac{\hbar^2}{2m^*\alpha'}}$. Then

$$-\xi^2\frac{d^2f}{dz^2} - f + f^3 = 0 \ . \tag{1.27}$$

The solution is $f = \tanh(\frac{z}{\sqrt{2}\xi})$, the famous soliton solution [6].

If there is only one pair of electrons in the system, then its wave function is thus $\psi = \tanh(z/\sqrt{2}\xi)$. The size ξ of this Cooper pair is called the coherence length, and is a measure of the minimum distance over which the superpair wavefunction can decrease to zero.

If we consider dynamic processes, then we should add a time term into Eq. (1.27). The simplest way is to add a second derivative term:

$$\frac{d^2f}{dx^2} - \frac{d^2f}{d\tau^2} + f - f^3 = 0 \ , \tag{1.28}$$

where $x = z/\xi$ and $\tau = V\,t/\xi$ and V is the velocity of the soliton. It is a very famous nonlinear differential equation. It has a soliton solution:

$$f = \tanh[\frac{x-\tau}{\sqrt{2}}] \ . \tag{1.29}$$

The properties of this solution are as follows: 1) It does not change shape when it travels; 2) After two solitons go though each other their shapes do not change; 3) The interaction between solitons is not linear. For example when two solitons meet

each other the principle of superposition does not hold. This leads to the possibility of big fluctuations, which the BCS theory does not address.

CHAPTER 2. FARADAY MAGNETOMETER

Introduction

The Faraday magnetometer [7] has been widely used in many areas of scientific research, e.g., in biology [8], chemistry [9], and especially in physics [10]-[17]. In many cases the Faraday magnetometer has proved to be not only useful but also essential, for example in measuring the magnetic susceptibility under pressure [10] [9], combined magnetic susceptibility and thermogravimetric analysis [11] [12], high magnetic field and high temperature measurements [13], and fast flux magnetization relaxation measurements in superconductors [14].

The research we are interested in requires using a magnetometer to measure the superconducting and normal state properties of high T_C superconductors. Determining the normal state properties is crucial in order to establish a basis to understand the mechanism of high temperature superconductivity. The exchange interaction strength between the Cu spins of cuprates is about 1500 K. Therefore one needs to characterize the high temperature ($>>$ 300 K) magnetic properties. In addition, H_{c2} ($T = 0$) for most high T_C materials is above 10 T. The Faraday magnetometer we installed is capable of temperatures to 1000 K and magnetic fields up to 8 Tesla.

The Faraday magnetometer technique is based on measuring the force on a magnetic dipole moment $\vec{m}$ in an external inhomogeneous magnetic field. Consider

a general case with

$$\vec{m} = m_x\vec{i} + m_y\vec{j} + m_z\vec{k} \tag{2.1}$$

$$\vec{B} = B_x\vec{i} + B_y\vec{j} + B_z\vec{k}\,, \tag{2.2}$$

where $\vec{B}$ is the magnetic field at the position of the sample. The potential energy U of $\vec{m}$ is

$$U = -\vec{m}\cdot\vec{B}\,, \tag{2.3}$$

and the force on $\vec{m}$ is

$$\vec{F} = -\nabla U\,. \tag{2.4}$$

Inserting Eq. (2.3) into (2.4) and expanding in Cartesian coordinates, we get

$$\vec{F} = \frac{\partial(m_xB_x + m_yB_y + m_zB_z)}{\partial x}\vec{i} + \frac{\partial(m_xB_x + m_yB_y + m_zB_z)}{\partial y}\vec{j} + \frac{\partial(m_xB_x + m_yB_y + m_zB_z)}{\partial z}\vec{k}\,. \tag{2.5}$$

In our case only the vertical (z) component of the force can be detected and we assume the magnetic dipole moment to be homogeneous over the sample volume, so that

$$F_z = m_x\frac{\partial}{\partial z}B_x + m_y\frac{\partial}{\partial z}B_y + m_z\frac{\partial}{\partial z}B_z\,. \tag{2.6}$$

In the Faraday technique, the magnetic induction $\vec{B}$ is designed to vary only in the z direction across the sample volume. Therefore, we neglect the first two terms in the previous equation and the force becomes

$$F_z = m_z\frac{\partial}{\partial z}B_z\,. \tag{2.7}$$

A sketch of the Oxford Instruments Faraday magnetometer is shown in Fig. 2.1.

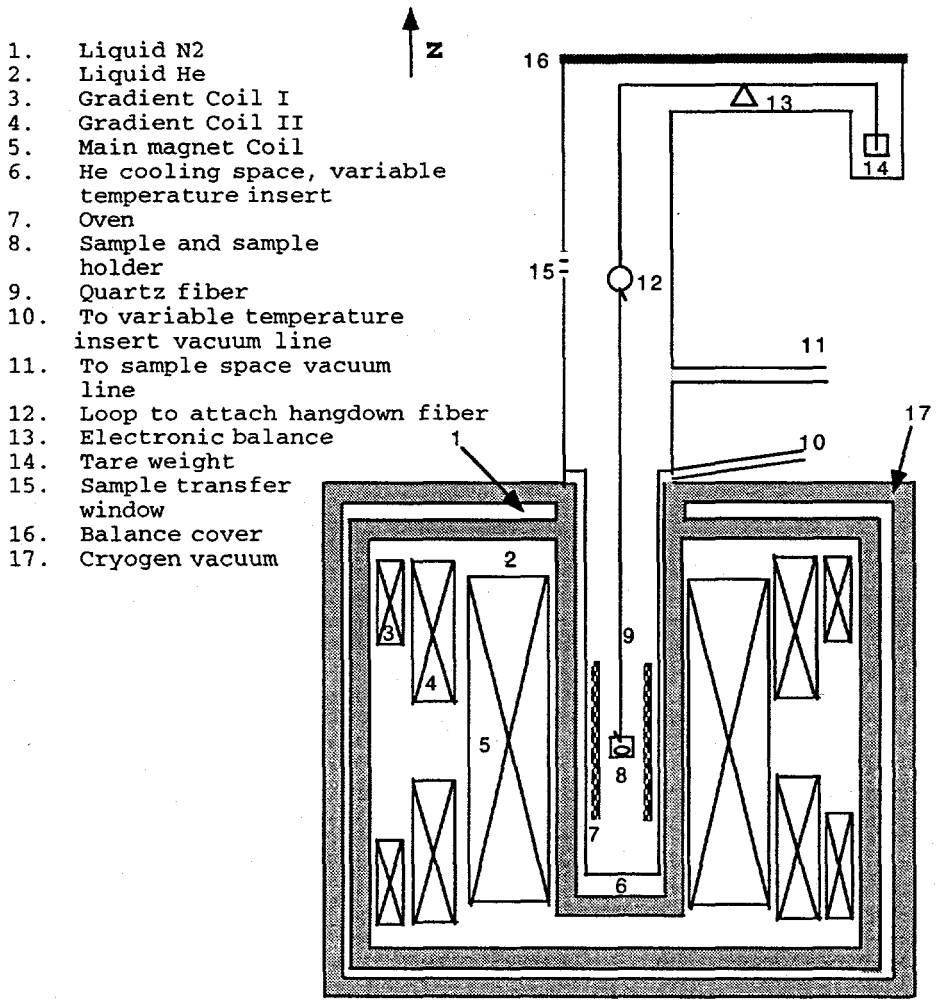

Figure 2.1: Sketch of the Oxford Instruments Faraday magnetometer

Sensitivity

The Faraday method is one of the oldest ways for measuring static magnetization. Modern vacuum microbalances and superconducting magnets make it possible for the Faraday magnetometer to compete with SQUID magnetometers in terms of sensitivity. The Oxford Faraday magnetometer uses a Sartorius electronic vacuum microbalance with resolution $\Delta m = 0.1$ μg and maximum capacity 3 g, a superconducting solenoid with a field of up to 8 T and a superconducting quadrupole-type coil [18] enabling field gradients of up to 30 T/m to be generated. For spins 1/2 a B/T ratio of 3 T/K is needed to saturate the spins within 1% at 2 K, and the 8 T field available with the Oxford Instruments Faraday magnetometer satisfies that criterion.

The sensitivity of the system is easily computed. Assume that the lowest magnetic moment that can be detected is M_z. From Eq. (2.7),

$$M_z = \frac{F_z}{\frac{dB}{dz}} \, . \tag{2.8}$$

Since $F_z = (\Delta m)$g, where g = 980.5 cm/s^2, one has

$$M_z = \frac{\Delta mg}{\frac{dB}{dz}} \, . \tag{2.9}$$

Inserting the minimum detectable $\Delta m = 0.1$ μ g and maximum field gradient $\frac{dB}{dz}$ = 3000 G/cm into Eq. (2.9) yields the resolution in magnetization $M_z = 3 \times 10^{-8}$ cm^3 G. In units of Bohr magnetons μ_B,

$$M_z = \frac{3 \times 10^{-8} cm^3 G}{(9.27 \times 10^{-21} \, cm^3 G/\mu_B)} = 3 \times 10^{12} \ \mu_B \, , \tag{2.10}$$

which corresponds to 3×10^{12} spin 1/2 impurity ions with saturated moments of 1 μ_B. If we consider a matrix of Pt with atomic weight W = 196 g/mole, we have

$\frac{6.023\times10^{23}}{196} = 3.07 \times 10^{21}$ Pt atoms in one gram of Pt. The ratio of the minimum detectable number of impurity spins to Pt atoms in 1 g of Pt is therefore

$$\frac{3 \times 10^{12}}{3.07 \times 10^{21}} = 1 \times 10^{-9} . \tag{2.11}$$

This ratio corresponds to 0.001 at. ppm of saturated spin 1/2 ions in a Pt matrix. The Quantum Design SQUID magnetometer has a magnetic moment sensitivity of 10^{-8} cm^3 G. Thus our Faraday magnetometer has comparable sensitivity (3×10^{-8} cm^3 G). In addition this system is capable of operation from 1.5 K to 1000 K and with applied magnetic fields from 0 T to 8 T, which exceed the corresponding ranges (1.5 K to 400 K; 0 to 5.5 T) of our SQUID magnetometer. These enhanced ranges justify the extra effort to run this system compared to a commercial SQUID magnetometer.

Pumping Station

The Faraday magnetometer is composed of three main parts; first an electronic cabinet accommodating power supplies, temperature controllers, and a data acquisition system; second a cryogenic system and the balance; third a vacuum control unit, including pumping facilities, vent valves and vacuum gauges.

The pumping station part of the Faraday magnetometer is homemade here in Iowa State University and Ames Laboratory. The author considered available pump facilities, the needs of the system, and availability of commercial pumping stations, and optimized the system according to these factors. Due to the special requirements of the Faraday magnetometer, we needed to design a special multipurpose vacuum pumping station, and at the same time to get an optimal plan in terms of both budget

and function of the station.

There are two special components of this pumping station. First, the high vacuum part requires a vacuum of 10^{-6} to 10^{-8} torr, with a pumping speed of roughly 80 l/s at 10^{-4} torr. Second, the helium pumping system is high throughput to allow the vapor pressure and hence the temperature of the liquid helium in a large bath cryostat to be reduced below 1 atmosphere (4.2 K). The pumping speed should be about 700 l/min at pressures between 0.1 torr (corresponding to about 1 K) and 760 torr (corresponding to 4.2 K) [21].

The available Duo-Seal 1398 mechanical pump has a pumping speed of 1500 l/min at a pressure between 10^{-1} torr and 1 atmosphere, which is more than the required speed 700 l/min (11.7 l/s) in the same pressure range. However there is a long distance between the pump and our Faraday magnetometer, so we need to consider the conductance between the pump and the Faraday balance. The pumping speed is defined as the volume of gas per unit of time $\frac{dV}{dt}$ which the pumping device removes from the system at the pressure existing at the inlet to the pump.[19] The pumping speed S_F at the Faraday magnetometer, connected by a conductance C to a pump having a pumping speed S_P, is given by

$$\frac{1}{S_F} = \frac{1}{S_P} + \frac{1}{C} \,. \tag{2.12}$$

When conductances are connected in series, the total conductance C_t is given by

$$\frac{1}{C_t} = \frac{1}{C_1} + \frac{1}{C_2} + \frac{1}{C_3} + \ldots \quad . \tag{2.13}$$

For the mechanical pump the pumping speed is almost constant between 10^{-1} and 760 torr. The conductance C on the other hand is proportional to the pressure in most of this pressure range (viscous flow range), but approaches a constant as the

pressure reaches about 10^{-1} torr or less (molecular flow range). Therefore if the lowest conductance (molecular flow range) meets our requirements then the pumping speed will be sufficient over the entire operating pressure range. Therefore we use the molecular flow conductance to estimate the mimimum pumping line diameter.

In the molecular flow limit the conductance for a long tube of constant cross section follows the Knudsen formula [20]:

$$C = 3.81(T/M)^{1/2} D^3/L \text{ (liter/sec)}, \tag{2.14}$$

where D(cm) is the diameter of the tube, L(cm) is the length of the tube, C(liter/sec) is the conductance, T is the absolute temperature, and M is the molecular weight of the gas pumped in g/mole. At room temperature $T = 293$ K and for He gas $M = 4$. This formula is independent of the pressure because in the Knudsen regime the molecules pass through the long tube without colliding with each other.

In the molecular flow range the conductance for an elbow is between [19]

$$C = 3.81(T/M)^{1/2} D^3/[L_1 + L_2 + 1.33D] \tag{2.15}$$

and

$$C = 3.81(T/M)^{1/2} D^3/[L_1 + L_2] \ , \tag{2.16}$$

where L_1 and L_2 are the arm lengths of this elbow. So when

$$L_1 \textit{ and } L_2 >> 1.33\ D \ , \tag{2.17}$$

we may omit the $1.33D$ in Eq. (2.15), and use Eq. (2.14) with total tube length $L = L_1 + L_2$. In our case $L \approx 8$ meters, and we now need to know what pumping line diameter (D) should be chosen to satisfy the pumping speed requirement. From Eq.

(2.14) for He one finds $C = 42.69$ (l/s) for $D = 4$ inches, and $C = 5.33$ (l/s) for $D = 2$ inches. If we use the Duo-Seal 1398 mechanical pump with $S_P = 25$ (l/s), then $S_F = 15.77$ (l/s) for $D = 4$ inches, and $S_F = 4.39$ (l/s) for $D = 2$ inches. Therefore $D = 4$ inches will be a reasonable choice (see Fig. 2.2).

For the high vacuum pumping station (1×10^{-6} torr), diffusion pump stations and turbo-molecular pumping stations are available. The advantages of a diffusion pumping station are reliability and cost. But the disadvantages are a worse vacuum limit compared to the vacuum limit (10^{-10} torr) that can be reached by a turbo-molecular pump, the presence of oil vapor, and the necessity of a liquid nitrogen cold trap. For a turbo-molecular pump the time to pump from one atmosphere to 10^{-6} torr is much less than for a diffusion pump. So generally speaking a turbo-molecular pump has better performance than an oil diffusion pump. However the maximam magnetic field a turbo-molecular pumping station can stand is about 100 G. In order to match this condition we need to separate the pump from the Faraday magnetometer by at least 2 meters. This separation will reduce the effective pumping speed considerably. Therefore we decided to use a diffusion pump station. We compared the products from Varian, Balzers, Edwards, Alcatel, and Veeco, and chose the Veeco VR-3000 diffusion pump station. The layout of the pumping lines is schematically illustrated in Fig. 2.2.

Faraday Magnetometer Operation

Introduction

The operation of the Faraday magnetometer can be summarized into the following five steps.

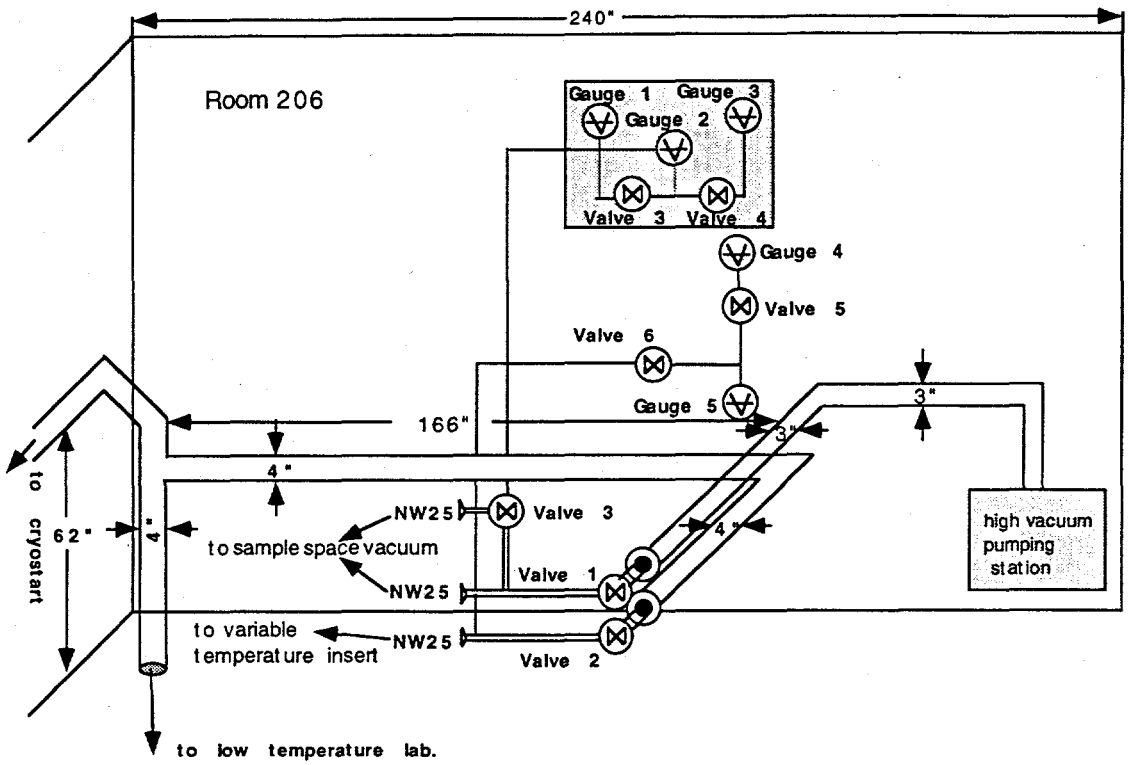

Figure 2.2: The pumping diagram for the Faraday magnetometer. The pump system in room A-206 consists of two separate pumping systems. The pump in the low temperature lab is connected to the variable temperature insert through valve 2. The high vacuum pumping station in room A 206 is connected to the sample space through valves 1 and 3. The pressure in the sample space is monitored by gauges 1, 2, and 3. The pressure in the variable temperature insert space is monitored by gauges 4 and 5.

1) The sample weight must be less than 3 g, which is the maximum capacity of the microbalance. The diameter of the sample must be less than 1/2 inch. The sample mass is also limited by the maximum force it will exert on the balance in the experimental magnetic field and magnetic field gradient; the maximum force should be 55 mg for the 100 mg range and 10 mg for the 10 mg range. The sample mass should be measured before and after each measurement. Balance drift due to buoyancy effects is not a factor in the magnetization measurements, since the method of taking the data corrects for balance drift (see below).

2) The sample and sample holder (if any) are suspended with a 22 1/4 inch quartz fiber. The sample holder is usually a quartz bucket or a thin pure gold wire. The sample holder contribution should be premeasured and later subtracted from the raw data.

3) Extra care should be taken when loading the sample because of the delicate nature of the quartz fiber. The balance should be tared to read 0 mg for the 10 mg range and 45 mg for the 100 mg range. The centering of the sample should be checked. The sample space should be evacuated by using the high vacuum pumping station to 10^{-6} torr for 12 hours, and refilled with He gas to the pressure required.

4) The data taking process is controlled by software provided by Oxford Instruments. The raw data should be reduced using software "convert.exe" (see below), and the calibration data file "zrwcalif.dat" (see below).

5) The Faraday magnetometer should be kept filled with liquid N_2 and liquid He all the time that the magnetometer is operated.

The standard sample we used was the NIST pure Pt sample, with atomic weight 195.09 g/mole, density 21.54 g/cm^3, and molar volume 9.057 cm^3/mole. The cali-

brations were done at room temperature. The range of gradient field was from 0 to 30 T/m, with a main field range from 0 to 8 T. At room temperature $T = 297$ K, the susceptibility of Pt is $\chi(\mathrm{Pt}) = 0.991 \times 10^{-6}$ cm^3/g. The standard sample we measured has mass 196.57 mg. For this sample, $\chi = 1.948 \times 10^{-7}$ cm^3. Let the field equal to 1 T which is 10^4 G, then the magnetic moment becomes $M = 1.948 \times 10^{-3}$ (cm^3 G). Now if we apply a gradient field $\frac{dB}{dz} = 10$ T/m $= 1000$ G/cm, then the force should be:

$$\begin{aligned} F(\mathrm{dyne}) &= M(\mathrm{cm}^3\ \mathrm{G})\frac{dB}{dz}(\frac{\mathrm{G}}{\mathrm{cm}}) = 1.946\ (\mathrm{dyne}) \\ F(\mathrm{newton}) &= M(\mathrm{A\ m}^2)\frac{dB}{dz}(\frac{\mathrm{T}}{\mathrm{m}}) = 1.946 \times 10^{-5}\ (\mathrm{newton})\ . \end{aligned} \tag{2.18}$$

Therefore by measuring the force on the sample at a known field gradient we can get the sample magnetic moment $M = F/\frac{dB}{dz}$.

Magnetic Moment Measurement Sequence

The measurement sequence is designed to take balance drift into account. The Oxford six point sequence is to first set the gradient $\frac{dB}{dz}$ to zero, measure the force at time t_1, $F(t_1)$, second measure the force at positive gradient $F(t_2)$, third measure the force at zero gradient again $F(t_3)$, fourth measure the force at the zero gradient $F(t_4)$, fifth measure the force at negative gradient $F(t_5)$, sixth measure the force at zero gradient field $F(t_6)$. The final formula for the force is:

$$\begin{aligned} 2F = F(t_2) - [\frac{F(t_3) - F(t_1)}{t_3 - t_1}(t_2 - t_1) + F(t_1)] \\ -F(t_5) + [(\frac{F(t_6) - F(t_4)}{t_6 - t_4}(t_5 - t_4) + F(t_4)]\ . \end{aligned} \tag{2.19}$$

The relationship between the gradient coil current in Amperes, I_G, and the field gradient dB_z/dz, is defined as

$$\frac{dB_z}{dz} = \frac{I_G}{calif} , \tag{2.20}$$

where $calif$ is a calibration factor which is 0.0341 A cm/G at low fields.

For example, a data file for the Pt sample at $T = 297$ K is listed in Table 2.1. For these data, $H = 70000$ G and

$$\frac{dB}{dz} = \frac{33 \text{ A}}{0.0341 \left(\frac{\text{A cm}}{\text{G}}\right)} = 968 \frac{\text{G}}{\text{cm}} . \tag{2.21}$$

From Table 2.1 and Eq. (2.19) we get $F = 13.78$ dyne. From Eq. (2.8) the sample magnetic moment is then

$$M = \frac{F}{\frac{dB}{dz}} = \frac{13.78 \text{ dyne}}{967.7 \text{ G/cm}} = 1.423 \times 10^{-2} \text{ cm}^3\text{G} . \tag{2.22}$$

Therefore the sample susceptibility is

$$\chi(\text{cm}^3) = \frac{M \text{ (cm}^3\text{G)}}{H \text{ (G)}} = 2.033 \times 10^{-7} \text{ cm}^3$$

$$\chi(\text{m}^3) = \frac{M \text{ (Am}^2\text{)}}{H \text{ (A/m)}} = 2.327 \times 10^{-12} \text{ m}^3 , \tag{2.23}$$

and gram susceptibility is

$$\chi_g = \frac{\chi}{M_{\text{Pt}}} = 1.034 \times 10^{-6} \frac{\text{cm}^3}{\text{g}} . \tag{2.24}$$

Units

The data file generated by the Oxford Instruments software gives a susceptibility in SI volume units. The relation between the molar susceptibility in CGS units and

Table 2.1: A Faraday magnetometer raw data file for a Pt sample of mass 196.57 mg, where g = 980.5 cm/s^2

Time (seconds)	Gradient Current (A)	Force/g (gram)	Magnetic field (T)
162222	+0.0000	0.00051400	7.000
162248	+33.0000	0.01457300	7.000
162272	+0.0000	-0.00051700	7.000
162310	+0.0000	+0.00023000	7.000
162334	-33.0000	-0.01381200	7.000
162360	+0.0000	+0.00022700	7.000

Table 2.2: The Faraday magnetometer data file (for H = 2000 G G = 3 A) for Pt with different units

B external (T)	0.200000	B external (G)	2000
Gradient (T/m)	0.880	Gradient (G/cm)	88.0
H (A/m)	1.592×10^{5}	H (oersted)	2000
Temperature (K)	297.00	Temperature (K)	297.00
Force (N)	3.260×10^{-7}	Force (dyne)	3.260×10^{-2}
M (volume) (A/m)	40.60	M (volume) (G)	0.0406
χ (volume)	$+2.546\ 10^{-4}$	χ (volume)	$2.027\ 10^{-5}$

the volume susceptibility in SI units is

$$\chi(\frac{cm^3}{mole}) = \chi(\text{volume})\,\frac{1}{4\pi}\,V_M(\frac{\text{cm}^3}{\text{mole}})\,, \tag{2.25}$$

where V_M is the molar volume. Therefore the volume susceptibility for Pt in SI units is

$$\begin{aligned}\chi &= \frac{4\pi\chi(\frac{\text{cm}^3}{\text{mole}})}{V_M(\frac{\text{cm}^3}{\text{mole}})} \\ &= \frac{4\pi[0.991\times10^{-6}(\text{cm}^3/\text{g})][195.09\ (\text{g/mole})]}{9.057(\text{cm}^3/\text{mole})} \\ &= 2.682\times10^{-4}\ (\text{dimensionless})\ .\end{aligned} \tag{2.26}$$

Table 2.2 gives examples of conversions between SI units and CGS units for various variables.

Sample Holder Contribution and Demagnetization Factor

For our standard sample we did not use any sample holder except the long quartz fiber. The error introduced by the long quartz fiber is less than 1 % (discussed below).

For the Ta sample we used a quartz bucket, which will give us a relatively large signal, and we will discuss this case in this section. A magnetization versus magnetic field curve was measured for the sample holder along with the long quartz fiber. The $\frac{M}{H} = \chi$ versus H plot shows an up-turn in the low field range, which can be fitted to

$$\chi = \frac{c1}{H - c2} + \chi o\ . \tag{2.27}$$

For the sample holder used with the Ta sample we get

$$\chi = \frac{0.141\times10^{-8}\text{G cm}^3}{H + 557(\text{G})} - 3.95\times10^{-8}\ \text{cm}^3\ . \tag{2.28}$$

The Ta magnetic data were corrected with that expression.

Above, we omitted the influence of the demagnetization factor N_d on the computed susceptibility. This is, we assumed that the magnetic field internal to the sample, H, is equal to H_a, where H_a is applied magnetic field. In order to estimate the error associated with this approximation, we use the formula:

$$H = H_a + N_d M \ . \tag{2.29}$$

In the case of Table 2.2, $M = 3.592 \times 10^{-4}$ (cm^3 G), and the volume magnetization is

$$M = 3.592 \times 10^{-4} (\mathrm{cm}^3 \mathrm{G}) \frac{\text{density}}{\text{mass}} = 0.040 \text{ G} \ . \tag{2.30}$$

Therefore,

$$H = H_a + N_d M = 2000.16 \text{ G} \ , \tag{2.31}$$

where we assume $N_d = 4\pi/3$. Therefore it is a good approximation to omit the demagetization factor correction in this case.

Calibration of Gradient Magnetic Field

The Faraday magnetometer has two superconducting coils, the main field solenoid and the gradient field coil. These two coils affect each other in the high field range, resulting in nonlinearity between the electric currents passed through the coils and the magnetic fields caused by those currents. The way that Oxford uses to correct this effect is to fit the gradient coil magnetic field gradient versus magnetic field applied by the main solenoid to a bipolynomial which is determined from calibration experiments.

Now let us consider the gradient field calibration in detail. We need to determine the dependence of the calibration factor, $calif$, in Eq. (2.20) on magnetic field H and magnetic gradient $G = dH/dz$. We assume the calibration factor is dependent on the field as well as the field gradient, so we need to calculate $calif(H, I_G)$ as a function of H and I_G,

$$calif(H, I_G) = a + bH + cH^2 + dHI_G + eI_G + f(I_G)^2 \qquad (2.32)$$

where a, b, c, d, e, and f are constant coefficients. However there is still an error associated with the fitting, and this error sometimes will reach as high as 5 to 10 percent depending on the range of H we select to fit.

Therefore the author developed an alternative program named "convert.bas" which numerically calculates the values of $calif(H, I_G)$ and stores them in a data file called "zrwcalif.cal". In order to explain the process we use the data file for the Pt sample of mass 196.57 mg in Table 2.1 as an example where H = 70000 G and I_G = 33 A. Using the standard (NIST) value for the susceptibility $\chi = 0.991 \times 10^{-6}$ cm^3/g, one predicts

$$M = \chi H = 1.364 \times 10^{-2} \text{ cm}^3 \text{ G} . \qquad (2.33)$$

Using Eqs. (2.18) and (2.20), the calibration factor is found to be

$$calif = \frac{I_G\, M}{F} = \frac{(33 \text{ A})\,(1.364 \times 10^{-2}\ cm^3\ G)}{13.77 \text{ dyne}} = 0.03268 \text{ A cm/G} \qquad (2.34)$$

instead of 0.0341 cited above. Using the same process for different H and I_G, one obtains the array $calif(H, I_G)$. As noted above, the software stores the array in a calibration file called zrwcalif.cal.

When the software analyzes the data for an arbitrary Faraday magnetometer experiment, it looks for the calibration factors from the calibration file stored previously in zrwcalif.cal. If the values of H and I_G do not match the values in the calibration data file zrwcalif.cal, the software calculates $calif(H, I_G)$ by using a linear interpolation formula, according to the values of the calibration factor at the four nearest locations where the calibration factors are known, $calif(H1, I_G1)$, $calif(H1, I_G2)$, $calif(H2, I_G1)$, $calif(H2, I_G2)$:

$$calif(H, I_G) = calif(H, I_G1) + \frac{calif(H, I_G2) - calif(H, I_G1)}{I_G2 - I_G1}(I_G - I_G1) \ , \quad (2.35)$$

where

$$calif(H, I_G1) = calif(H1, I_G1) + \frac{calif(H2, I_G1) - calif(H1, I_G1)}{H2 - H1}(H - H1) \quad (2.36)$$

$$calif(H, I_G2) = calif(H1, I_G2) + \frac{calif(H2, I_G2) - calif(H1, I_G2)}{H2 - H1}(H - H1) \ .$$

Therefore the the magnetization (CGS) of the sample is:

$$M(H, G) = \frac{F(H, G)(\text{dyne})}{I_G \ (\text{A})/[calif(H, I_G)(\text{A cm/G})]} \ . \quad (2.37)$$

A calibration data file zrwcalif.cal was generated using a standard Pt sample from NIST. The obtained calibration factors are plotted versus H and I_G in Fig. 2.3. The software and the calibration file were tested against several different standard samples (Ta, Al, Pt, and Pd). For the Ta sample, the maximum difference in susceptibility for different (H, I_G) values from (0.2 T, 3.41 A m/T) to (6 T, 13.64 A m/T) is 8 percent if the software with a constant calibration factor is used, but is only is 1 percent if the zrwcalif.cal calibration file is used, as shown in Figs. 2.4 and 2.5 respectively.

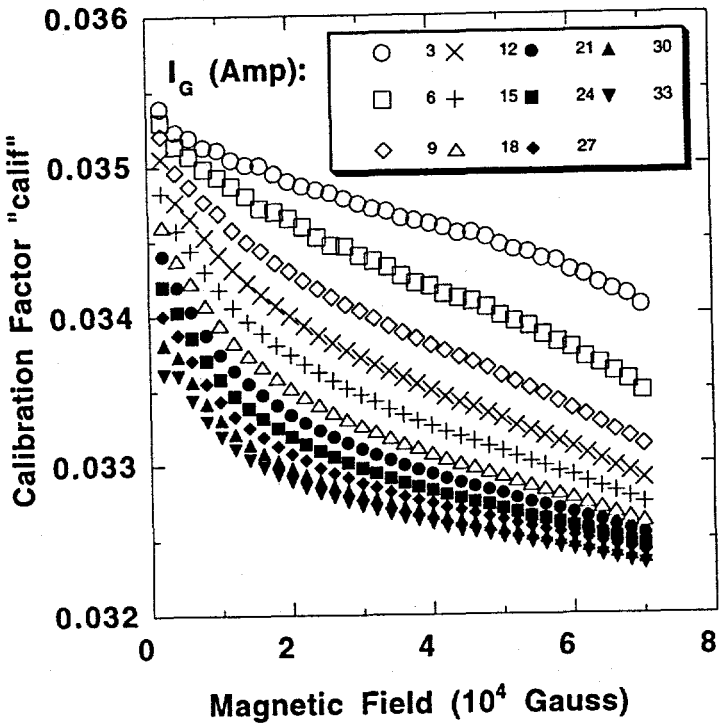

Figure 2.3: The calibration factor calif versus magnetic field at different gradient coil currents for the calibration data file zrwcalif.cal, where the symbols represent the value of gradient coil current I_G.

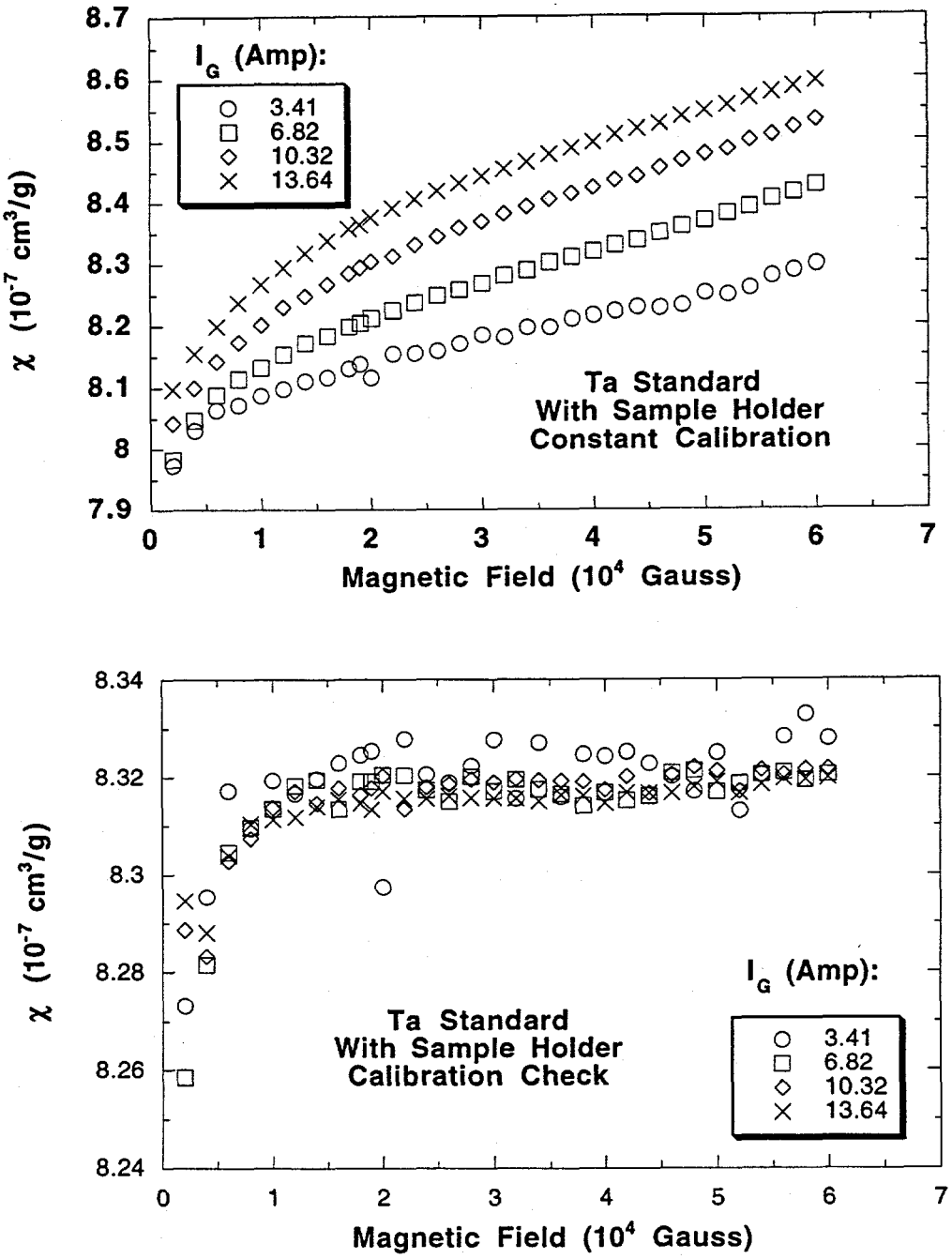

Figure 2.4: (a) The susceptibility determined according to constant calibration factor calif = 0.0341 versus magnetic field at different gradient fields for a standard Ta sample and its sample holder. (b) The susceptibility, determined according to calibration file zrwcalif.cal, versus magnetic field at different gradient fields for a standard Ta sample and its sample holder. The symbols represent various values of the gradient coil current I_G.

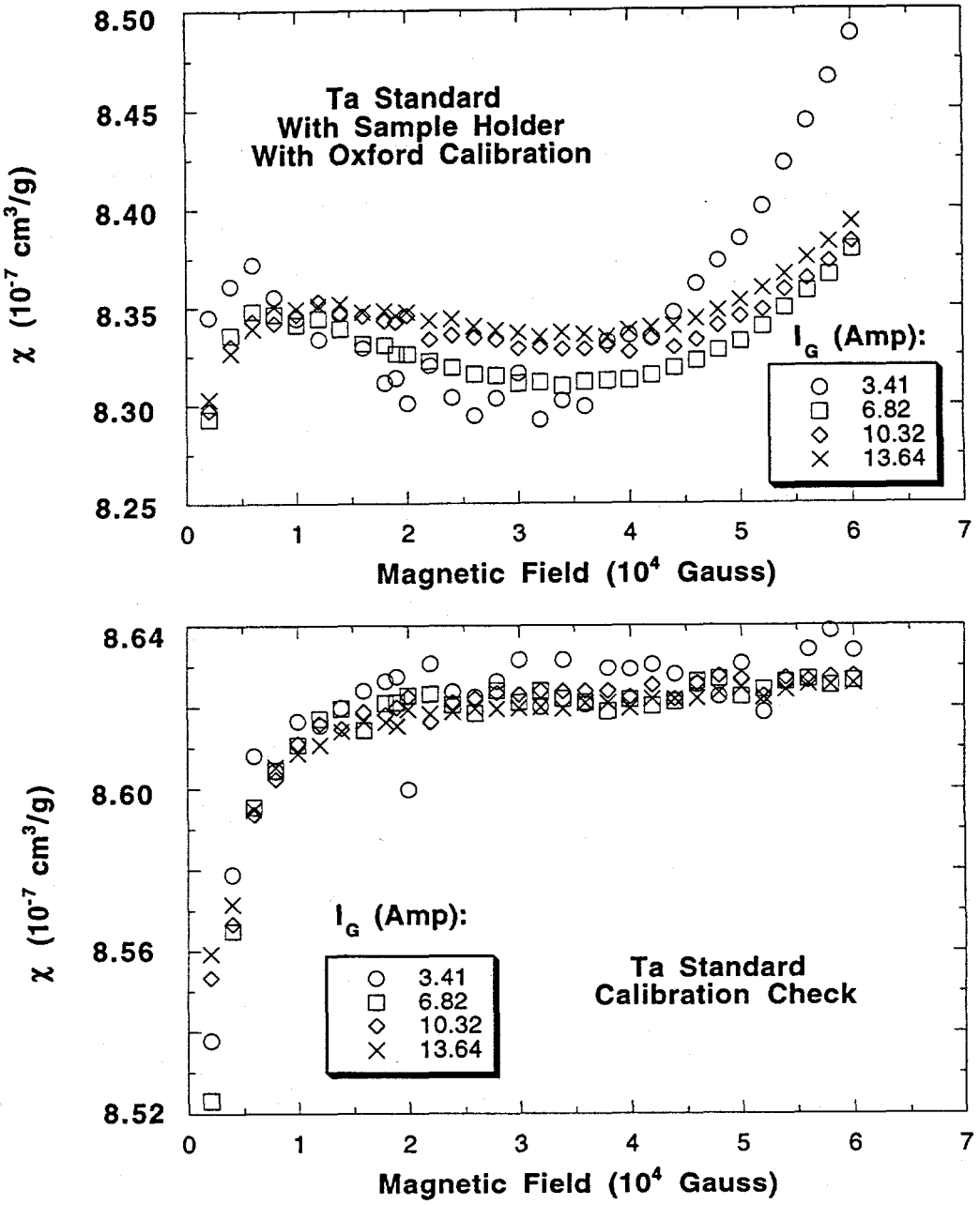

Figure 2.5: (a) The susceptibility determined according to a bipolynomial (Oxford Instruments' program) versus magnetic field at different gradient fields for a standard Ta sample and its sample holder. (b) The susceptibility, determined according to calibration file zrwcalif.cal, versus magnetic field at different gradient fields for a standard Ta sample corrected for the sample holder signal. The symbols represent the values of the gradient coil current I_G.

Centering the Sample in the Magnetometer

Centering the sample was done by positioning the sample in zero field at a height such that the measured force difference ΔF_+ between positive magnetic gradient field and the zero gradient field, is equal to the force difference ΔF_- between zero magnetic gradient field and negative gradient field. Thus, plots of ΔF_+ and ΔF_- versus sample height cross at the correct sample height. This centering assumes that the center of the main magnetic field is the same as the center of the gradient magnetic field.

In order to explain how the method works, let us examine a simple double gradient coil case. The expression for the magnetic field B along the axis of a single-turn coil with current I is

$$B = \frac{\mu_o R^2 I}{2(R^2 + r_o^2)^{3/2}} , \tag{2.38}$$

where R is the radius of the coil and r_o is the distance from a point on the coil axis to the plane of the coil. In the case of $r_o = 0$,

$$B = \frac{\mu_o I}{2R} \equiv B_o . \tag{2.39}$$

If we position two coils with opposite currents a distance a apart, then the magnetic field on the axis of these two coils at the position z of a sample on the axis is

$$B = \frac{\mu_0 I}{2R}\left[\frac{1}{(1+(\frac{z}{R}+\frac{a}{2R})^2)^{3/2}} - \frac{1}{(1+(-\frac{z}{R}+\frac{a}{2R})^2)^{3/2}}\right] , \tag{2.40}$$

where z is the distance between the center of these two coils and the sample. In the $\frac{z}{R} \ll 1$ case we may expand the denominators using Taylor series to yield

$$B = B_o \frac{6z}{(1+\frac{a}{2R})^2 R} . \tag{2.41}$$

If the magnetic moment is proportional to the magnetic field then the force can be calculated in terms of the product of magnetic field and its gradient, which is proportional to

$$B \times \frac{dB}{dz} = B_o^2 \frac{6z}{(1+\frac{a}{2R})^4 R^2} \cdot \tag{2.42}$$

This expression is proportional to z. If we plot Weight(+gradient) - Weight(zero gradient) versus z together with Weight(zero gradient) - Weight(-gradient) versus z, the crossing point of these two plots is the center ($z = 0$) of the two gradient coils.

Temperature Calibration

Temperature calibration of the Faraday magnetometer furnace is accomplished by first performing the calibration at several temperatures, then correcting the nominal temperature value read by the thermometer in the Faraday magnetometer.

A set of magnetic calibration standards (Perkin-Elmer No. 0219-0071) are used to perform the Curie temperature T_C calibration on the Faraday magnetometer furnace. The standard samples we used are Alumel ($T_C = 436$ K), Nickel ($T_C = 627$ K), Nicoseal ($T_C = 711$ K), and Perkalloy ($T_C = 869$ K). The compositions of Nicoseal and Perkalloy are proprietary and would not be released by the manufacturer. The measurement results are shown in Figs. 2.6-2.10.

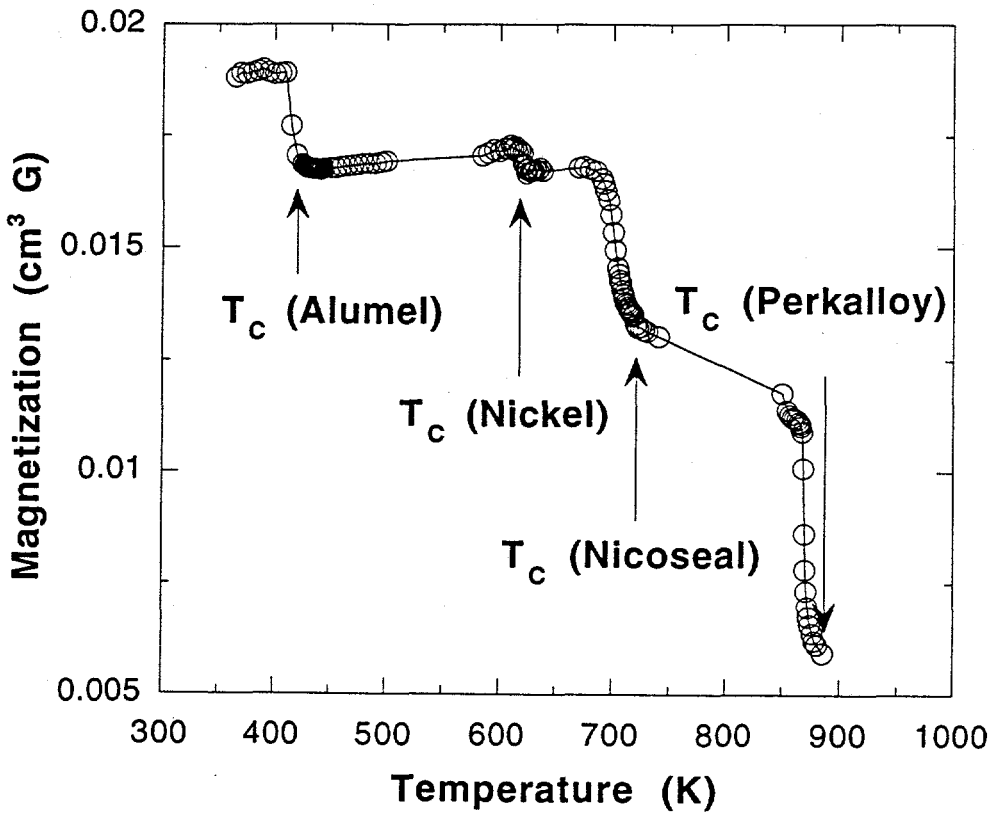

Figure 2.6: The magnetization versus temperature for four different standard calibration samples for the calibration of temperature

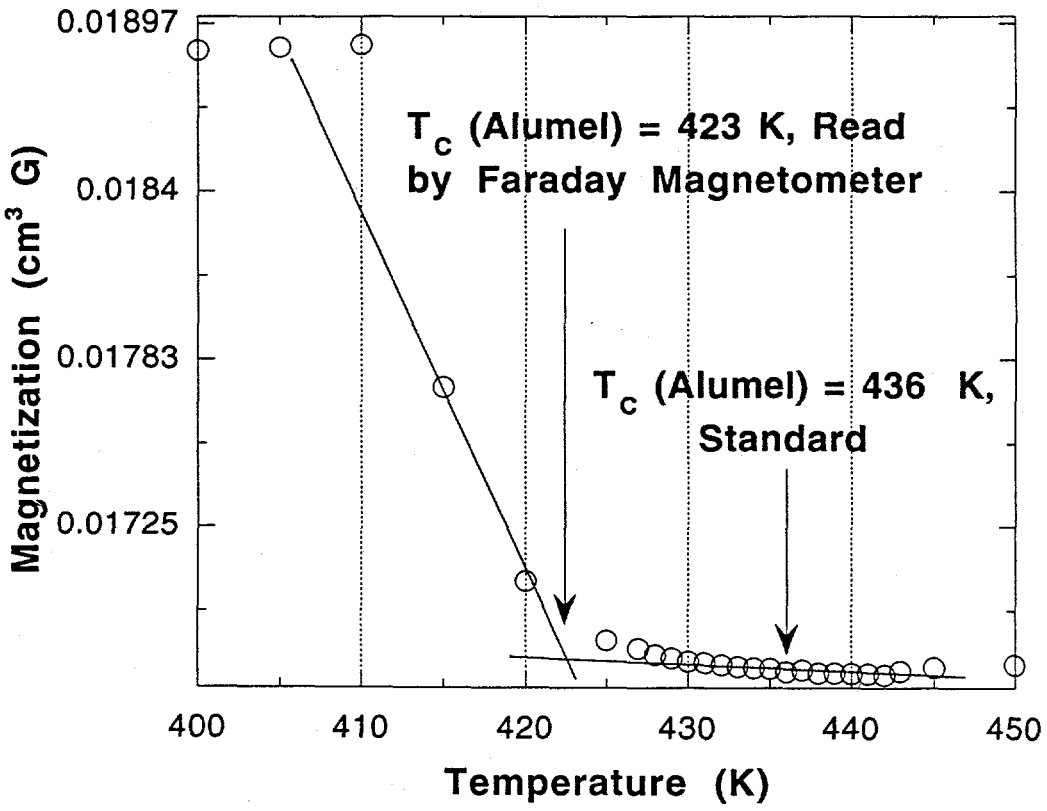

Figure 2.7: The magnetization versus temperature for a standard calibration sample of Alumel.

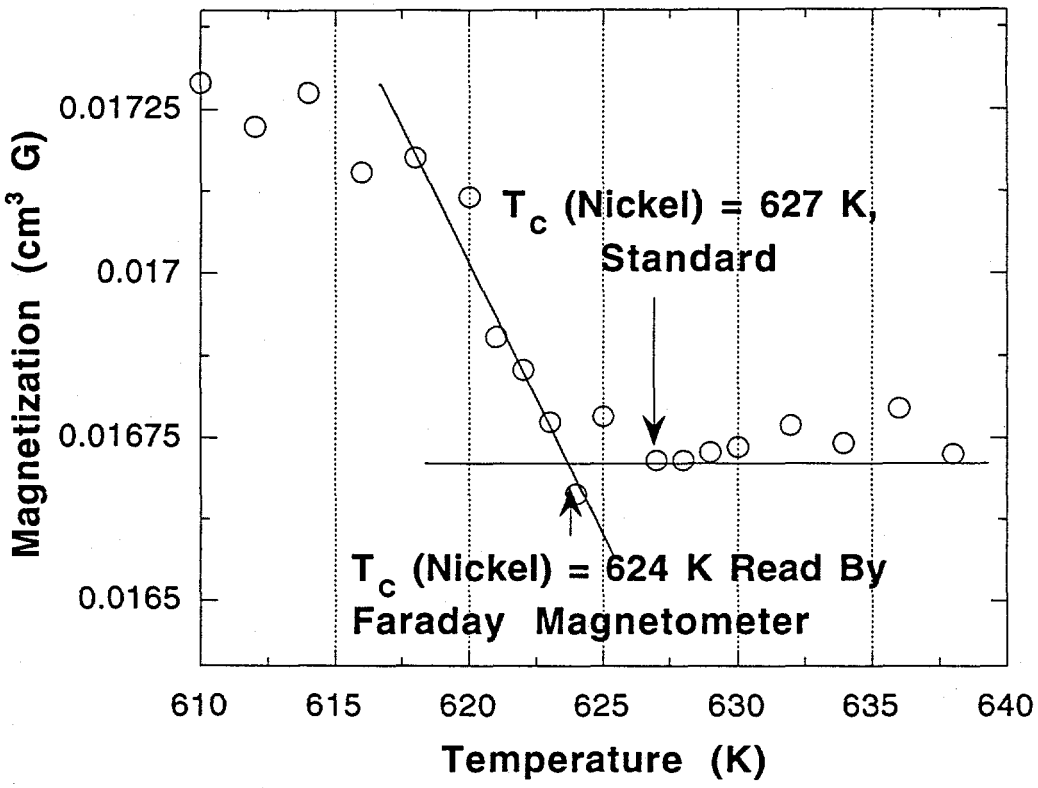

Figure 2.8: The magnetization versus temperature for a standard calibration sample of nickel.

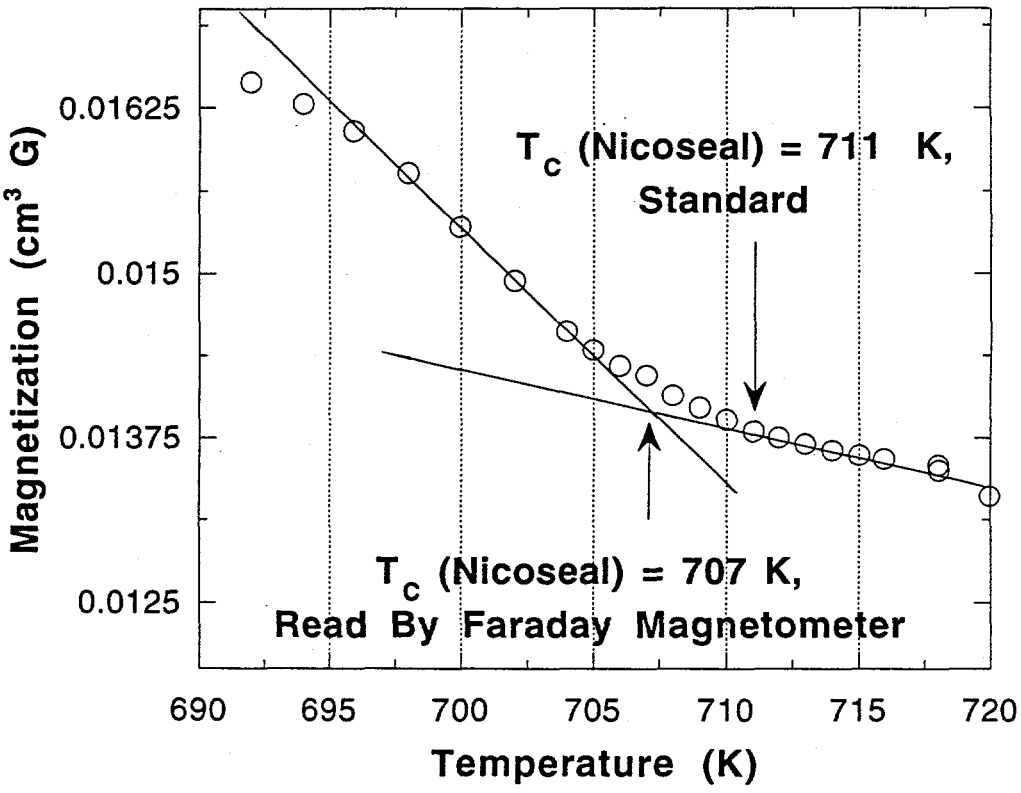

Figure 2.9: The magnetization versus temperature for a standard calibration sample of Nicoseal.

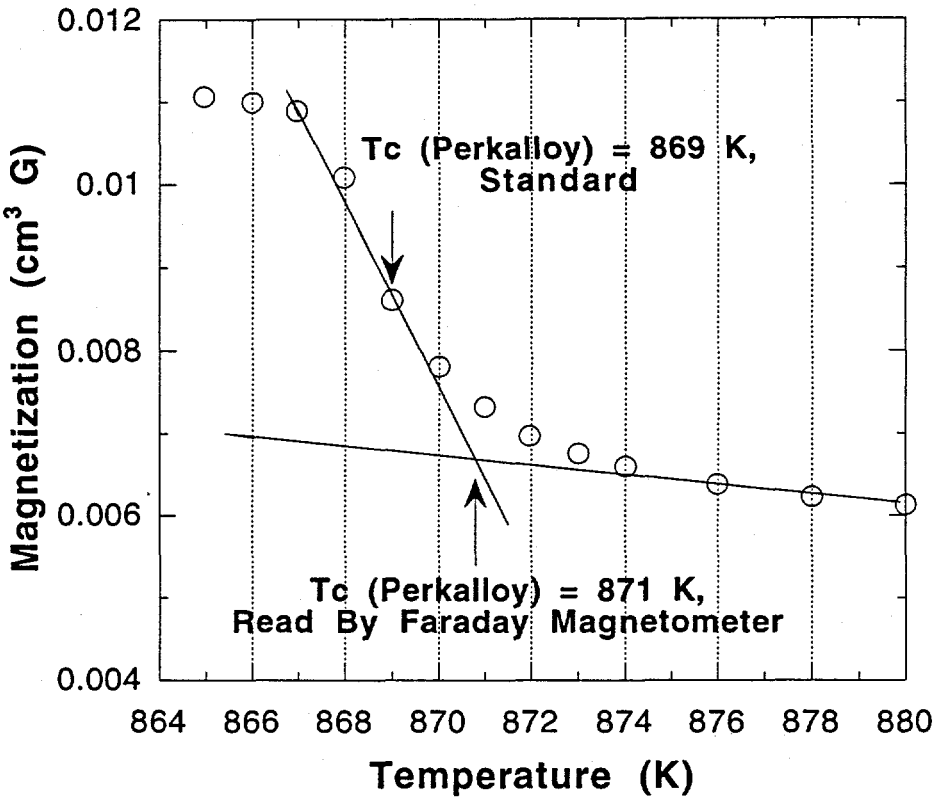

Figure 2.10: The magnetization versus temperature for a standard calibration sample of Perkalloy.

CHAPTER 3. SUPERCONDUCTING PROPERTIES OF $Ba_{0.625}K_{0.375}BiO_3$

Introduction

Due to the unique composition [22], structure [23], and properties [24]-[26] of the superconductor $Ba_{1-x}K_xBiO_3$ system, further investigation of its properties is important to understand the mechanism of this high T_c superconductor. In order to understand more about the material, we systematically studied one of the fundamental parameters that characterizes superconductivity, the magnetic penetration depth. The magnetic penetration depth is related to many important properties of superconductors. For example the energy gap [27], and the effective mass and the superfluid density of a superconductor [25] are related to $\lambda(0)$. For ordinary superconductors at $T = 0$, the superfluid density is identical to the carrier density for $T \geq T_c$.

Two frequently used measurements to determine the magnetic penetration depth of a superconductor are magnetization and muon spin relaxation (μSR). Mitra et al. [28] obtained the temperature dependence of the penetration depth of $YBa_2Cu_3O_{7\pm y}$ and $Bi_2Sr_2CaCu_2O_8$ from magnetic measurements. Uemura et al. [29] used μSR to measure the temperature dependent penetration depth of a series of high T_c materials. They also found a linear relation between T_c and $\lambda(0)$ for "underdoped" high

T_c materials. Thus, it is interesting to see the results for the noncuprate high T_c superconductor $Ba_{1-x}K_xBiO_3$ system.

In this chapter, the magnetic penetration depth, λ(T), was measured by means of muon spin relaxation and the magnetization method for the same batch of single phase $Ba_{0.675}K_{0.325}BiO_3$ (T_c = 26 K). The T-dependence of λ for both methods indicates conventional s-wave pairing with the extrapolated (isotropic) value $\lambda(0)$ = 3400 Å, similar to that of $La_{2-x}Sr_xCuO_4$ samples of the same T_c [30]. However as the temperature approaches T_c there is a significant difference in magnetic penetration depth for these two methods, and a possible explanation for this difference will be discussed. The magnetization data were fitted using the Hao-Clem model [36]. The different results from these two methods can be explained by the field dependence of the penetration depth.

Sample Preparation and Charactization

The single phase material was made by the two-step method [23]. The starting materials were BaO (99.99%), KO_2 (95%), and Bi_2O_3 (99.9%). The optimum synthesis conditions were determined by TGA, [24] SQUID magnetometry, and X-ray diffraction [23]. The conditions for making a 15 g batch of the sample were as follows. First, we rapidly (1 ^oC/min) heated the sample in N_2 to 700 ^oC and maintained the sample at this temperature for one hr. The sample was then rapidly cooled to room temperature by quenching in vacuum. Next, the sample was ground in a glove box for one hr in a He atmosphere and heated at 1 ^oC/min in O_2 to 550 ^oC. This temperature was maintained for one hr and then the sample was oven-cooled to room temperature. X-ray results showed very sharp diffraction peaks, and no impurity

peaks were detected.

The magnetic susceptibility data were obtained with a Quantum Design Superconducting Quantum Interference Device (SQUID) magnetometer. We compared the penetration depth of the sample returned from the μSR measurements with the remainder of the sample (kept in the glove box). The results show that the penetration depth agreed to within 1% for the two samples.

From the M vs. H curve in the normal state at several different temperatures, we obtained the ferromagnetic impurity average spontaneous magnetization contribution, $M_s = 4.14 \times 10^{-5}$ G cm^3/g. Also, by fitting the M vs T curve at 1 T near T_c with a constant term plus an impurity Curie-Weiss contribution

$$\chi(T) = \chi_0 + \frac{C}{T - \theta}\,, \tag{3.1}$$

we obtained $\chi_0 = -2.15 \times 10^{-7}$ cm^3/g, $C = 2.36 \times 10^{-6}$ cm^3 K/g, and $\theta = -10.6$ K. The magnetization data were corrected for these impurity contributions.

Experimental Results

μ^+SR Measurement

The sample was made into a cylindrical pellet about 25 mm in diameter and 4 mm thick, which insured that all of the incident muons stopped in the sample. The μSR measurements were carried out by our collaborators using "surface" beams at the TRIUMF cyclotron. The apparatus and techniques are similar to those of previous work [30],[31]-[35]. Field cooled (FC) scans from the normal state were used for the determination of $\lambda(T)$, and zero-field-cooled (ZFC) measurements were carried out to test background and flux pinning effects for completeness. The asymmetry function

in the transverse field (TF) consists of a precession signal (Larmor frequency for the muons in the average internal field) modulated by the spin relaxation function G_{TF}. In turn, $G_{TF}(t)$ is the Fourier transform of the lineshape due to the microscopic field distribution acting on the muon spin magnetic moment,

$$G_{TF}(t) = exp(-\sigma^2 t^2). \tag{3.2}$$

The Gaussian approximation (giving the second moment, σ, of the field distribution directly) yielded good fits to the data. Figure 3.1 shows the obtained $\sigma(T)$, compared for reference to the empirical relation

$$\lambda(T) = \lambda(0)[1 - (T/T_c)^4]^{-1/2}\ , \tag{3.3}$$

and Larmor frequency versus temperature. Thus, we obtain $T_c = (26 \pm 1)$ K and a penetration depth $\lambda(0) = 3400\ \mathring{A}$ (see below) , similar to that of $La_{2-x}Sr_xCuO_4$ of comparable T_c.

Magnetization Measurement

The SQUID sample was put into a 3 mm I.D. quartz tube, which formed a cylinder 8 mm in length. The magnetization M versus magnetic field H data were averaged over increasing field and decreasing field, as an approximation to the reversible magnetization [28]. The zero field shielding at 5 K is equivalent to a 73% superconducting fraction. The $M(H)$ data are shown in Fig. 3.2. Additional $M(T)$ data are shown in Fig. 3.3.

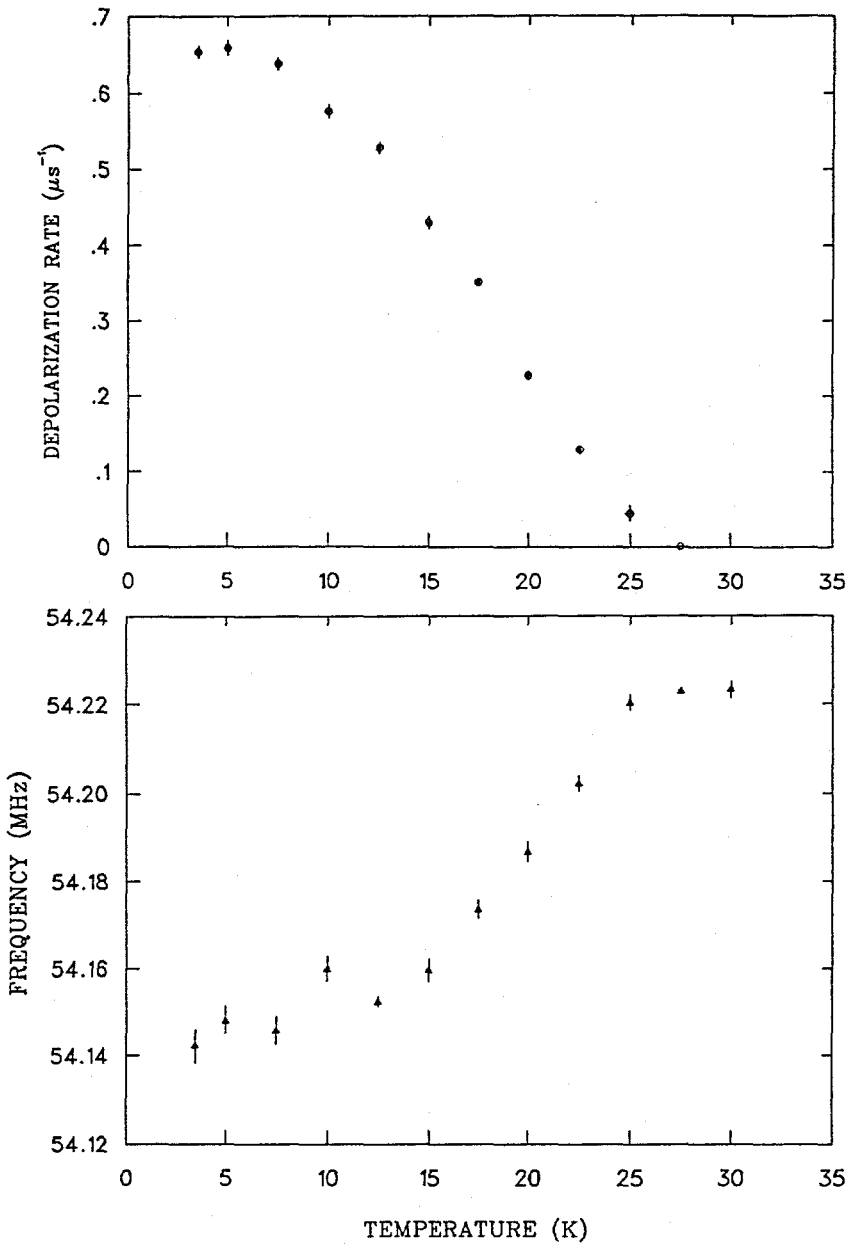

Figure 3.1: Temperature dependence of the Gaussian relaxation rate σ and Larmor frequency for an applied field $H_{ext} = 4$ kG

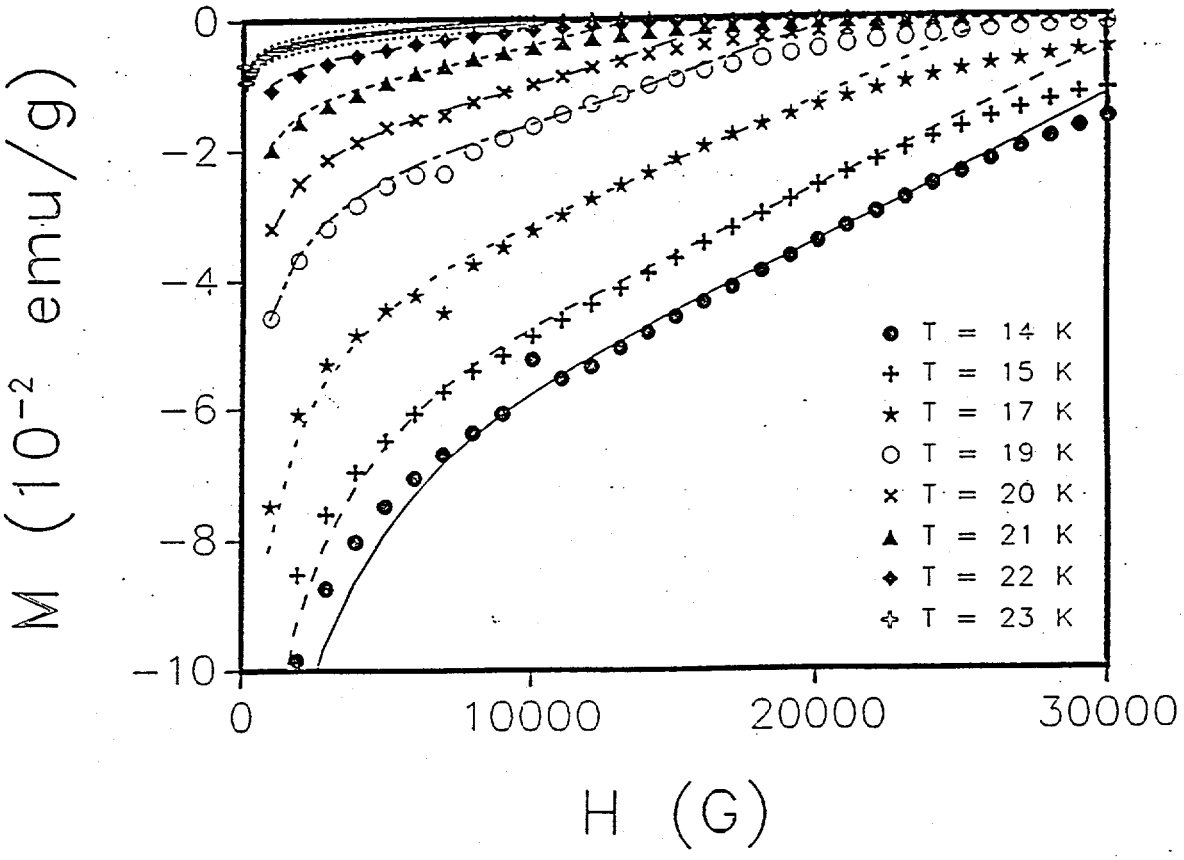

Figure 3.2: Magentization M versus applied magnetic field H at different temperatures T. The solid and dashed lines are the theoretical fits to the experimental points.

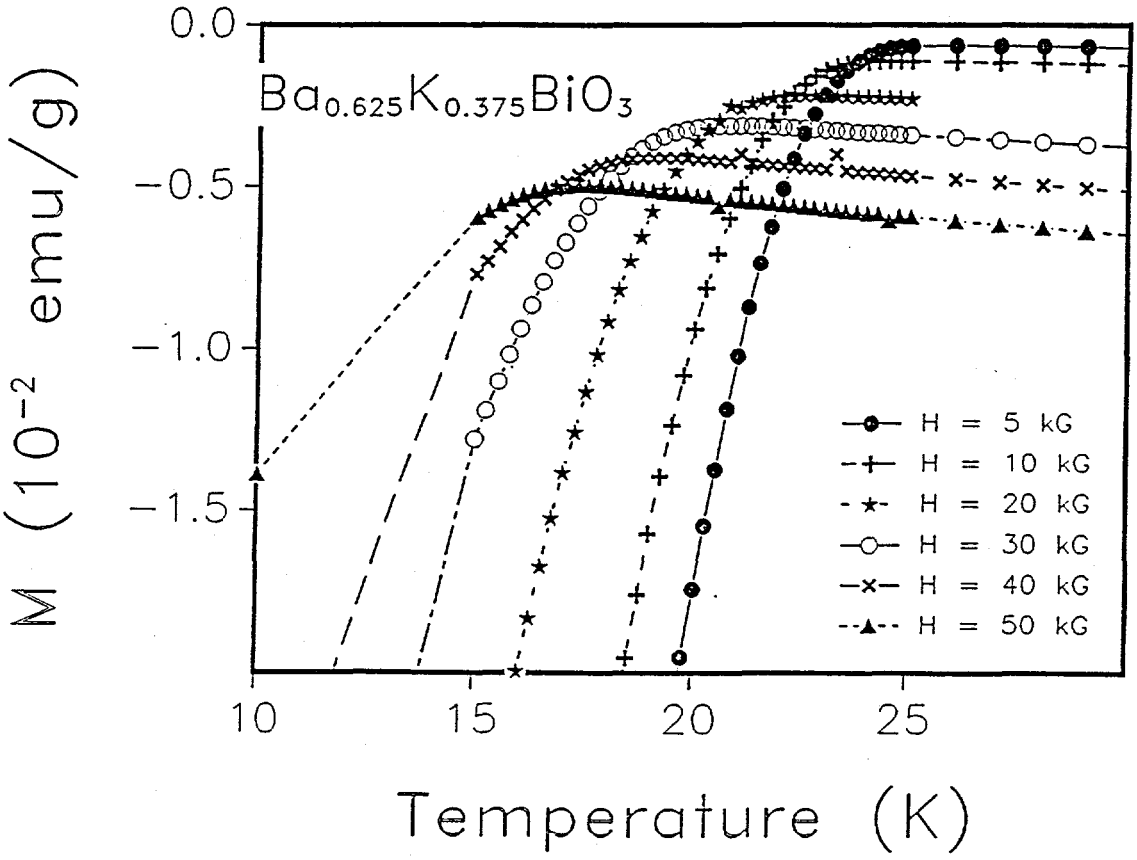

Figure 3.3: Magnetization M versus Temperature T at different magnetic fields H.

Theory and Data Analysis

μ^+SR

As detailed in the previous work on $YBa_2Cu_3O_{7-x}$ and $La_{2-x}Sr_xCuO_4$, [30]-[40] λ is determined from the relaxation of the muon spin polarization signal in an external field H_{ext} such that the separation between the vortices is much smaller than λ. Under this condition the μ^+ spin relaxation rate, $\sigma = 1/T_2$, is almost independent of H_{ext}, and is given by the second moment of the microscopic field distribution [40], analogous to the field inhomogeneity broadening (T_2 relaxation) in magnetic resonance [40]. From the relaxation time, T_2, the magnetic penetration depth is determined (assuming a perfect vortex lattice) by the relation, [38]

$$\lambda = \sqrt{0.043\phi_0\gamma_\mu T_2}, \tag{3.4}$$

where ϕ_0 is the magnetic flux quantum, and γ_μ is the muon's gyromagnetic ratio.

Reversible Magnetization and Penetration Depth

Hao and Clem [36], starting from Ginzburg-Landau theory, obtained the following expression for the reversible magnetization M:

$$\begin{aligned} -4\pi M = \quad & \frac{\kappa(1-(\frac{B}{\kappa})^4)\xi_v^2}{2}[\frac{(\frac{B}{\kappa})^4}{2} ln(\frac{2}{B\kappa\xi_v^2}+1) - \frac{(\frac{B}{\kappa})^4}{2+B\kappa\xi_v^2} + \frac{1-(\frac{B}{\kappa})^4}{(2+B\kappa\xi_v^2)^2}] \\ & + \frac{[1-(\frac{B}{\kappa})^4](2+3B\kappa\xi_v^2)}{2\kappa(2+B\kappa\xi_v^2)^3} + \frac{1-(\frac{B}{\kappa})^4}{2\kappa\xi_v K_1(\kappa B\xi_v)} \\ & [K_0(\xi_v\sqrt{1-(\frac{B}{\kappa})^4+2B\kappa}) - \frac{B\kappa\xi_v K_1(\xi_v\sqrt{1-(\frac{B}{\kappa})^4+2B\kappa})}{\sqrt{1-(\frac{B}{\kappa})^4+2B\kappa}}] , \end{aligned} \tag{3.5}$$

where $K_n(x)$ is a modified Bessel function of nth order,

$$\kappa\xi_{v0} = \sqrt{2}[1 - \frac{K_0^2(\xi_{v0})}{K_1^2(\xi_{v0})}]^{1/2} , \tag{3.6}$$

$$(\frac{\xi_v}{\xi_{v0}})^2 = [1 - 2(1 - \frac{B}{\kappa})^2\frac{B}{\kappa}][1 + (\frac{B}{\kappa})^4] , \tag{3.7}$$

and

$$-4\pi M = H - B . \tag{3.8}$$

The only adjustable parameters are κ and H_c, where κ is the Ginzburg-Landau parameter and H_c is the thermodynamic critical field which is also a scaling parameter: $\sqrt{2}H_c = \kappa\phi_0/2\pi\lambda^2$, and $H_{c2}(T) = \kappa\sqrt{2}H_c(T)$. We use $\sqrt{2}/\xi_{v0}$ as an approximation for $\kappa(\xi_{v0})$, which results in a less than 1% error for $\kappa \geq 30$.

The M vs H data in Fig. 3.2 were fitted with the Hao-Clem theory [36]. The fitting parameters, κ and H_{c2}, were converted to λ by the formula $\lambda^2 = \kappa^2\phi_0/(2\pi H_{c2})$, shown in Fig. 3.4. The upper critical fields from these fits, plotted in Fig. 3.5, are similar to results from the literature. [35]

Discussion

From the two fluid model, Eq. 3.3, we know that the penetration depth depends on the critical temperature T_c. However the critical temperature depends on the applied magnetic field, and in turn the penetration depth depends on the applied magnetic field. Therefore so we get a generalized two fluid model

$$\lambda(T) = \lambda(0)[1 - (\frac{T}{T_c(H)})^4]^{-1/2} . \tag{3.9}$$

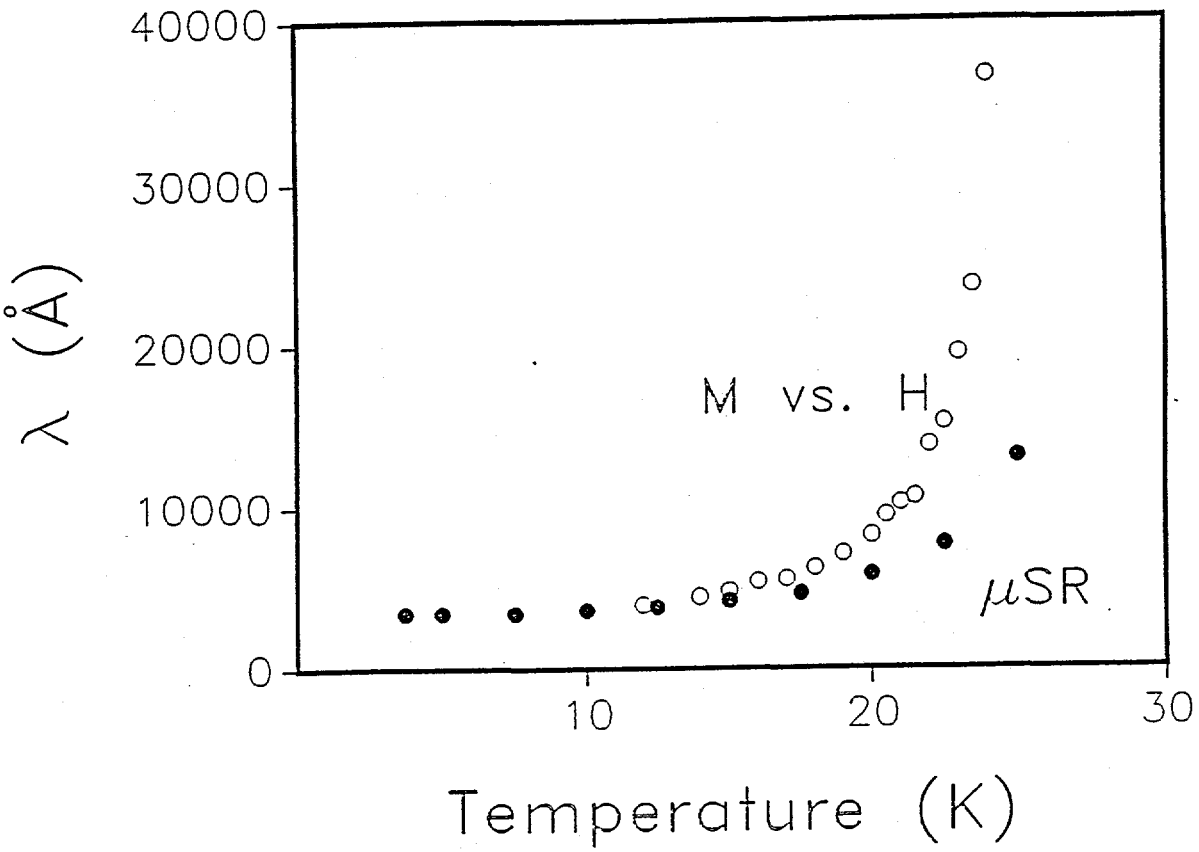

Figure 3.4: Penetration depth λ versus temperature. The solid dots are μSR data, and the open circles are magnetization data.

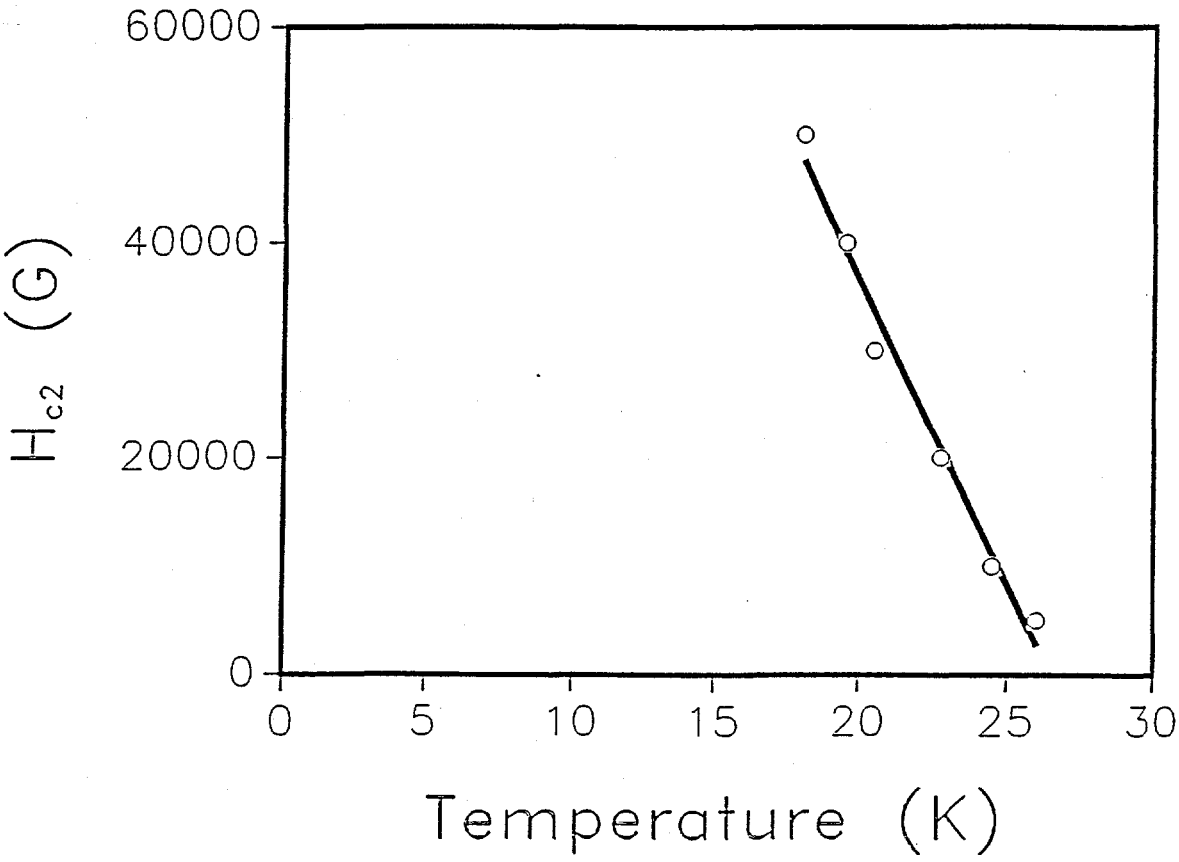

Figure 3.5: Upper critical field H_{c2} versus temperature

Then the difference between μSR and magnetization penetration depths when the temperature is close to the critical temperature could be explained by the field dependence of the penetration depth. This tendency that the μSR penetration depth changes faster with temperature near T_c than the magnetization penetration depth can also be seen in other studies [28] [29] [96] [39] [43].

From the onset of superconductivity as seen in the M versus T data in Fig. 3.3, we get the critical field H_{c2} = -0.56 (Tesla/K) T+14.9 Tesla as shown in Fig. 3.5, from which we obtain T_c (H = 0) = 26 K. Thus,

$$T_c(K) = 26 + \frac{1}{\frac{dH_{c2}}{dT}} H(T) = 26 - \frac{H(T)}{0.56}. \tag{3.10}$$

For the reason that our fitting must be in the reversible range, the fitting range in the $M(H)$ plots changes for different T values. The middle of our fitting range can be approximately written as $H(T)$ = -0.19 $T(K)$ +4.9, which in turn gives the relation between the critical temperature and temperature to which the $M(H)$ curve was fitted

$$T_c = 17.3 + 0.34T \ . \tag{3.11}$$

Therefore, T_c is changing when the T changes. Our fitting range is 14 K to 24 K, which leads us to the average range $\bar{T}$ = 19 K with an error bar 2 K. From Fig. 3.4 we see that within the error of experiment, the μSR penetration depth matches the magnetization penetration depth data for $T \leq$ 15 K.

In our sample we did not find any sign of a node in the gap (i.e., the penetration depth for $T \leq$ 10 K is alomost independent of T). We also observed that our $\lambda(0)$ data satisfy Uemura's linear T_c versus $\frac{1}{\lambda^2}$ relation [43].

The κ value at low temperatures is almost constant, equal to 40. Then, the

coherence length for the system in the low temperature limit is $\xi = \lambda/\kappa = 85$ Å.

CHAPTER 4. MAGNETIC PROPERTIES OF $BaCuO_{2+x}$

Introduction

The structures of all known high transition temperature T_c cuprate superconductors contain CuO_2 planes [44]. The parent (undoped) insulator (at $T = 0$) phases of those materials, like La_2CuO_4 and $YBa_2Cu_3O_6$, exhibit long-range antiferromagnetic (AF) ordering of the Cu^{+2} (d^9) magnetic moments below a Néel temperature $T_N < 550$ K [45] [11], and dynamic two-dimensional AF short-range ordering above T_N [46] [101]. Furthermore, upon doping with either additional oxygen or by cation substitutions, the insulating parent materials become metallic and T_N drops to zero, but short range AF order survives [11]-[48]. The short range AF order may play an important role in the mechanism of the high temperature superconductivity [49]. The strong AF interaction ($J \sim 1500$ K) between the Cu spins in the CuO_2 planes [11] [101] originates from the 180^o-bond-angle Cu^{+2}-O^{-2}-Cu^{+2} indirect superexchange interaction [50] [51]. Aharony et al. [52] and others (e.g. [53]) have argued that an intervening O^{-1} ion produced by a localized doped hole on the O^{-2} ion results instead in an indirect *ferromagnetic* interaction between the two adjacent Cu spins. This *ferromagnetic* interaction would result in magnetic frustration which may be relevant to the superconducting pairing mechanism in the high T_c cuprates [52]. However, an alternative cause of FM interactions has been predicted to be a

change in the Cu^{+2}-O^{-2}-Cu^{+2} bond angle from 180^o to 90^o [51]. This bond angle has recently been found by Büchner et al. [54] to be important to the occurrence of superconductivity. Their experiments show that when the tilt angle of the CuO_6 octahedra in $La_{2-x-y}Sr_xNd_yCuO_4$ decreased below 3.6^o, the superconductivity was destroyed. Thus it is important to further clarify the conditions under which FM versus AF Cu^{+2}–Cu^{+2} interactions occur in copper oxides.

A FM Cu^{+2}–Cu^{+2} interaction has been found in several copper oxide compounds. For example, in $La_4Ba_2Cu_2O_{10}$ a bulk three dimensional ferromagnetic transition at 5.2 K was detected [55]. The structure of this compound contains isolated square-planar CuO_4 units. The planes of adjacent CuO_4 units are nearly perpendicular to each other. The Cu-O-Cu angle is 114.2^o, but the respective Cu-O and O-Cu distances are 1.82 $\AA$ and 3.80 $\AA$. Since the latter distance is much larger than the sum of the Cu^{+2} and O^{-2} ionic radii, the FM Cu-Cu coupling is very weak ($J = 2.6$ K [55]). Another example is Li_2CuO_2 [56] [57], in which square-planar CuO_4 units are edge-shared to form infinite chains. The intrachain Cu^{+2}-O^{-2}-Cu^{+2} bond angle is 94.0^o, and the Cu^{+2}-O^{-2} distance is 1.96 $\AA$ [56]. Specific heat and magnetic susceptibility measurements show an AF ordering transition at $T_N = 9.3$ K [58]. However, neutron diffraction measurements revealed that below T_N, the spins in the chains are ferromagnetically aligned as expected from the Cu^{+2}-O^{-2}-Cu^{+2} bond angle, and the AF character below T_N arises from AF alignment of the spins in adjacent chains [56] [59].

The material studied in this work is $BaCuO_{2+x}$. This compound has a large body-centered-cubic unit cell ($a_o = 18.277$ $\AA$) with 90 formula units/cell [60] [61]. As illustrated in Fig. 4.1, the cell contains 6 lone CuO_2 units, 8 Cu_6O_{12} ring clusters

[Fig. 4.1(b)] and 2 $Cu_{18}O_{36}$ sphere clusters [Fig. 4.1(c)]. Within the ring clusters, the Cu^{+2}-O^{-2}-Cu^{+2} bond angle is 82.83^o, the Cu^{+2}-O^{-2} distance is 1.969 $\AA$, and the Cu^{+2}–Cu^{+2} distance is 2.605 $\AA$, whereas within the sphere clusters, the Cu^{+2}-O^{-2}-Cu^{+2} bond angle is 86.86^o, the Cu^{+2}-O^{-2} distance is 1.98 $\AA$, and the Cu^{+2}–Cu^{+2} distance is 2.698 $\AA$ [61]. A picture of the unfolded ring is shown in Fig. 4.1(d). Because these bond angles are rather close to 90^o, one would expect the Cu spins in the Cu_6 and Cu_{18} clusters to be ferromagnetically coupled.

By considering the atomic position occupancies of $BaCuO_{2+x}$ from the structure determined using single crystal x-ray diffraction, Kipka and Müller-Buschbaum [60] obtained the composition $BaCuO_2$. Similarly, Weller and Lines [61] found the compositions of two samples to be $BaCuO_2$ and $BaCuO_{2.07}$. They also measured the oxygen content of a sample by means of thermogravimetric analysis (TGA). They heated their sample to 800 ^oC under N_2 + 5 % H_2 at 30 ^oC/min. The weight loss gave the composition of the initial material as $BaCuO_{2.08\pm0.02}$. From structural analysis on a single crystal, Paulus et al. [62] found the oxygen content to be 2.28 by modifying the crystal model obtained by Kipka et al. [60]. Aranda et al. [63] used both x-ray and neutron diffraction methods, and obtained the composition $Ba_{44}Cu_{48}(CO_3)_6O_{81+x}$, (with $x = 6.9(3)$ for their sample) instead of $BaCuO_{2+x}$. Using iodometric titration, Eriksson et al. [64] found the oxygen content to be between 1.8 and 2.05. Therefore the oxygen content of $BaCuO_{2+x}$ appears to be variable [65].

Specific heat measurements have been reported by Eckert et al. [67]. The results vary from sample to sample below $\sim$ 15 K. For a sample prepared in air, a (magnetic) phase transition was found at about 13 K.

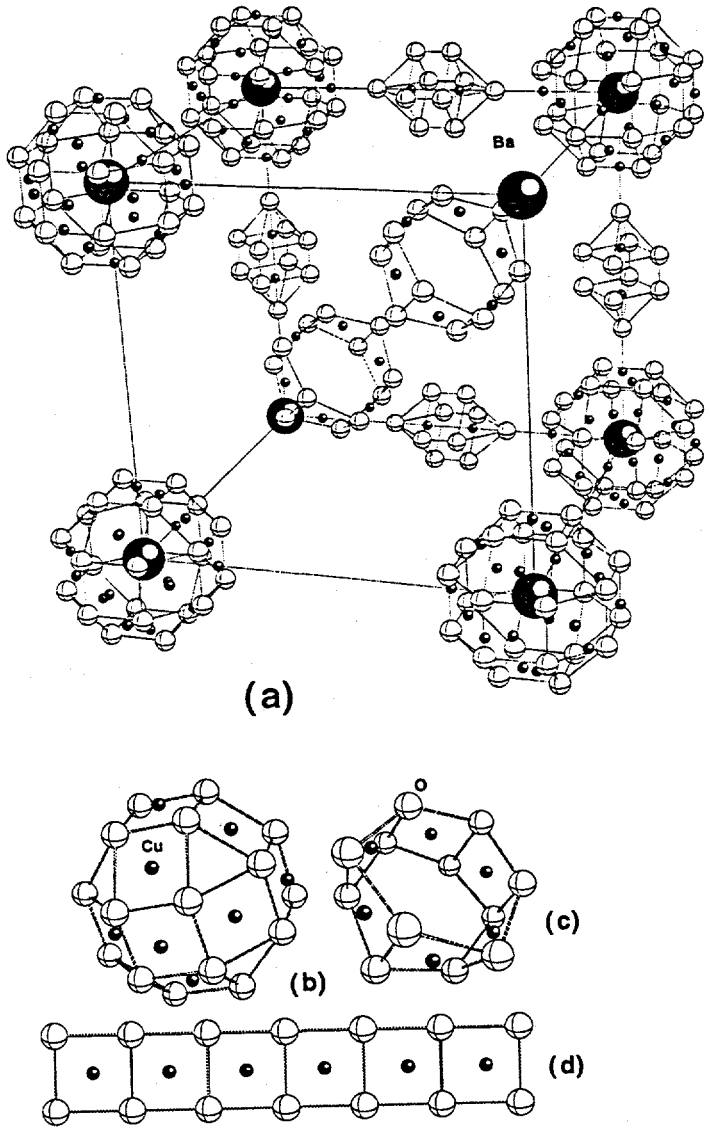

Figure 4.1: Perspective representation of the two types of Cu-O clusters in the bcc unit cell of $BaCuO_{2+x}$. The sphere-like clusters are located at the (000) and (1/2 1/2 1/2) (not shown) the ring-like clusters are located at the (1/4 1/4 1/4) and the remaining seven equivalent positions with their axis of highest symmetry along the corresponding body diagonal (only two rings are shown). The lone spins are located along principal directions adjacent to the spheres (partially occupied). Both clusters consist of closed one-dimensional strips of Cu_4O oxygen edge-sharing squares.

Electrical conductivity σ measurements have been reported by Migeon et al. [68]. The conductivity was found to be activated, with an activation energy of 0.61 eV for $BaCuO_2$, but which decreased with increasing oxygen content. A slope change was found in $\log(\sigma)$ versus $1/T$ at $\approx$ 370 K [69], for both $BaCuO_2$ (cubic) and $BaCuO_{2.5}$ (orthorhombic) samples.

The magnetic properties of $BaCuO_{2+x}$ have been previously measured by many research groups. From electron spin resonance (ESR) measurements, Vier et al. [70] and de Mesquita et al. [71] concluded that the resonance observed at room temperature originated from Cu^{2+} ($3d^9$). Vier et al. [70] found the peak-to-peak linewidth to have a minimum at about 15 K which can be associated with a magnetic phase transition, but the magnetic structure was unknown. They also measured the DC magnetic susceptibility and found that the susceptibility χ versus temperature T curve can be characterized into two parts according to temperature range. For $T \geq$ 100 K, the $1/\chi$ versus temperature plot shows a linear behavior which corresponds to an effective magnetic moment μ_{eff} of 1.72 μ_B per Cu ion; at lower temperatures, the $1/\chi$ versus T curve shows positive curvature and μ_{eff} increases, reaching a value of 3.16 μ_B below 30 K. Recently Petricek et al. [72] reported the observation of an antiferromagnetic to diamagnetic transition at about 3 K from χ(T) measurements for their sample of $BaCuO_{2.5}$ (with a non-cubic structure).

Herein, we report ac and dc magnetization measurements of $BaCuO_{2+x}$ from 2 K to 400 K in magnetic fields up to 55 kG. Our study was initially motivated by the observation of an anomalously strong, crystallographically forbidden (111) peak in the neutron diffraction pattern of this compound at 4 K which was not present at 300 K, suggesting that this reflection was magnetic in origin [95]. On the other

hand, the intensity of this peak was comparable to those of adjacent structural peaks, and the various magnetic structures modeled could not explain the intensity of this peak and the simultaneous absence of other magnetic peaks. We successfully resolved the nature and provided a model for the magnetic structure of the magnetic phase below 15 K via analysis of the present measurements. This model has been verified from analyses of subsequent polarized and unpolarized magnetic neutron diffraction measurements [74] [66]. Following the experimental details in the next section, we present our magnetization data, analyze them and present our model of the magnetic structure below T_N. We conclude with a discussion of the results. Some of our results were briefly presented previously [74].

Experimental Details

Sample Preparation and Oxygen Content

To synthesize $BaCuO_{2+x}$, a one-to-one molar ratio mixture of $BaCO_3$ (99.99 %) and CuO (99.99 %) was ground thoroughly and heated in air to 800 ^oC for 24 hours. The sample was then reground and fired five times in air at 925 ^oC for 24 hours. The sample weight was recorded before and after each heat treatment. The final total weight loss of the batch was 13.663 %, giving a final product composition of $BaCuO_{2.39}$, assuming that all the CO_2 gas in the $BaCO_3$ was released. The oxygen content of the batch was also measured using TGA by heating to 950 ^oC in 5% H_2/He at a rate of 2 ^oC/min and holding at 950^o for 180 min. The weight did not change during the last 100 min of this 180 min period. The oxygen content from this measurement was found to be 2.56 ± 0.03. Portions of the batch were annealed in He or O_2 at 900 ^oC for 10 hours and cooled to room temperature at a rate of 10 ^oC/hr.

The oxygen content for the O_2-annealed sample was then measured using TGA by heating the sample in 5% H_2/He to 950 ^oC at a rate of 0.5 ^oC/min, as shown in Fig. 4.2(top), where the weight does not change above 820 ^oC. From the weight loss, the oxygen content of the O_2-annealed sample was found to be 2.6 $\pm$ 0.1. The oxygen content for the He-annealed sample was measured using TGA in 5% H_2/He at a rate of 5.0 ^oC/min and kept at 950 ^oC for 30 min, as shown in Fig. 4.2(bottom). From the weight loss, we calculated the oxygen content for the He-annealed sample to be 2.1 $\pm$ 0.1.

X-ray Analysis

Powder X-ray diffraction measurements were carried out using a Rigaku Geiger-flex diffractometer, with a curved graphite crystal monochromator, using Cu K_α radiation (λ = 1.5418 $\AA$). The X-ray patterns for the He-annealed sample and O_2-annealed sample are shown in Fig. 4.3(top) and Fig. 4.3(bottom) respectively. The peaks were indexed according to the structural model obtained by Kipka et al. [60] and Weller et al. [61], and no impurity peaks were found, fraction of impurity phase in our samples is therefore estimated to be less than 5%. The peak positions were corrected for zero point shift and nonlinearity using Si as an internal standard. Lattice parameters were obtained using the least squares fitting program FINAX. The lattice parameter was found to be a_o = 18.29 $\pm$ 0.03 $\AA$ for the He-annealed sample, and a_o = 18.34 $\pm$ 0.03 $\AA$ for the oxygen-annealed sample. The lattice parameter thus appears to increase as the oxygen content increases, as also observed by Weller (18.277 - 18.286 $\AA$) [61], Migeon (18.28 - 18.31 $\AA$) [68], and Eriksson (18.27 - 18.32 $\AA$) [64] [65]. Our oxygen- and helium-annealed samples were found [66] from neutron

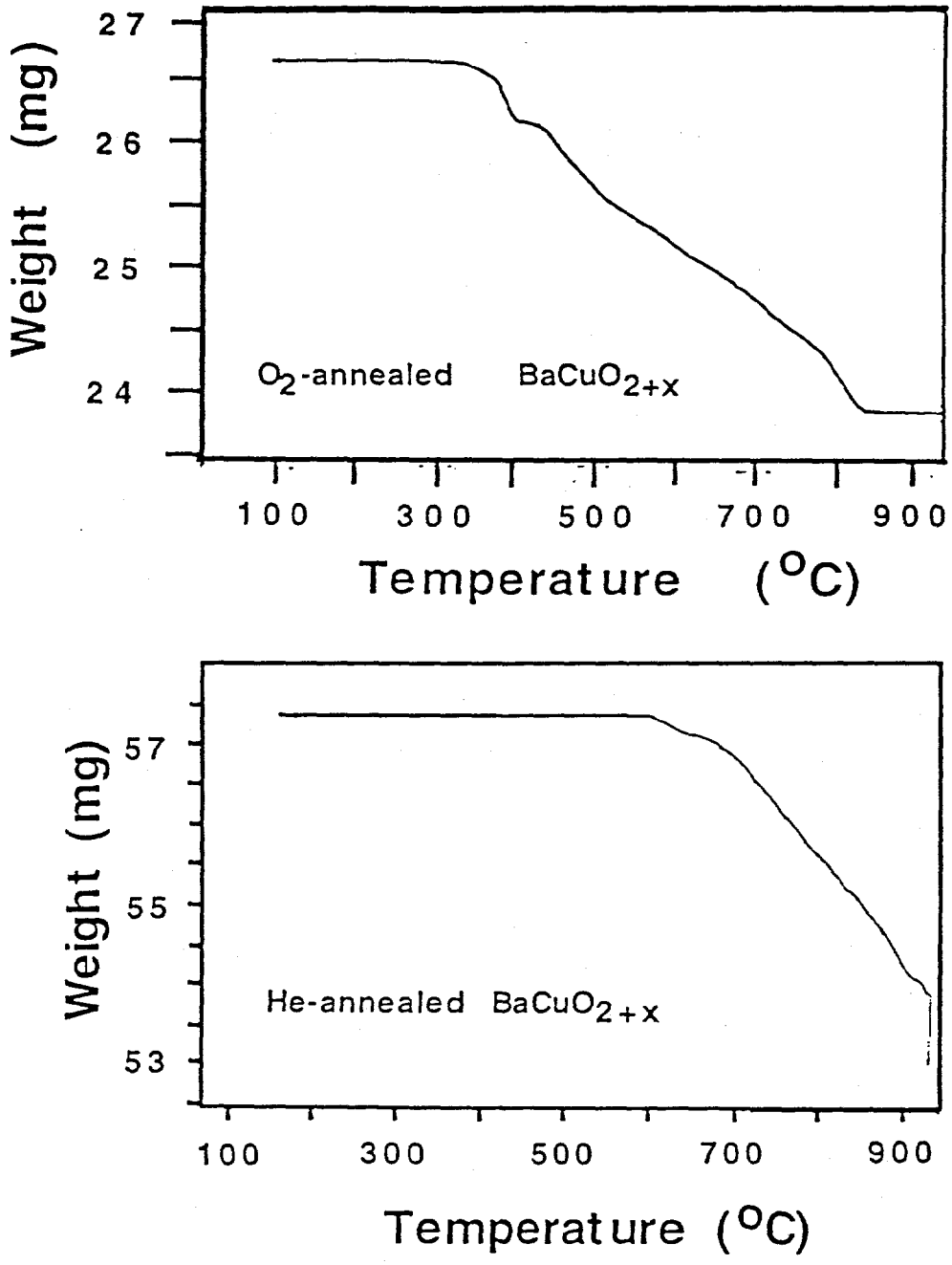

Figure 4.2: Thermogravimeteric analysis (TGA) data for $BaCuO_{2+x}$

diffraction measurements to have essentially the same structure as proposed in [60] and [61].

DC and AC Magnetization Measurements

AC magnetic susceptibility measurements were made on a Lake Shore ACS7000 AC susceptometer. The amplitude of the AC field was kept at 100 Gauss and the frequency at 125 Hz. The measurements versus temperature T were performed under constant DC magnetic field in the range of 0 to 50 kG. DC magnetization M data were obtained using a Quantum Design SQUID magnetometer. The $M(T)$ was measured at fixed applied magnetic fields of H = 500 G and H = 10 kG, from 2 K to 400 K, and $M(H)$ isotherms were measured at a series of different temperatures.

Experimental Results and Preliminary Analysis

The observed magnetic susceptibility χ of $BaCuO_{2+x}$ is expected to be the sum of three terms: $\chi = \chi^{dia} + \chi^{VV} + \chi^{spin}$, where the first term is due to the orbital diamagnetism of the closed-electron-shells of the atoms, the second is the orbital paramagnetic Van Vleck susceptibility of the Cu^{+2} ions and the third term is the spin susceptibility of the Cu^{+2} ions. From standard tables [75], one obtains χ^{dia} = -6.8 $\times$ 10^{-5} cm^3/mol for $BaCuO_2$ and χ^{dia} = -7.4 $\times$ 10^{-5} cm^3/mol for $BaCuO_{2.5}$. The anisotropic χ^{VV} values for Cu^{+2} in the layered high T_c cuprates have been estimated in, for example, Ref. [76]. For our samples, we take the powder average of those values and estimate that $\chi^{VV} \approx 7.4 \times 10^{-5}$ cm^3/mol. Thus, the sum χ^{dia} + χ^{VV} is nearly zero and we will neglect it. Also, since $\chi \simeq \chi^{spin}$, we will henceforth denote χ^{spin} by χ to simplify notation.

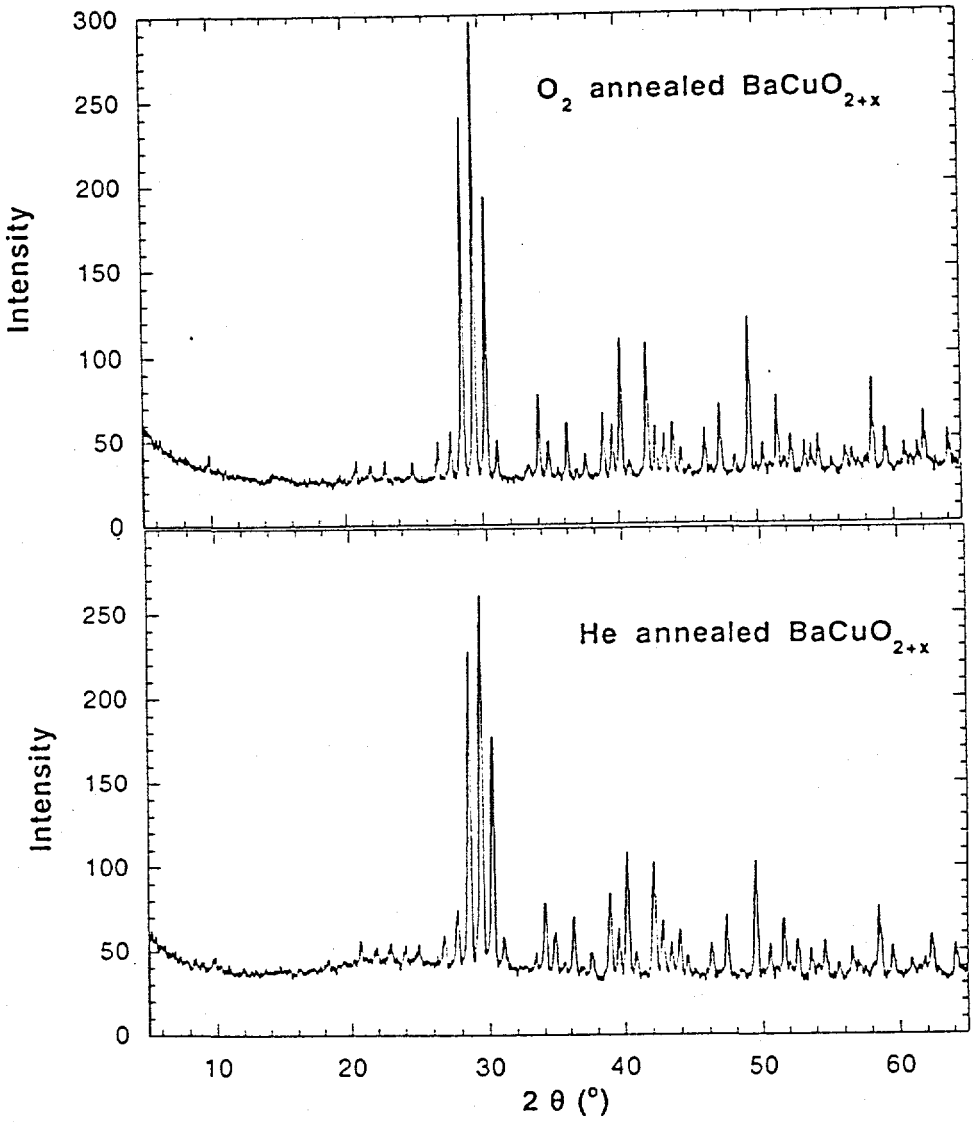

Figure 4.3: Powder x-ray diffraction patterns for $BaCuO_{2+x}$.

He-annealed $BaCuO_{2+x}$

We first present the results for the He-annealed sample of $BaCuO_{2+x}$. Shown in Fig. 4.4(a) is the inverse molar magnetic susceptibility χ^{-1} versus T of this sample. At high T ($\geq$ 300 K), $\chi^{-1}(T)$ increases linearly with temperature (Curie-Weiss law):

$$\chi^{-1} = (T - \theta)/C \,, \tag{4.1}$$

where

$$C = \mathrm{N_A} g^2 S(S+1)\mu_B^2/3\mathrm{k_B} = \mathrm{N_A}\mu_{eff}^2/3\mathrm{k_B} \tag{4.2}$$

is the molar Curie constant, $\mathrm{N_A}$ is Avogadro's number, g and S are respectively the gyromagnetic factor and the spin of the paramagnetic species, μ_B is the Bohr magneton and $\mathrm{k_B}$ is Boltzmann's constant. By fitting Eq. (4.1) to the data in the temperature range between 300 and 400 K, we get $C = 0.39$ cm^3 K/mole Cu, $g = 2.10 \pm 0.04$ (assuming $S = 1/2$ for Cu^{+2}), $\theta = 81$ K, and $\mu_{eff} = 1.82\ \mu_B$/Cu atom, as indicated by the solid line in Fig. 4.4(a). The g value obtained here is the same, within the error of measurement, as the powder average ($g = [(g_x^2 + g_y^2 + g_z^2)/3]^{1/2} = 2.15$) of the values ($g_x = 2.27$, $g_y = 2.12$, $g_z = 2.05$) obtained from the ESR measurements [70]. Thus, at high T, He-annealed $BaCuO_{2+x}$ behaves as if all Cu^{+2} spins are equivalent and interacting ferromagnetically.

However, in contrast to the prediction of molecular field theory, (long range) FM order is not observed at (or below) $T = \theta = 81$ K. Rather, χ^{-1} exhibits positive curvature with decreasing T and then exhibits linear Curie-Weiss behavior again between 2 K and 6 K [Fig. 4.4(b)], with $C = 1.13$ cm^3 K/mol Cu, $\theta = 0.4$ K, and $\mu_{eff} = 3.01\ \mu_B$. The FM sign of θ and the large increase of C with decreasing T suggests that the Cu_{18} and Cu_6 clusters in $BaCuO_{2+x}$ have maximal spin 9 and

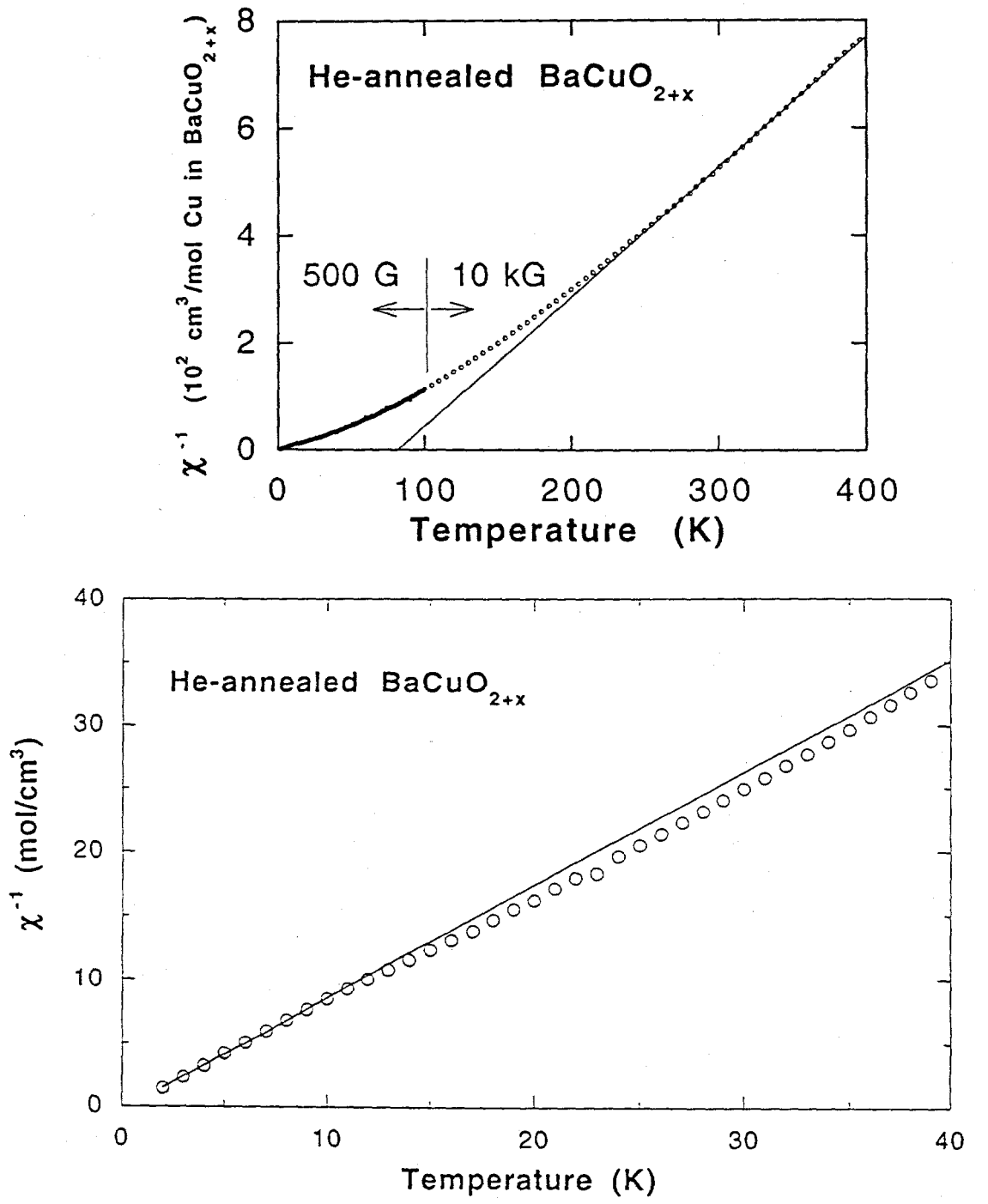

Figure 4.4: Inverse magnetic susceptibility χ^{-1} versus temperature for He-annealed $BaCuO_{2+x}$ between 2 K to 400 K.

spin 3 ground states and spin 8, 7, ...,0 and spin 2, 1, 0 excited states, respectively. Indeed, the shape of $\chi^{-1}(T)$ in Fig. 4.4(a) is very similar to that of a $(Cr^{+3})_4$ cluster with a maximal spin 6 ground state and spin 5, 4, ..., 0 excited states [77].

In order to further clarify the magnetic character of $BaCuO_{2+x}$, $M(H)$ isotherms were obtained at various temperatures between 2 K and 300 K, as shown in Fig. 4.5(a). At low temperature ($T \leq 15$ K), the $M(H)$ data exhibit negative curvature. The slope of the data χ_o at the highest fields (30 kG to 55 kG) exhibits a peak at a temperature between 15 to 25 K, as shown in Fig. 4.5(b), suggesting the onset of long-range AF order below $T_N \sim 15$ to 25 K. A higher resolution measurement of $M(T)$ at fixed $H = 55$ kG is shown in Fig. 4.6. The data show a clear slope change at $T_N \approx 12 \pm 2$ K.

The AC susceptibility for the He-annealed sample was measured at various DC magnetic fields H, as shown in Fig. 4.7. The antiferromagnetic transition postulated above becomes very clear for $H \geq 40$ kG. The data in Figs. 4.5(b), 6, and 7 together suggest that some of the Cu spins in $BaCuO_{2+x}$ order antiferromagnetically at $T_N \simeq 15$ K, and the remainder remain paramagnetic down to 2 K.

Oxygen-annealed $BaCuO_{2+x}$

Now we present the DC magnetic results for the O_2-annealed sample of $BaCuO_{2+x}$. Shown in Fig. 4.8 is χ^{-1} versus T for this sample. At high temperature (≥ 300 K), $\chi^{-1}(T)$ follows the Curie-Weiss law, Eq. 4.1, with $C = 0.35$ cm^3 K/mol Cu, $g = 1.93$, $\theta = 65$ K, and $\mu_{eff} = 1.67\ \mu_B$/Cu atom, as shown by the fitted straight line in Fig. 4.8. By comparism with the above corresponding values for the He-annealed sample, one sees that the effective magnetic moment decreases as the oxygen content

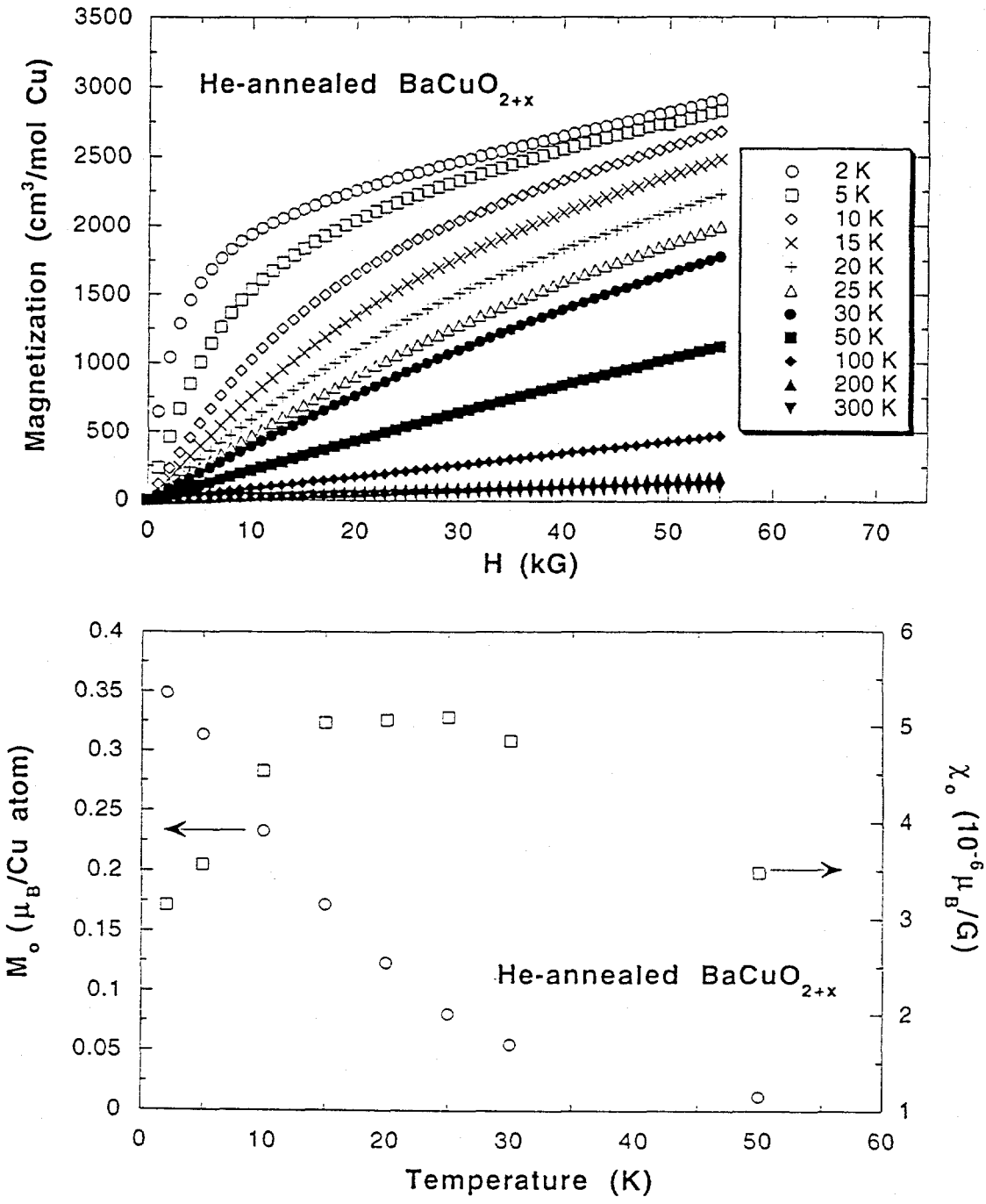

Figure 4.5: Top. Magnetization *vs.* applied magnetic field H at various temperatures for He-annealed $BaCuO_{2+x}$. Bottom. Slope χ_O (right-hand-scale) and y-intercept M_O (left-hand scale) of straight-line fits to the data in the top panel between 30 kG and 55 kG.

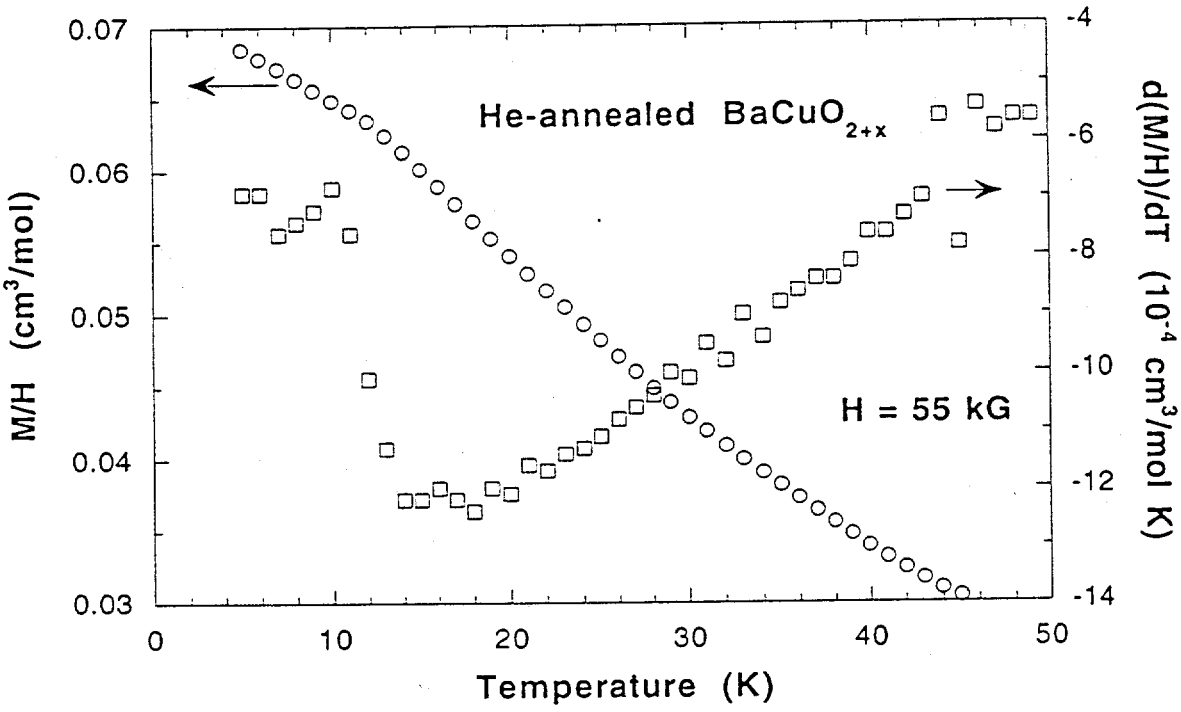

Figure 4.6: High field ($H = 55$ kG) DC magnetization M divided by H versus temperature for He-annealed $BaCuO_{2+x}$ (open circles). The temperature derivative of these data versus temperature (open squares) is also shown.

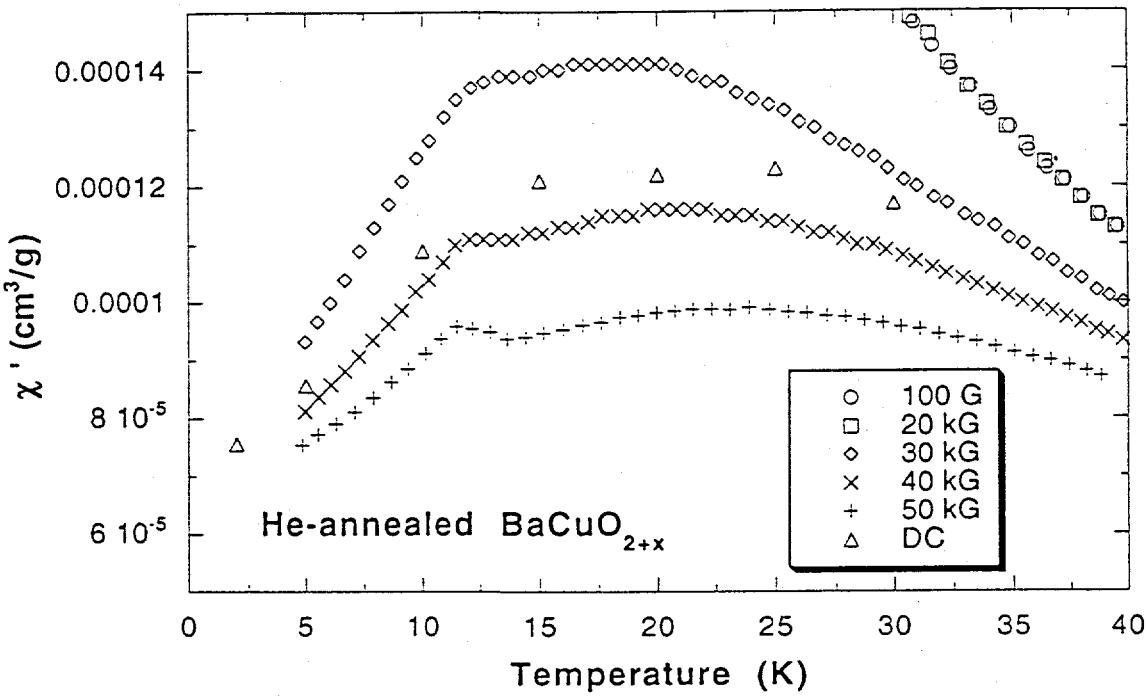

Figure 4.7: AC magnetic susceptibility χ' in various DC fields versus temperature. The open triangles are the high-field differential susceptibility data $\chi_o(T)$ reproduced from Fig. 4.5(Bottom).

increases, as first observed by Migeon [68].

The $M(H)$ isotherms measured at various temperatures between 2 K and 300 K are shown in Fig. 4.9(a). The high-field (30 - 50 kG) slope (χ_o) and corresponding y-intercept (M_o) are plotted versus temperature in Fig. 4.9(b).

Detailed Analysis and Modeling for Helium-annealed Sample

Magnetization versus Magnetic Field and Temperature for $T \ll T_N$

From Fig. 4.5(a), the $M(H)$ data at the lowest temperatures contain a component which saturates by $H \sim 20$ kG, and a component with magnetization proportional to H. In this high field linear region, we parametrize this behavior as follows:

$$M(H) = M_o + \chi_o H \ . \tag{4.3}$$

By subtracting the fitted $\chi_o H$ from the observed $M(H)$, we can examine the behavior of the saturating contribution, normalized to the highest-field value, as shown in Fig. 4.10 for the data in Fig. 4.5(a) at 2 K, where $M(2\ \text{K}) = 31\ \mu_B$/unit cell. Also plotted are Brillouin functions $B_S(H,T)$ for $g = 2$, $T = 2$ K, and spins $S = 6$, 9 and 15. A comparison of the shapes of these Brillouin functions with the data shows that the saturation arises from a large spin $S \sim 9$. The only candidate in the structure which could have this spin value is the Cu_{18} sphere cluster which we therefore conclude remains paramagnetic to 2 K with a ground state with maximal spin $S_s = 18(1/2) = 9$. The Cu_6 rings thus apparently do not contribute to the saturation and their contributions to $M(H)$ must therefore be contained in the $\chi_o H$ term in Eq. (4.3). The Curie constant expected from Eq. (4.2) for the low-field

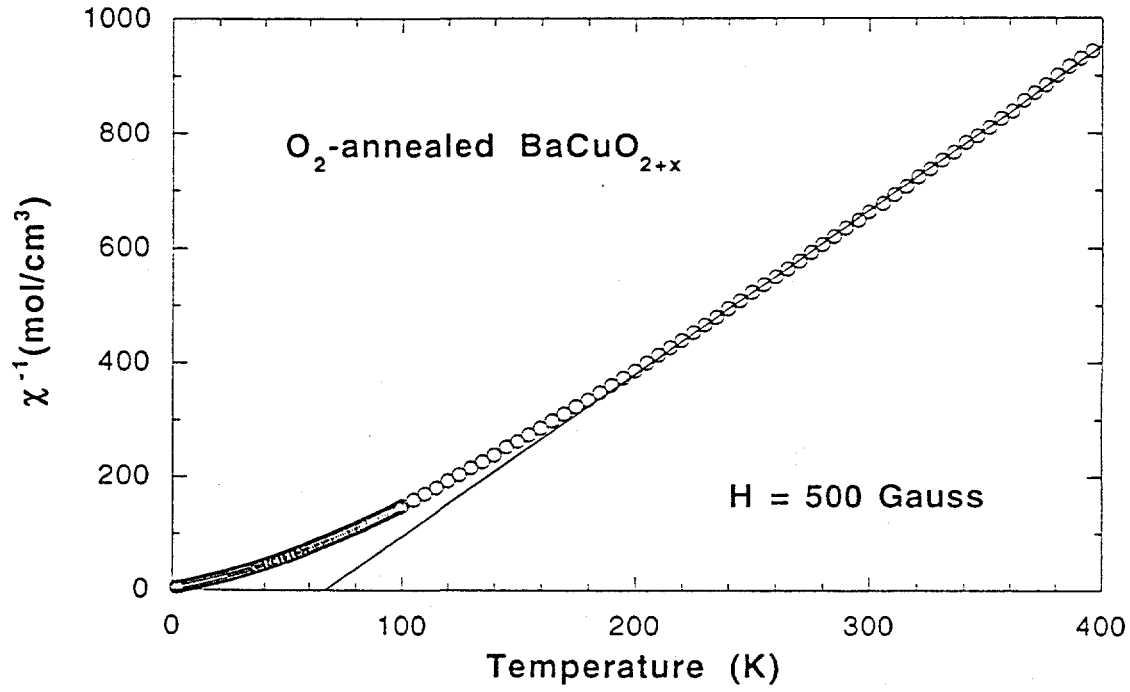

Figure 4.8: Inverse magnetic susceptibility χ^{-1} versus temperature for O_2-annealed $BaCuO_{2+x}$ between 2 K and 400 K. The solid line is a fit of Eq. (4.1) to the data above 300 K.

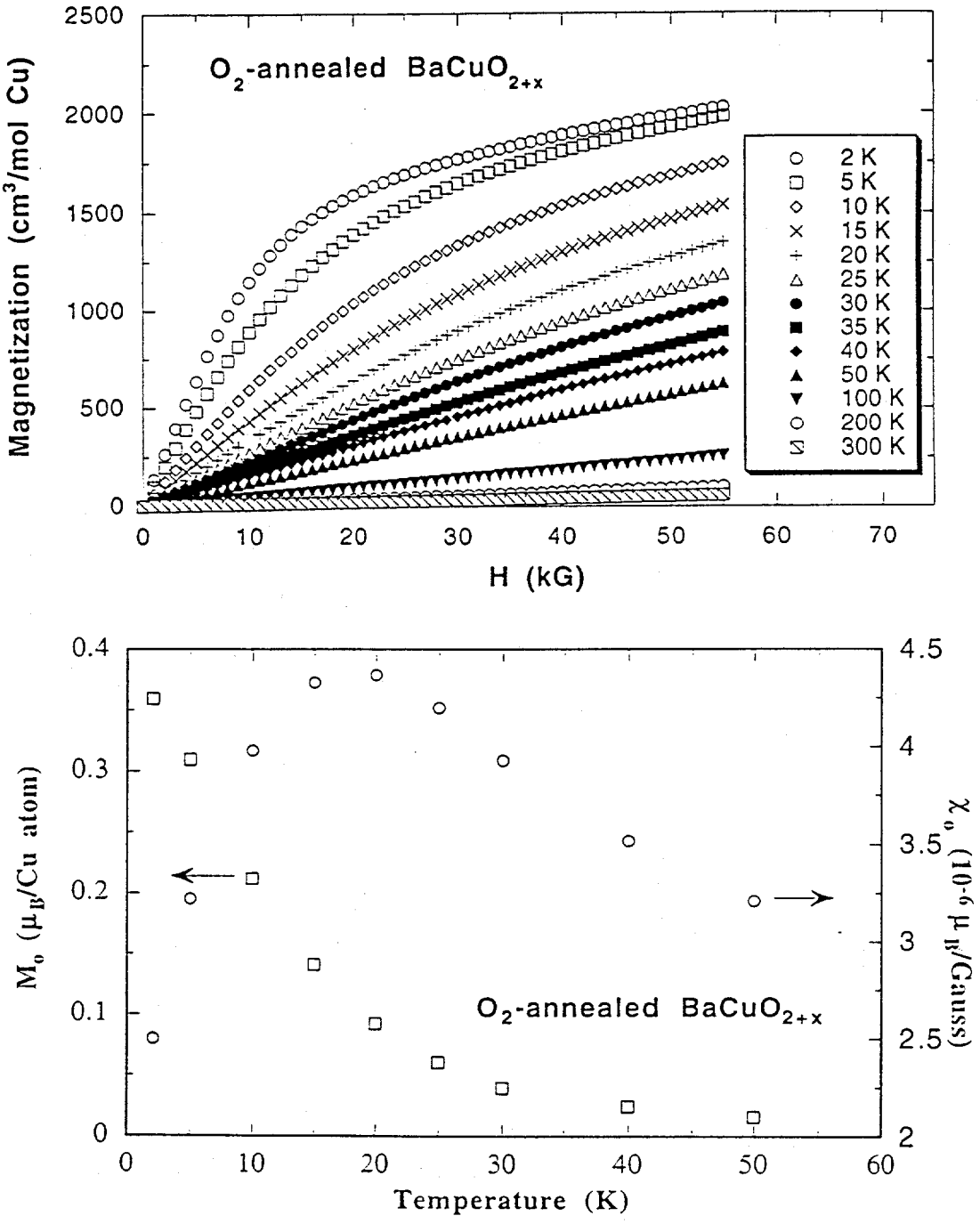

Figure 4.9: Top. Magnetization versus applied magnetic field H at various temperatures for O_2-annealed $BaCuO_{2+x}$. Bottom. Slope χ_o (right-hand-scale) and y-intercept M_o (left-hand-scale) of straight-line fits to the data in top panel between 30 kG and 55 kG.

Curie-Weiss-law susceptibility of the Cu_{18} clusters with $g = 2.1$ (from above) is C = 49.6 cm^3 K/mol Cu_{18} clusters = 1.10 cm^3 K/(mol Cu in $BaCuO_{2+x}$). This value is in close agreement with the value (1.13 cm^3 K/mol Cu in $BaCuO_{2+x}$) observed between 2 K and 6 K in Fig. 4.4(bottom), confirming that the Cu_{18} sphere clusters are primarily responsible for the Curie-Weiss susceptibility observed in Fig. 4.4(bottom) between 2 K and 6 K, and that the Cu_6 clusters do not contribute to the Curie-Weiss susceptibility in this T range. The Weiss temperature $\theta = +0.4$ K found from Fig. 4.4(bottom) suggests that the Cu_{18} sphere clusters should undergo long-range ferromagnetic intercluster order at roughly this temperature.

On the other hand, the above value of $M_o(2K) = 31\ \mu_B$/unit is about 6 μ_B less than the value $M_o = 2\ gS_s\mu_B$/unit cell = 37 μ_B/unit cell expected for the two Cu_{18} clusters per unit cell, again using $g = 2.10$. Since the six lone Cu ions in the unit cell would have a saturation moment of $6gS_{Cu}\mu_B$/unit cell $\approx$ 6 μ_B/unit cell, three lone Cu ions are apparently antiferromagnetically coupled to each Cu_{18} cluster in the unit cell (see Fig. 4.1), and their moments oppose that of the Cu_{18} cluster at low T and H. Since the magnetic behaviors of the Cu_{18} clusters and the lone Cu ions are now accounted for, the AF ordering inferred to occur below $\sim$ 15 K from Fig. 4.5(b) above must be due to the Cu_6 ring clusters, which are the only remaining magnetic species in the unit cell.

To summarize the above discussion, our model thus far for the magnetic properties of $BaCuO_{2+x}$ consists of the following. All of the Cu ions have an oxidation state of +2 and have spin $S_{Cu} = 1/2$. Each Cu_{18} sphere cluster has a maximal spin ground state with spin $S_s = 9$, with lower spin excited states. This ground state is consistent with the ferromagnetic nature of the nearest-neighbor Cu-Cu ex-

change coupling within each cluster expected from the nearly 90^o Cu-O-Cu bond angle, as noted in the Introduction. For the same reason, we also expect each Cu_6 ring cluster to have a maximal spin ground state with spin $S_r = 3$. From Fig. 4.4, both the Cu_6 and Cu_{18} clusters are in their ground states below ~ 40 K. Below $T_N \sim 15$ K, the magnetic moments of the Cu_6 ring clusters with spins $S_r = 3$ order antiferromagnetically with respect to each other. The magnetic moments of the lone copper ions with spins $S_I = 1/2$ and of the Cu_{18} sphere clusters with spins $S_s = 9$ do not participate in this AF ordering; these species remain paramagnetic down to our low temperature measurement limit of 2 K. The spin of each Cu_{18} sphere cluster is antiferromagnetically coupled to those of three lone Cu ions; the spin of each lone Cu ion is antiferromagnetically coupled to that of one Cu_{18} sphere cluster. The gyromagnetic factor g of the Cu_{18} sphere clusters and the lone Cu ions are both close to 2, and a similar value is expected for the Cu_6 clusters. For $T \ll T_N$, the magnetization of the antiferromagnetically ordered Cu_6 ring clusters is proportional to H, and we denote the magnetization of a single ring by $M_r = \chi_r H$.

We now proceed to calculate the magnetization versus magnetic field and temperature expected at $T \ll T_N$ for $BaCuO_{2+x}$. On the basis of the above model, the measured magnetization $M(H,T)$ of a unit cell of $BaCuO_{2+x}$ at $T \ll T_N$ is the sum of the respective contributions from the 6 lone Cu ions, 2 Cu_{18} sphere clusters and 8 Cu_6 ring clusters:

$$M(H,T) = 6M_I(H,T) + 2M_s(H,T) + 8\chi_r(T)H \ , \qquad (4.4)$$

where $M_I(H,T)$ and $M_s(H,T)$ are respectively the magnetizations of a single lone Cu ion and Cu_{18} sphere cluster, respectively. The AF coupling between M_s and M_I is taken into account using molecular field theory. The effective magnetic fields seen

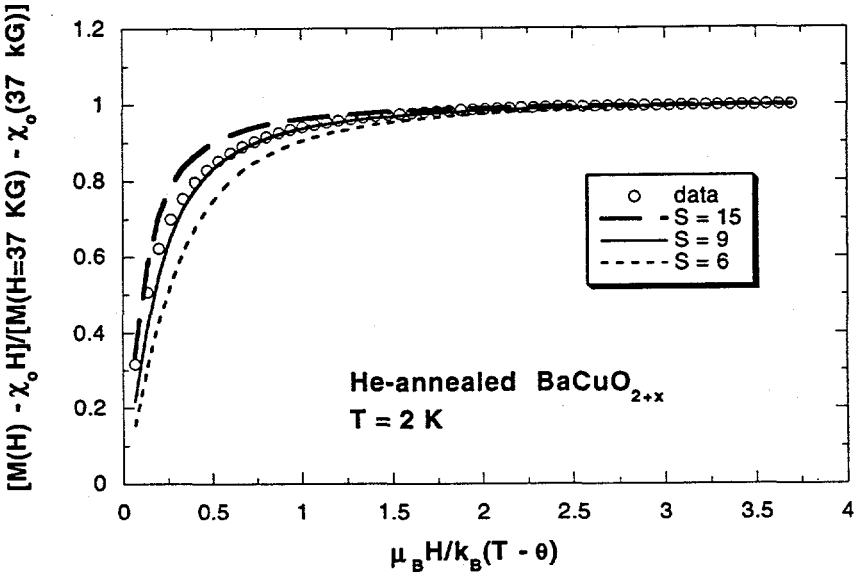

Figure 4.10: The saturating part $M(H)$ - $\chi_o H$ of the magnetization $M(H)$ at 2 K for He-annealed $BaCuO_{2+x}$, from Fig. 4.5(Top), normalized to $M(H$ = 37 kG) - χ_o(37 kG), open circles, plotted versus reduced magnetic field $\mu_B H/k_B(T-\theta)$, where θ = 0.3 K. Brillouin functions with T replaced by $T-\theta$, g = 2 and spins S =6, 9 and 15 are also plotted versus reduced field.

by $M_I(H,T)$ and $M_s(H,T)$ are then respectively

$$\begin{aligned} H_{eff,I} &= H - \lambda M_s \\ &\text{and} \\ H_{eff,s} &= H - 3\lambda M_I \ , \end{aligned} \tag{4.5}$$

where H is the applied magnetic field and $\lambda > 0$ is the antiferromagnetic molecular field coupling constant between M_I and M_s. In the molecular field approximation, these magnetizations are given by

$$\begin{aligned} M_I(H,T) &= gS_I\mu_B B_{S_I}(H_{eff,I},T) \\ &\text{and} \\ M_s(H,T) &= gS_s\mu_B B_{S_s}(H_{eff,s},T) \ , \end{aligned} \tag{4.6}$$

where the g values of the Cu_6 and Cu_{18} cluster ground state spins are assumed to be the same, and $B_J(H,T)$ is the Brillouin function for spin J.

Equations (4.5) and (4.6) constitute a set of coupled nonlinear equations. We solve them using an iterative procedure with ascending orders of approximation. To zeroth order,

$$H^{(0)}_{eff,I} = H^{(0)}_{eff,s} = H \ , \tag{4.7}$$

$$\begin{aligned} M^{(0)}_I(H,T) &= gS_I\mu_B B_{S_I}(H^{(0)}_{eff,I},T) \ , \\ &\text{and} \\ M^{(0)}_s(H,T) &= gS_s\mu_B B_{S_s}(H^{(0)}_{eff,s},T) \ . \end{aligned} \tag{4.8}$$

To first order,

$$H^{(1)}_{eff,I} = [H - \lambda g S_s\mu_B B_{S_s}(H^{(0)}_{eff,s},T)] \ ,$$

and (4.9)

$$H^{(1)}_{eff,s} = [H - 3\lambda g S_I \mu_B B_{S_I}(H^{(0)}_{eff,I}, T)] ,$$

$$M^{(1)}_I(H,T) = g S_I \mu_B B_{S_I}(H^{(1)}_{eff,I}, T)$$

and (4.10)

$$M^{(1)}_s(H,T) = g S_s \mu_B B_{S_s}(H^{(1)}_{eff,s}, T) .$$

By induction to nth order,

$$H^{(n)}_{eff,I} = [H - \lambda g S_s \mu_B B_{S_s}(H^{(n-1)}_{eff,s}, T)] ,$$

and (4.11)

$$H^{(n)}_{eff,s} = [H - 3\lambda g S_I \mu_B B_{S_I}(H^{(n-1)}_{eff,I}, T)] ,$$

and

$$M^{(n)}_I(H,T) = g S_I \mu_B B_{S_I}(H^{(n)}_{eff,I}, T) ,$$

and (4.12)

$$M^{(n)}_s(H,T) = g S_s \mu_B B_{S_s}(H^{(n)}_{eff,s}, T) .$$

The zeroth order magnetizations correspond to no coupling between them. The influence of the coupling (λ) is taken into account with increasing accuracy as the order of iteration increases. The accuracy of the calculated magnetization in second order is estimated to be 5 % and in 20th order to be 0.01 %. By solving Eqs. (4.12) numerically for $M_I(H)$ and $M_s(H)$ at $T = 2$ K using $g = 2.10$ (above) for various λ and $\chi_r(2\text{ K})$ and inserting these into Eq. (4.4), we obtained a reasonably good fit to the $M(H)$ data at 2 K in Fig. 4.9(top) using $\lambda = 0.22\ \mathrm{N}_A \frac{G^2}{erg}$ (= 390 [dimensionless])

(2nd order iteration) and $\lambda = 0.21\ N_A \frac{G^2}{erg}$ (20th order iteration) and $\chi_r(2\ K) = 8.1 \times 10^{-2}$ cm^3/mol Cu in $BaCuO_{2+x}$ for both order approximations. The fit is shown as the solid curve in Fig. 4.11, where the separate contributions of the Cu_6 clusters, the Cu_{18} clusters and the Cu ions are also shown.

The magnetizations at 2 K of a lone Cu ion M_I and a Cu_{18} sphere cluster M_s versus applied magnetic field H in Fig. 4.11 can be understood as follows. The effective magnetic fields experienced by a Cu_{18} sphere cluster and a lone Cu ion are different. Below $H \sim 50$ kG, the effective field $H_{eff,s} = H - 3\lambda M_I$ seen by a sphere cluster is on the order of H because the opposing exchange field due to AF coupling with the three lone Cu ions is relatively small compared with H. Therefore, the effective field seen by the Cu_{18} clusters is always in the direction of H. On the other hand, for H below $\sim$ 20 kG, the effective field $H_{eff,I} = H - \lambda M_s$ experienced by a lone Cu ion is dominated by the negative AF exchange field due to the large M_s of the sphere cluster to which the lone ion is coupled. This is the reason that M_I is initially *diamagnetic* in Fig. (4.11). When M_s becomes saturated, the exchange field $-\lambda M_s$ seen by a lone Cu ion no longer depends on H, and H can become larger than the opposing exchange field, resulting in a *paramagnetic* M_I, as seen in Fig. (4.11) above $\approx$ 20 kG. We note that to obtain the diamagnetic behavior of the lone Cu ions below 20 kG in Fig. 4.11, Eqs. (4.11) and (4.12) must be solved to at least second order.

The relation of the molecular field coupling constant λ and conventional coupling constant J in the spin Hamiltonian can be estimated by going to the high field limit, where the Brillouin function saturates to 1. Then the maximum exchange field

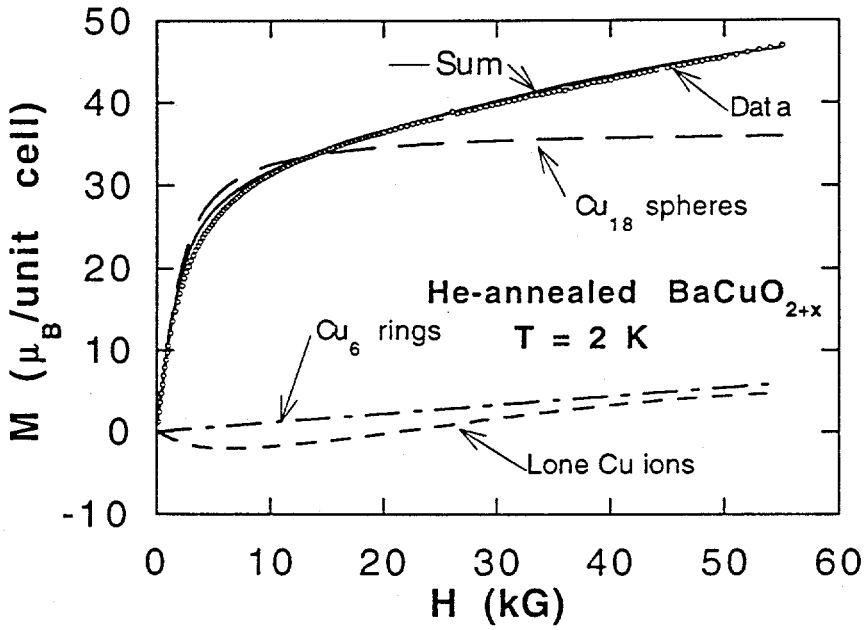

Figure 4.11: Magnetization (M) versus applied magnetic field (H) for He-annealed $BaCuO_{2+x}$ (open circles). The solid curve labeled Sum is a theoretical fit to the data [Eq. (4.12)]. The contributions to the Sum from the lone Cu ions, the Cu_6 clusters, and the Cu_{18} sphere clusters are as indicated.

experienced by a lone ion is

$$H_{ex,max} = \lambda g S_I \mu_B = 2.2 \times 10^4 \ \ Gauss. \tag{4.13}$$

This corresponds to an exchange energy

$$E = g S_s \mu_B H_{ex,max} = \lambda g^2 S_I S_s \mu_B^2 = 1.5 \text{ K} . \tag{4.14}$$

If we convert this into the Heisenberg type interaction

$$E = 2J \ \mathbf{S}_s^i \ \mathbf{S}_I^i \tag{4.15}$$

we get

$$2J = 2\lambda g^2 \mu_B^2 = 0.33 \text{ K} = 0.028 \text{ meV} . \tag{4.16}$$

Low Temperature ($T \ll T_N \approx 15$ K) Magnetic Susceptibility

We write the magnetic susceptibility χ of a unit cell in a manner analogous to Eq. (4.4):

$$\chi(T) = 6\chi_I(T) + 2\chi_s(T) + 8\chi_r(T) , \tag{4.17}$$

where χ_I, χ_s, and χ_r are respectively the susceptibilities of a lone Cu ion, a Cu_{18} sphere cluster and a Cu_6 ring cluster. In the low temperature range $T \ll T_N \approx$ 15 K, χ_r of the antiferromagnetically ordered Cu_6 ring clusters should be nearly independent of T, and the Cu_{18} sphere clusters are in their ground states with spin $S_s = 9$. The magnetic susceptibility χ is defined as $\chi = \lim_{H \to 0} M(H)/H$. In this low-field limit with $\mu_B H / k_B T \ll 1$, Eqs. (4.5) and (4.6) can be solved analytically [78] to yield the first two terms on the right-hand-side of Eq. (4.17):

$$6\chi_I(T) + 2\chi_s(T) = 2\frac{(C_s + 3C_I)T - 6\lambda C_s C_I}{T^2 - 3\lambda^2 C_s C_I} , \tag{4.18}$$

where C_s and C_I are respectively the Curie constants for a Cu_{18} sphere cluster (S_s = 9) and a lone Cu ion ($S_I = 1/2$). The right hand side of Eq. (4.18) has the same form as for a two-sublattice ferrimagnet [78].

Using the above values of $g = 2.10$ and $\lambda = 0.22\ N_A \frac{G^2}{erg}$, subtraction of $3\chi_I(T)$ + $\chi_s(T)$ in the units appropriate to Fig. 4.12 from the observed χ yields, according to Eq. (4.17), the Cu_6 ring susceptibility $\chi_r(T)$ which is shown in Fig. 4.12, along with $[6\chi_I(T) + 2\chi_s(T)]^{-1}$. As independently deduced above in Fig. 4.5(bottom), $\chi_r(T)$ shows a maximum at $T_N \approx 13$ K in Fig. 4.12, indicative of long-range AF ordering of the Cu_6 ring cluster magnetic moments below T_N. The extrapolated observed χ^{-1} data and predicted $[3\chi_I(T) + \chi_s(T)\ ]^{-1}$ data in Fig. 4.12 indicate that the Cu_{18} sphere clusters will order ferromagnetically below ~ 1 K.

High Temperature ($\geq$ 40 K) Susceptibility and Intracluster Coupling Constants

The Heisenberg model has been widely used to interpret the magnetic properties of the layered high T_c cuprates. Similar to the Cu^{+2} ions in high T_c cuprates, the Cu^{+2} ions in $BaCuO_{2+x}$ are spin 1/2 ions, as shown above. Therefore the exchange interaction between adjacent Cu ions should be nearly isotropic, and $BaCuO_{2+x}$ should also be well described by the Heisenberg model. The magnetic susceptibility can be obtained in principle by diagonalizing the Heisenberg Hamiltonian

$$\mathcal{H} = -2J \sum_{<i,j>} \mathbf{S}_i \cdot \mathbf{S}_j\ , \tag{4.19}$$

as in the Bonner-Fisher [79] type of calculation, where $J > 0$ is the nearest-neighbor Cu-Cu FM exchange coupling constant and the sum is over nearest-neighbor Cu-Cu pairs. However, due to limitations of computer memory we can only obtain the

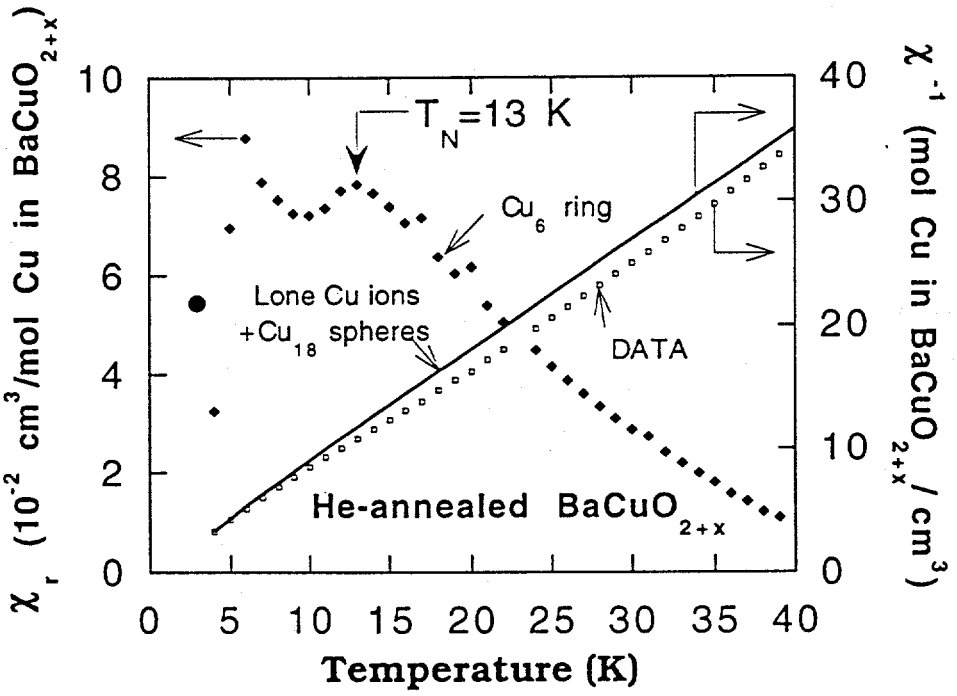

Figure 4.12: Inverse magnetic susceptibility χ^{-1} versus temperature T for He-annealed $BaCuO_{2+x}$ (open squares), reproduced from Fig. 4.4(Bottom). The solid curve is the predication of χ^{-1} for the lone Cu ions and Cu_{18} sphere clusters. The filled diamonds are the derived $\chi_r(T)$ data for the Cu_6 rings.

solution for up to an 11 spin cluster. Therefore we use Van Vleck's approximation [80] for the energy levels of a cluster:

$$E_{S,\alpha} = -\frac{J_\alpha z_\alpha}{n_\alpha - 1}[S(S+1) - n_\alpha s_{Cu}(s_{Cu}+1)]\,, \tag{4.20}$$

where n_α is the (even) number of Cu spins in the cluster, $S = 0, 1, 2, ..., n_\alpha s_{Cu} = S_{\alpha,max}$ is the spin of the cluster, z_α is the (average) number of nearest neighbors, $s_{Cu} = 1/2$ is the spin of a copper ion, and $\alpha = s$ (sphere cluster) or r (ring cluster). Here we assume that J can be different within a sphere (J_s) and within a ring (J_r) cluster because of the different geometries of these two clusters. When the Zeeman energy $\mu_B H$ is much smaller than the thermal energy $k_B T$, the susceptibility of a cluster can be written as [77]

$$\chi\alpha(T) = \frac{N_A g^2 \mu_B^2}{3k_B T} \times \frac{\sum_{S=0}^{S=S_{\alpha,max}} G_{S,\alpha} S(S+1)(2S+1) e^{-E_{S,\alpha}/k_B T}}{\sum_{S=0}^{S=S_{\alpha,max}} G_{S,\alpha}(2S+1) e^{-E_{S,\alpha}/k_B T}}\,, \tag{4.21}$$

where $G_{S,\alpha}$ is the degeneracy of energy level $E_{S,\alpha}$, not counting the Zeeman degeneracy, and we assume $g_s = g_r = g$.

For the sphere cluster, $n_s = 18$, $z_s = 2.667$, and $G_{S,\alpha} = 4862$, 11934, 13260, 9996, 5508, 2244, 663, 135, 17, and 1 for $S = 0, 1, 2, 3, 4, 5, 6, 7, 8, 9 = S_{sphere,max}$, respectively. For the ring cluster, $n_r = 6$, $z_r = 2$, and $G_{S,r} = 5$, 9, 5, and 1 for $S = 0, 1, 2, 3 = S_{ring,max}$, respectively. For a lone Cu ion, Eqs. (4.20) and (4.21) yield a Curie Law denoted by $\chi_I(T)$.

The total susceptibility $\chi(T)$ of a unit cell is given again by Eq. (4.17). Using Eqs. (4.20) and (4.21), the $1/\chi(T)$ from Eq. (4.17) was fitted to our experimental data, using $g = 2.10$ $J_r = 148$ K, and $J_s = 38$ K as shown in Fig. 4.13(top).

The Cu_6 ring cluster susceptibility χ_r can be calculated exactly using a Bonner-Fisher [79] type calculation. By comparing this susceptibility with that calculated

using Eq. (4.21) and the approximate energy levels in Eq. (4.20), we may estimate the error in our J_r and J_s coupling constants derived above for the ring cluster, see Fig. 4.13(bottom) , from which we conclude that our J_s value has an error of less than 30 K, which leads to $J_r = 148 \pm 30$ K. If we assume that J_s has a similar percentage error, one obtains $J_s = 38 \pm 8$ K.

Summary and Conclusions

The motivation for studying the properties of magnetic clusters is interdisciplinary, in chemistry, biology, and physics [81]. The unique and complex structure of $BaCuO_{2+x}$ makes this study very challenging but also very interesting. First the model of the magnetic structure and magnetic phase transition gives us insight about the magnetic interactions inside the clusters and between clusters, which is not only relevant to the mechanism of high T_C superconductivity but also helps us to understand the quantum mechanics on a nanometer scale.

Our results show that the ring and the sphere clusters in $BaCuO_{2+x}$ have ferromagnetic ground states with spin 3, 9 respectively, where the FM intracluster interaction strengths are 148 K and 38 K, respectively. This indicates that for nearly 90^o Cu^{+2}-O^{-2}-Cu^{+2} bonds the superexchange interaction is ferromagnetic; this is relevant to many cuprate superconductors which show buckling of the CuO_2 planes and significant deviations of the Cu^{+2}-O^{-2}-Cu^{+2} bond angle from 180^o.

R. Gottschall and Robert Schöllhorn [82] have sucessfully made the barium nickel oxide with $BaCuO_2$ type structure. Therefore substituting Cu by Ni and other metallic ions and studying how the magnetic properties change with the substitution will be very interesting.

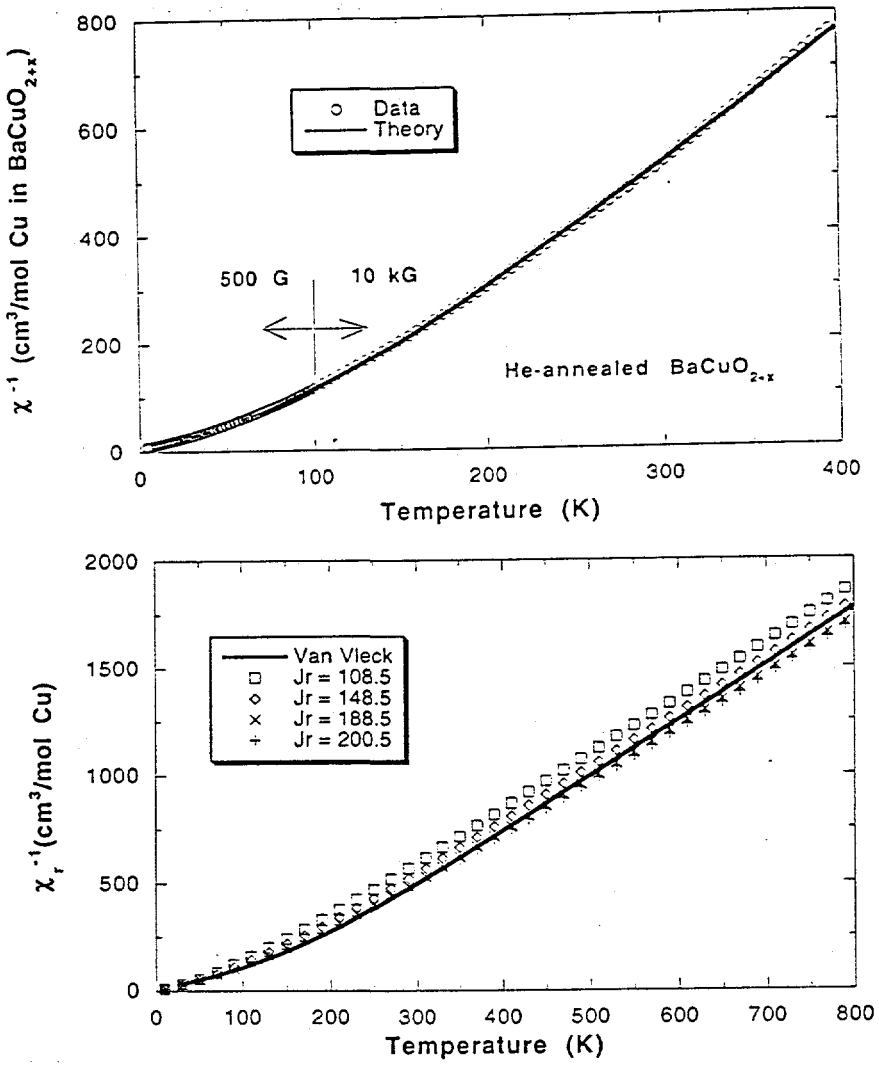

Figure 4.13: Top. Inverse magnetic susceptibility χ^{-1} versus temperature for He-annealed $BaCuO_{2+x}$, reproduced from Fig. 4.4(Top). The solid curve is a theoretical fit [Eq. (4.16)] to the data above 70 K. Bottom. Theoretical predictions for the inverse susceptibility χ^{-1} of the Cu_6 rings versus temperature. The solid curve is the prediction using Eq. (4.21) and the approximate cluster magnetic energy levels in Eq. (4.20). The results of exact calculations using the Heisenberg model are shown by the various symbols for the corresponding values of exchange constant J_r.

Neutron Diffraction Study of Magnetic Ordering of Helium-annealed Sample

Neutron diffraction measurements were carried out by D. Vaknin, J. Fernandez-Baca and X. L. Wang on the powder diffractometer HB-4, the triple axis spectrometer, HB1A and on the spin polarized triple-axis spectrometer HB-1, all at the High Flux Isotope Reactor (HFIR) at Oak Ridge National Laboratory. The 10g pellet-like polycrystalline sample was wrapped in a thin Al foil and loaded into an Al can under He atmosphere that was then mounted in various cryostats for different measurements.

The reflections allowed by the bcc crystal structure of $BaCuO_{2+x}$ are of the type h+k+l = even. At temperatures below 15 K, extra reflections at the (1 1 1) and at the (2 2 1) position are observed. Figure 4.14 shows a 2θ scan of the (1 1 1) reflection at two different temperatures. The inset of Fig. 4.14 shows the temperature dependence of the integrated intensity of this reflection, with a clear indication that a phase transition occurs at $T = 15.0 \pm 0.5$ K. Scans around the (1 0 0) and (2 0 1) reflections, with better statistics, did not show any appreciable intensity at $T = 4.2$ K, and high order magnetic reflections were not identified due to the extensive overlap and dominance of nuclear reflections. High resolution neutron powder diffraction measurements above and below the transition temperature were performed and confirmed that no structural distortion occurs in the temperature range 4 - 16 K, suggesting that the (1 1 1) reflection is associated with an AF long range order. Polarized beam measurements on the same sample proved unequivocally that the (1 1 1) reflection is magnetic in origin [74], as shown in Fig. 4.15.

To model the magnetic neutron reflections we assumed that the long range order

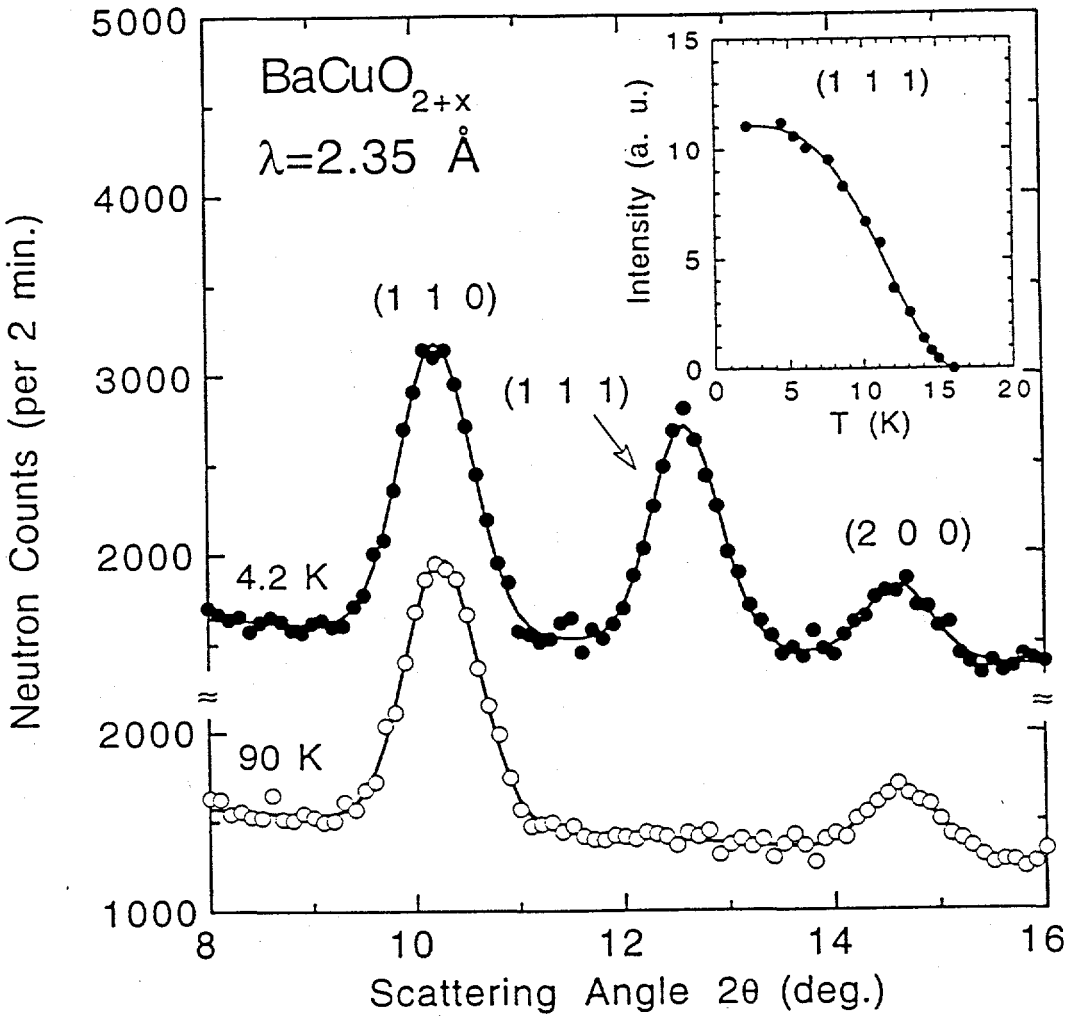

Figure 4.14: Unpolarized-neutron scans for the (1, 1, 1) reflection at temperatures of 4.2 K and 90 K. The solid curve for each scan is a multiple Gaussian fit to the experimental data. Inset: temperature dependence of the integrated intensity of the (1, 1, 1) reflection (the solid curve is a guide to the eye).

is primarily associated with the magnetic ring system, as discussed above. That is due to the general observation in model calculations that the (1/4 1/4 1/4) position always gives rise to a (1 1 1) reflection, and allows for models that predict the clear absence of the (1 0 0) reflection, whereas all AF model, incorporating the spheres predict prominent (1 0 0) and (2 0 1) reflections in contrast to the experimetal observations. The model that we proposed above is that the spins on each ring are internally ferromagnetically oriented and the spin on nearest neighbor Cu_6 rings are antiparallel (powder diffraction measurements are insufficient for the determination of the actual direction of the moment [83]). The general form factor in this case is given by

$$F = p_0 \mu f(\mathbf{Q}) \sum_{i=1}^{8} F_i \sigma_i \exp(i\mathbf{r}_i^0 \cdot \mathbf{Q}) \tag{4.22}$$

where, $p_0 = 0.27\text{x}10^{-12}$ cm, μ and $f(\mathbf{Q})$ are, respectively, the magnetic moment and the magnetic form factor of an individual spin on the ring, $\sigma_i = \pm 1$, and F_i is the structure factor of each ring given by

$$F_i = \sum_{j=1}^{6} \exp(i\mathbf{r}_{i,j} \cdot \mathbf{Q}) \,, \tag{4.23}$$

where $\mathbf{r}_{i,j}$ are the relative positions of each spin with respect to the center point of the ring $\mathbf{r}_i^0$, so that the absolute position of spin j in ring i from the origin of the unit cell is given by $\mathbf{r}_i^0 + \mathbf{r}_{i,j}$. The $\mathbf{r}_{i,j}$'s are of three types $(\pm\epsilon, \pm\epsilon, 0)$, $(0, \pm\epsilon, \pm\epsilon)$ and $(\pm\epsilon, 0, \pm\epsilon)$ where $\epsilon \approx 0.1008$. The plus or minus sign in the brackets should be chosen so that each $\mathbf{r}_{i,j}$ is orthogonal to the axis of highest symmetry of a ring. For instance, for the ring whose center is located at the (1/4 1/4 -1/4) position, the $\mathbf{r}_{i,j}$'s are $(\epsilon, -\epsilon, 0)$, $(\epsilon, \epsilon, 0)$, $(0, \epsilon, \epsilon)$, $(0, -\epsilon, -\epsilon)$, $(\epsilon, 0, -\epsilon)$ and $(-\epsilon, 0, \epsilon)$. Each pair of Cu^{2+} rings sharing the same body diagonal are related by inversion symmetry

Table 4.1: Observed and calculated integrated intensities of the the magnetic reflections at T = 4.2 K. The intensities of the magnetic reflections were normalized to a nuclear diffraction pattern of the angular 2θ range 8 - 60 degrees, excluding the magnetic reflections. The magnetic moment determined from the model described in the text is $\mu = 0.89 \pm 0.05\mu_B$.

reflection	$\sin\theta/\lambda$ $\AA^{-1}$	Calculated intensity	Integrated Intensity
(1 0 0)	0.0274	forbidden	*
(1 1 1)	0.0475	938	930 ±36
(2 0 1)	0.0613	forbidden	*
(2 2 1)	0.0823	148	137 ±16
(3 1 1)	0.0910	22	*
(3 2 2)	0.1131	72	*
(4 0 1)		forbidden	*
(4 2 1)	0.1257	40	*

and therfore have the same F_i. The general structure factor of any reflection can be readily calculated,

$$\begin{aligned} F &= 2p_0\mu f(\mathbf{Q}) \cdot i \cdot \sin[\frac{\pi}{2}(h+k+l)] \\ &\quad \cdot[F_1 - F_2\exp(i\pi h) - F_3\exp(i\pi k) - F_4\exp(i\pi l)] \,. \end{aligned} \tag{4.24}$$

Due to the $\sin[\frac{\pi}{2}(h+k+l)]$ factor, only (odd, odd, odd) and (even, even, odd) type of reflections are allowed. For the former case we get

$$F = 16p_0\mu f(\mathbf{Q}) \cdot \{\cos[2\pi h\epsilon]\cos[2\pi k\epsilon] + \cos[2\pi k\epsilon]\cos[2\pi l\epsilon] + \cos[2\pi l\epsilon]\cos[2\pi h\epsilon]\}, \tag{4.25}$$

so that when $\epsilon = 0$, F reaches the maximum value of $48p_0\mu f(\mathbf{Q})$. In Table 4.1 we list the calculated integrated intensities, $I = A \cdot M \cdot L \cdot F^2\langle\sin^2\eta\rangle$, where A is a scale factor obtained from the refinement of the nuclear reflections, M the mutiplicity, and η the angle between the magnetic moment and $\mathbf{Q}$. The average magnetic moment obtained from fitting our model [Eq. (4.24)] to the observed intensity yields a moment

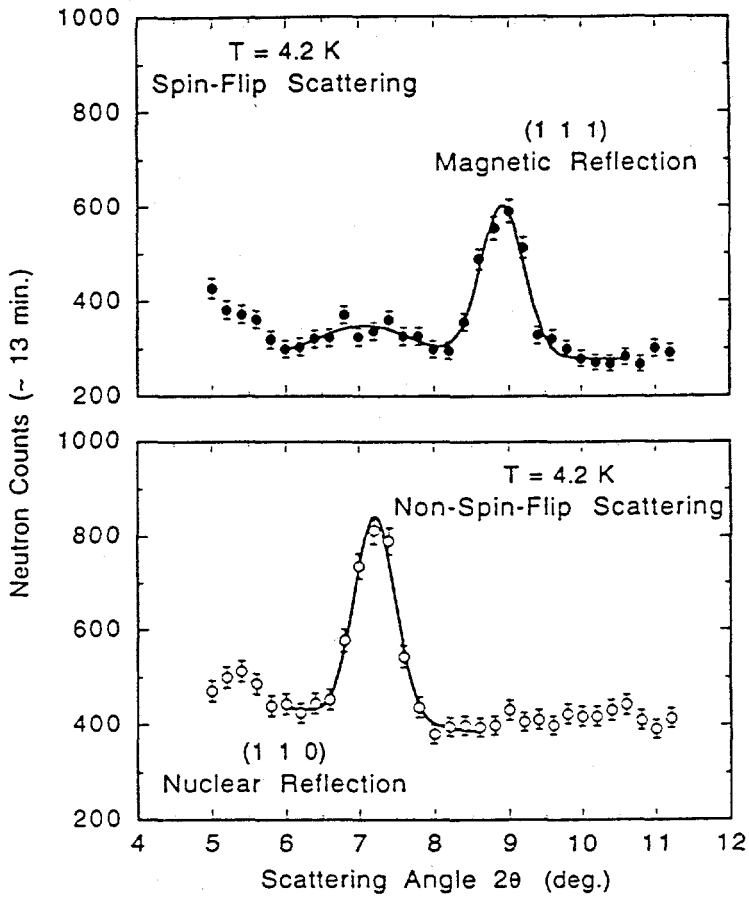

Figure 4.15: Polarized-neutron scans at $T = 4.2$ K. The top and the bottom scans show the spin-flip (magnetic) and the non-spin-flip (nuclear) scattering, respectively. The solid curves are guides to the eye.

$\mu = 0.89 \pm 0.05\ \mu_B$ using the form factor of localized Cu^{2+}, Ref. [66]. The slightly reduced value of the magnetic moment from that expected (1.1 μ_B) for a free Cu^{2+} spin reinforces our belief that the sole contributors to the magnetic neutron scattering observations are the Cu_6 ring clusters.

Heat Capacity Study of Magnetic Ordering of Helium-annealed Sample

The heat capacity C for the He-annealed sample was measured by R. E. Fisher and coworkers at U. C. Berkeley at two different magnetic fields $H = 0\ G$ and $H = 7\ T$, as shown in Fig. 4.16. There is a clear heat capacity jump at the antiferromagnetic transition temperature $T_N = 13$ K for both $H = 0$ T and $H = 7$ T. The value of the heat capacity jump at T_N according to mean field theory is [84]

$$\Delta C = 5K \frac{S(S+1)}{S^2 + (S+1)^2} \tag{4.26}$$

Where S is the total spin of the cluster. In our experimental ΔC is 1.2 J/K mole, which is the same within 40 % as the mean field value for the ring cluster assuming the spin on the cluster is 3 In the low temperature range a plot of C versus T (Fig. 4.17) shows is a maximum at about 0.8 K, presumably from ferromagnetic ordering between the sphere clusters (above).

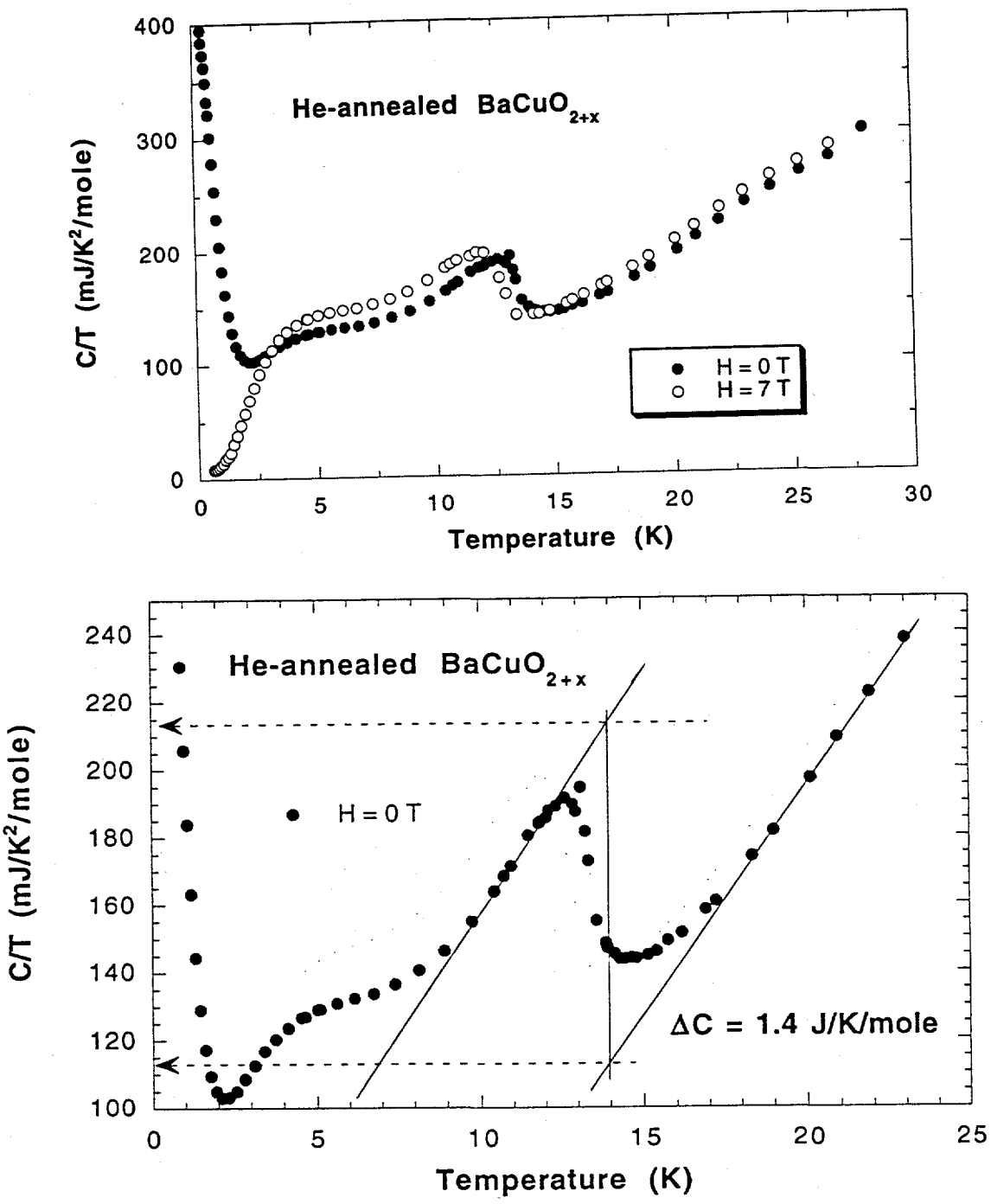

Figure 4.16: Heat capacity divided by temperature C/T, versus temperature. In the top panel, data were obtained in magnetic fields $H = 0$ (open circles) and 70 kG (filled circles).

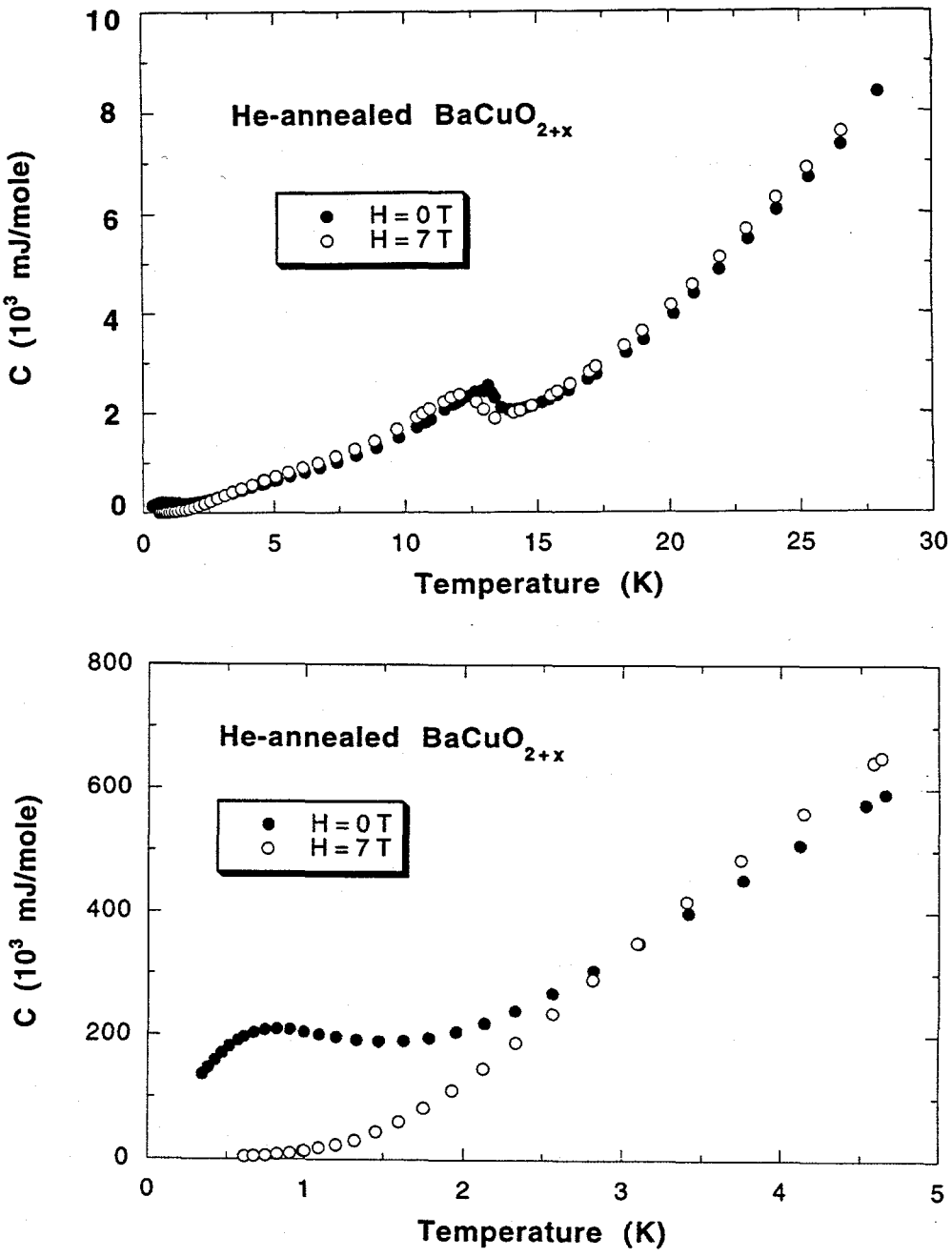

Figure 4.17: Heat capacity C versus temperature for applied field $H = 0$ (filled circles) and $H = 7$ T (open circles).

CHAPTER 5. MAGNETIC SUSCEPTIBILITY OF Sr_2CuO_3

Introduction

Since the discovery of high temperature superconductivity, many studies have been performed both to search for new superconductors and elucidate the mechanism underlying the high transition temperature (T_c). At this time, all known systems with $T_c > 40$ K possess 2-dimensional CuO_2 sheets which are generally agreed to play the active role in superconductivity. On the other hand, it has recently been reported [85] that $Sr_2CuO_{3+\delta}$ exhibits high temperature superconductivity for appropriate values of δ. The parent insulating phase for these superconductors, Sr_2CuO_3, has a crystal structure [86] in which one dimensional Cu-O chains, similar to those in $YBa_2Cu_3O_7$, lie parallel to the a axis (Figure 5.1). The location(s) of the excess oxygen in $Sr_2CuO_{3+\delta}$ are not yet known, so it is not known whether this doped compound has an essentially quasi-one-dimensional or -two-dimensional structure. Although no one has reported superconductivity in materials which only have Cu-O one dimensional chains, the observation of superconductivity in Oxygen-doped $Sr_2CuO_{3+\delta}$ raises important questions concerning the minimum magnetic and electronic dimensionalities which will support high T_c. Furthermore, since the insulating parents of all other known high T_c cuprate superconductors are two dimensional spin 1/2 Heisenberg antiferromagnets [11], it is important to understand the magnetism

in this one dimensional system as a prerequisite to determining its evolution as the system is doped into the metallic and superconducting state. Toward that end, we have studied the static magnetic properties of this material and observe direct evidence of Bonner-Fisher type behavior [79], indicating that Sr_2CuO_3 is a nearly ideal one-dimensional (1-D) spin 1/2 Heisenberg antiferromagnet.

Experimental Details

Sr_2CuO_3 was prepared by M. K. Crawford and Coworkers at DuPont using conventional solid state reaction. A one to one molar ratio of $SrCO_3$ and CuO was mixed and fired at 950^o under flowing oxygen ($\sim$ 1 l/min) for a total of 24 hours with one intermediate grinding. The calcined powders were pulverized, pelletized and sintered under the same conditions. Some samples were subjected to nitrogen treatment. Pellets were placed in an alumina boat and heated to between 400 ^{o}C and 1000 ^{o}C under flowing nitrogen ($\sim$ 1 l/min) for 12 hours. The decomposition temperature for this system is about 900 ^{o}C under the nitrogen atmosphere we employed. This nitrogen gas is obtained from liquid nitrogen boiloff and has a small residual oxygen partial pressure. We expect that the decomposition temperature of Sr_2CuO_3 would decrease below 900 ^{o}C if the oxygen partial pressure were further reduced and, in fact, samples heated above about 520 ^{o}C in 6 torr He in the Faraday magnetometer do decompose as shown in Fig. 5.2. The oxygen contents of the samples were determined iodometrically. Powder x-ray diffraction data for initial characterization were obtained with a Scintag diffractometer using CuKα radiation at ambient temperature.

Magnetic susceptibilities below 300 K were measured using a SQUID magne-

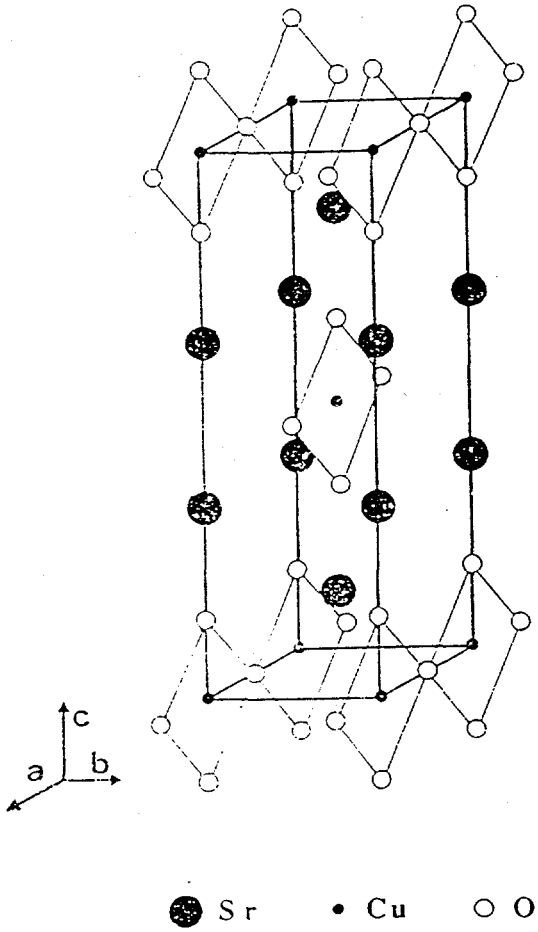

Figure 5.1: The crystal structure of Sr_2CuO_3. The Cu-O chains are parallel to the a axis.

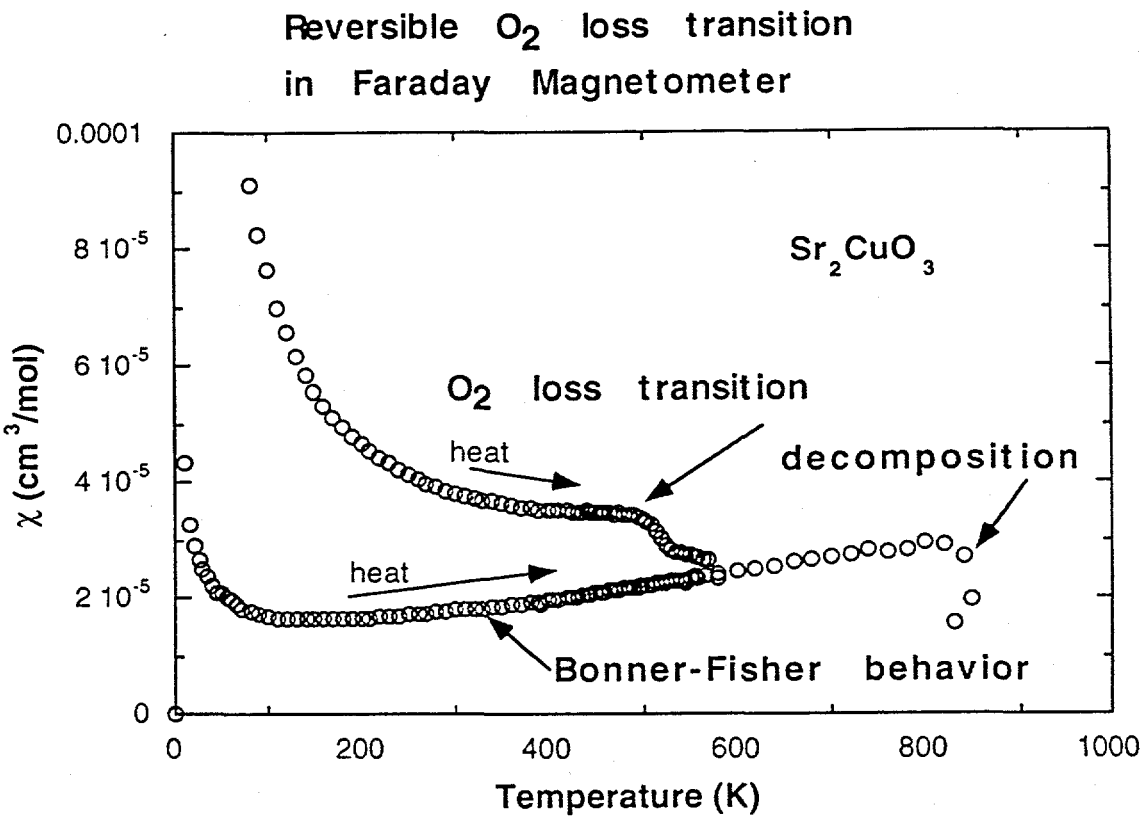

Figure 5.2: Magnetic susceptibility χ versus temperature for the first time running (upper curve) and second time running (lower curve).

tometer (Quantum Design) at Dupont, whereas the high temperature susceptibility (to 800 K) was measured using our Oxford Instruments Faraday balance. The sample holder was 99.999 % pure gold wire. Its magnetic susceptibility was independently measured and substracted from the raw data for the $Sr_2CuO_{3\pm\delta}$ samples. The contribution of ferromagnetic impurities to the measured magnetization was determined from magnetization-field isotherms between 25 K and 750 K (Fig. 5.3) and was found to correspond to that of 2 at. ppm or less, with respect to Cu, of ferromagnetic iron metal impurities; this contribution is corrected for in Fig. 5.7 below. The magnetic measurements from the SQUID and the Faraday magnetometers were in good agreement below 300 K.

Low temperature neutron powder diffraction studies were carried out at 11 K by the Dupont group using the BT-4 triple axis spectrometer at the reactor facility of the National Institute of Standard and Technology. The collimation was 20'-40'-10', and the neutron wavelength (1.540 $\AA$) was chosen by a Cu (220) monochromator. The sample was mounted in an Al sample container containing He exchange gas. Low temperature synchrotron x-ray powder diffraction [119] data were collected at 12 K by the Dupont group at beamline X-7A at the National Synchrotron Light Source at Brookhaven National Laboratory.

Results

Synchrotron and Neutron Diffraction Studies

The crystal structure of Sr_2CuO_3 at room temperature was first determined by single crystal x-ray [86] diffraction. Powder neutron [91] and x-ray diffraction [92] data at room temperature have also been reported. All of these studies assigned the

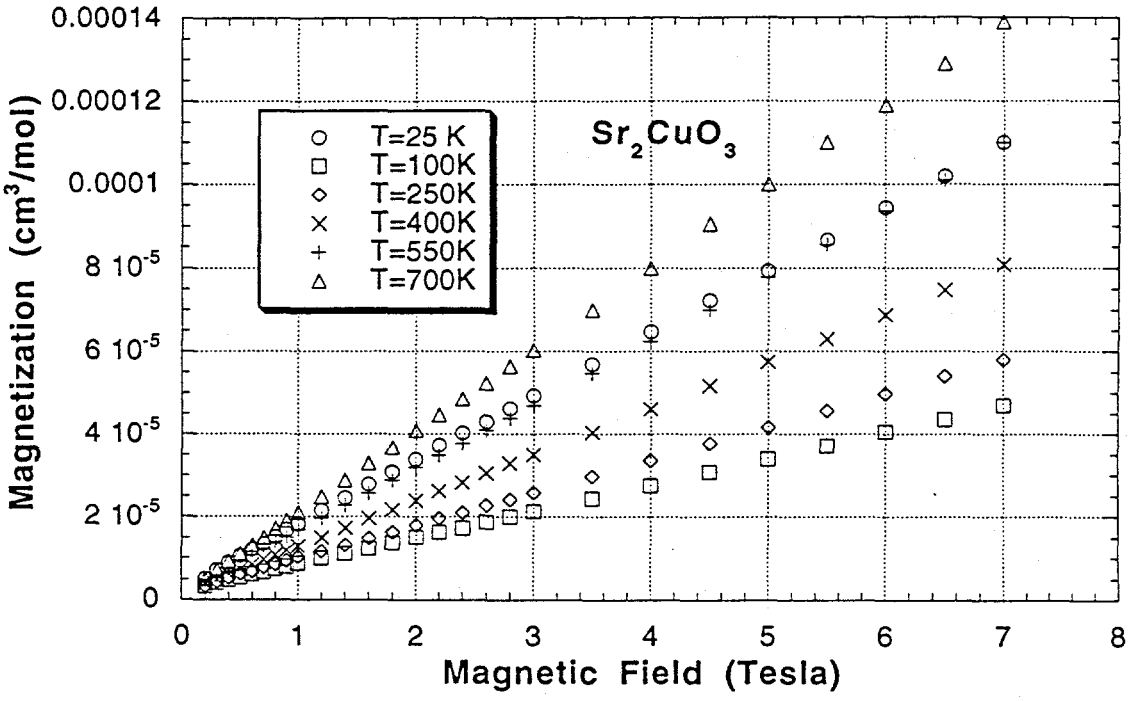

Figure 5.3: Magnetization versus magnetic field isotherms at different temperatures T.

orthorhombic Immm space group to Sr_2CuO_3. We utilized neutron and synchrotron x-ray powder diffraction at low temperature in order to search for any evidence of structural phase transitions or distortions which would further lower the symmetry and, for example, contribute to the magnetic anisotropy by allowing a Dzyaloshinsky-Moriya (D-M) interaction [93] to occur. It is known that the leading order magnetic anisotropy in several of the cuprates, for example La_2CuO_4, arises from the D-M interaction.

Structural information determined by Rietveld refinement [94] of neutron diffraction data (Figure 5.4) obtained at 11 K are shown in Table 5.1. Aluminum reflections from the sample container used were excluded from the refinement. No superlattice peaks which would indicate lattice distortion were observed. High resolution synchrotron x-ray diffraction data (Fig. 5.5) at 12 K yielded a similar conclusion. These results show that there are no structural transformations in Sr_2CuO_3 between room temperature and 11-12 K, and thus suggest that the leading order magnetic anisotropy arises from magnetic dipole interactions and/or from anisotropy in the exchange coupling tensor.

Magnetic Susceptibility

There have been several previous studies [88]-[90] of the magnetic susceptibility of Sr_2CuO_3, but none of these studies observed clear evidence for Bonner-Fisher [79] behavior, and therefore accurate values of J, the Cu^{+2}-Cu^{+2} nearest-neighbor superexchange constant, were not determined. Furthermore, no systematic attempt was made in these earlier studies to account for the possible effect of oxygen nonstoichiometry on the magnetic susceptibilities. To address these problems, we have made

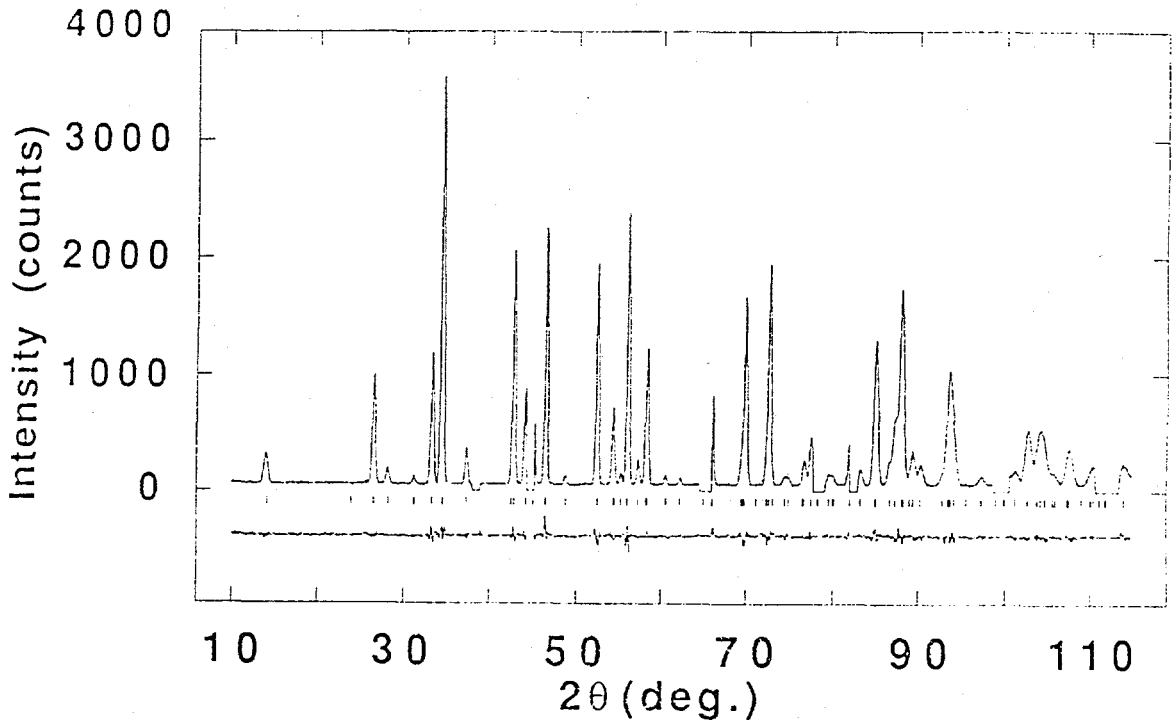

Figure 5.4: Powder neutron diffraction data collected at 11 K. The results of Rietveld refinement are superimposed on the raw data. The vertical tick marks indicate the expected location of diffraction peaks. The fit residuals are plotted at the bottom of the figure. The neutron wavelength was 1.5401 $\AA$.

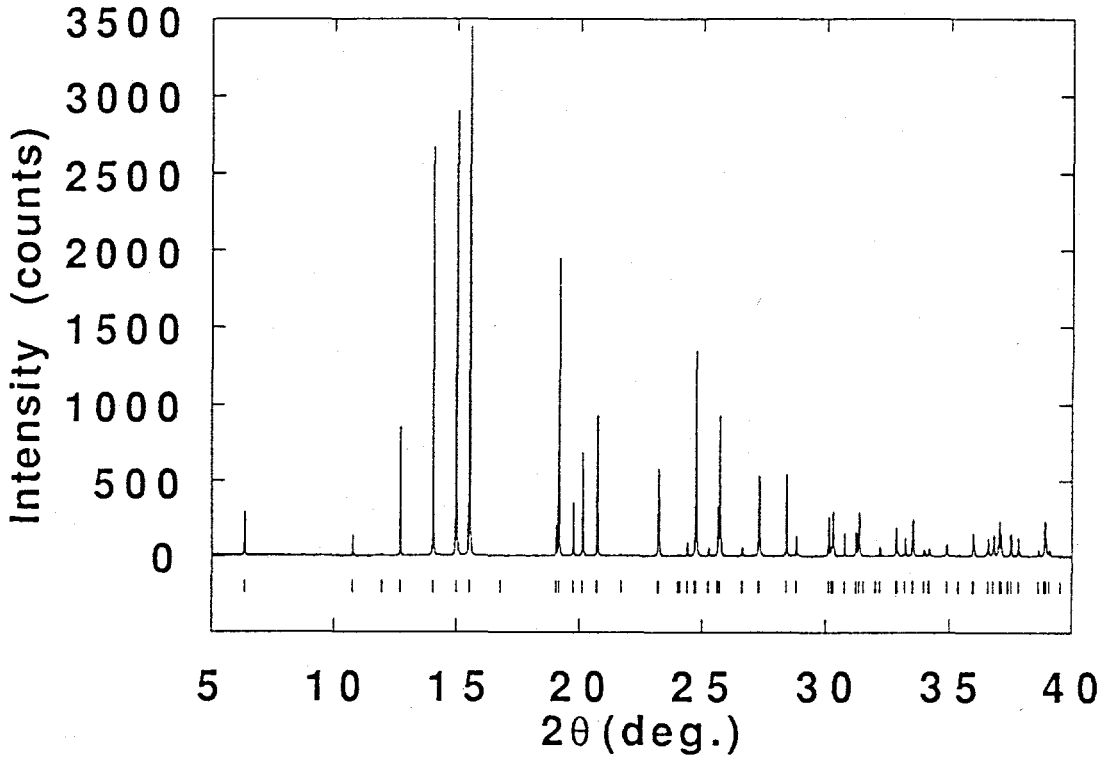

Figure 5.5: Synchrotron x-ray diffraction data collected at 12 K. The vertical tick marks indicate the expected location of diffraction peaks. The x-ray wavelength was 0.70377 $\AA$.

Table 5.1: Low temperature crystallographic data for Sr_2CuO_3 determined by Rietveld refinement of neutron diffraction data obtained at 11 K.

Atom	x	y	z	U_{iso}	Occupancy
Sr	0	0	0.35195(9)	0.006(4)	0.980(4)
Cu	0	0	0	0.001(5)	0.990(6)
O(1)	0	0	0.15445(11)	0.0027(5)	1.000(5)
O(2)	0.5	0	0	0.0021(8)	0.993(8)

magnetic susceptibility measurements over a wide range of temperature on samples which have undergone various annealing treatments and therefore have slightly different oxygen contents (Table 5.2). The susceptibility is strongly affected by such treatments. Figure 5.6 shows the temperature dependencies below 300 K of the magnetic susceptibilities of samples before and after annealing under a N_2 or a 6 torr He atmosphere. The diamagnetic terms originating in the closed shells of the ions have been subtracted (χ_{dia} = -77 $\times$ 10^{-6} cm^3/mole). Plot (a) shows the susceptibility for an as-made sample before nitrogen treatment. As can be seen from this figure, treatment under a reducing atomosphere decreasing the susceptibility, especially the Curie-type component. Thus it is natural to associate the magnitude of this Curie-type term with the presence of excess oxygen in the lattice (this point will be discussed further below). In this picture, as-made sample (a) contains some excess oxygen ion defects, whereas nitrogen annealing reduces the number of such defects and consequently suppresses the Curie-Weiss-like behavior at low temperatures. Futhermore, Figure 5.6 shows the susceptibility for a sample kept at 600 K

Table 5.2: Parameters for $Sr_2CuO_{3+\delta}$ derived from iodometric titrations and magnetic refinement assuming that $g = 2.1$, $|J|/k_B = 1307$ K.

(conditions)	O content δ	impurity level %	θ (K)	χ_{VV} (cm^3/mole)
(a) 950^{o}C in O_2	0.02(2)	0.363	-1.09	2.87 10^{-5}
(b) 600^{o}C in N_2	0.01(1)	0.287	-0.83	2.91 10^{-5}
(c) 800^{o}C in N2	-0.01(1)	0.227	-0.86	2.63 10^{-5}
(d) 327^{o}C in 6 τ He	no data	0.114	-7.81	2.28 10^{-5}

under 6 torr He overnight and then measured *without being removed from the He atmosphere*. This sample shows a much smaller Curie-Weiss-type term compared with the other samples, presumably due to loss of almost all the excess oxygen after the overnight anneal. Since samples annealed in N_2, but then exposed to air before the magnetic measurements were made, have large Curie-Weiss-type terms, this result also suggests that this material absorbs oxygen from air at room temperature fairly quickly, and that considerable care must be taken if one wishes to measure properties for the stoichiometric system.

Magnetic susceptibility χ measurements for $Sr_2CuO_{3\pm\delta}$ made using the Faraday magnetometer in the temperature range of 2 K to 800 K also indicated a strong dependence upon oxygen content δ, as shown above in Fig. 5.2. The as-made sample was first measured from 10 K to 600 K. There is a clear decrease in χ at 540 K, which indicates the loss of oxygen (oxygen loss at 540 K is confirmed by TGA in He at a flow rate of 40 cc/min). Then the same sample was again measured from 10 K to

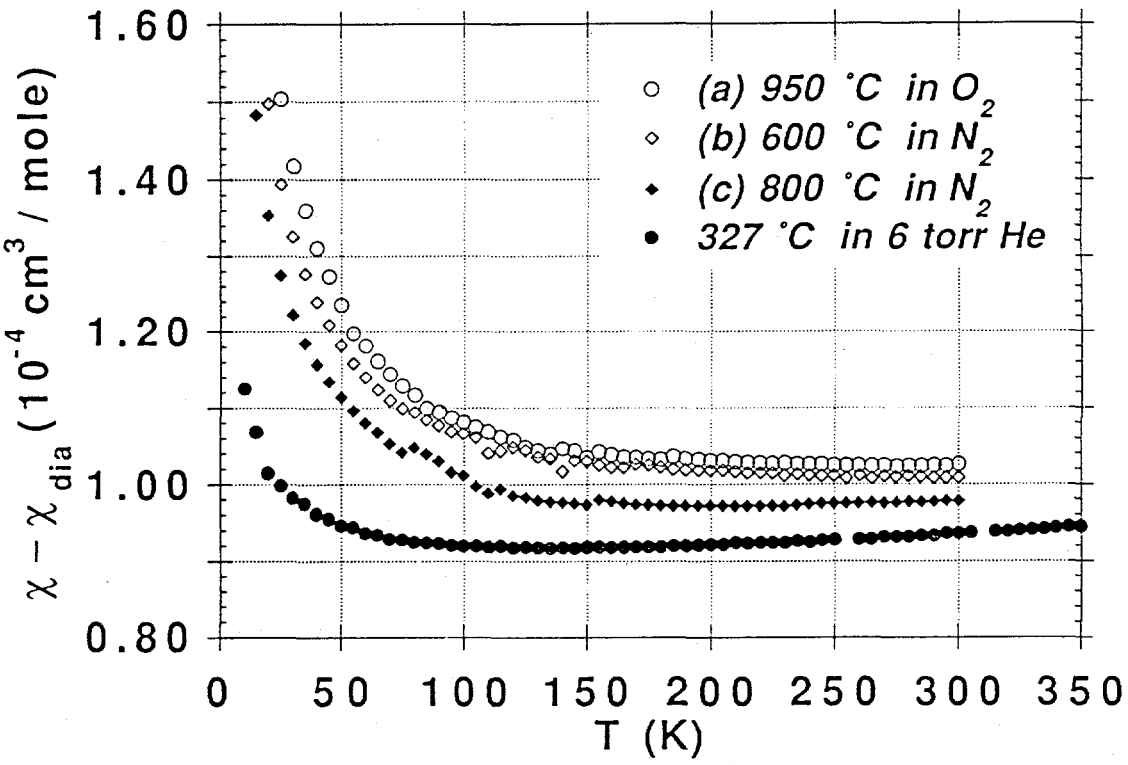

Figure 5.6: The temperature (T) dependencies of the magnetic susceptibilities (χ) for the samples annealed under different conditions. The diamagnetic core contributions (χ_{dia}) have been subtracted. The measurement field was 1.0 T in each case.

800 K. Figure 5.2 shows a clear difference between these two curves.

Figure 5.7 shows the susceptibility versus temperature from 10 to 800 K for the sample annealed at 327 ^{o}C (600 K) under 6 torr He then measured in the same atmosphere. $M(H)$ isotherms were measured between 25 K and 750 K, and the susceptibility was found to be independent of applied magnetic field up to $H = 7.0$ T (after correction for the influence of ferromagnetic impurities, see above). The enhancement of the susceptibility at low temperature presumably originates from a residual Curie-Weiss-like component, as mentioned above, but the gradual increase of the susceptibility with increasing temperature in the high temperature region is not Curie-Weiss like, but rather is similar to a Bonner-Fisher type susceptibility [79], as our fit to the data described below demonstrates.

Data Analysis

The magnetic Hamiltonian which describes a spin 1/2 Heisenberg chain,

$$\mathcal{H} = 2|J| \sum_i \vec{\mathbf{S}}_i \cdot \vec{\mathbf{S}}_{i+1} \,, \tag{5.1}$$

has been described previously [79]. In this expression, J is the antiferromagnetic Cu^{+2}-Cu^{+2} superexchange interaction coupling constant, and the summation extends over pairs of nearest neighbor spins. It is worthwhile spending a moment to justify the use of such a model to describe the magnetic susceptibility of Sr_2CuO_3. The assumption that Sr_2CuO_3 is a one dimensional magnetic system follows directly from the structure of this material (Fig. 5.1). Since the Cu^{+2} ions are only bonded to oxygen ions along the **a** direction with 180 degree Cu-O-Cu bonds, there will be strong Cu^{+2}-Cu^{+2} antiferromagnetic superexchange interactions only in this direc-

tion. The additional assumption that this is an Heisenberg system is based upon the fact that the Cu^{+2} ion is spin 1/2 and thus has no single ion anisotropy to first order. Furthermore, the structural studies reported here and previously [91],[92] for Sr_2CuO_3 demonstrate that there is an inversion center located midway between the Cu^{+2} ions in the Cu-O chains, which precludes the existence of a Dzyaloshinsky-Moriya (D-M) $\vec{S}_i \times \vec{S}_j$ interaction [93]. In contrast, La_2CuO_4, an antiferromagnetic insulator which is structurally similar to Sr_2CuO_3, has a leading order magnetic anisotropy arising from a D-M interaction which is allowed by the rotational distortion of the CuO_6 octahedra in the Bmab (orthorhombic) phase [100]. We also expect that the interchain magnetic coupling will be rather weak in Sr_2CuO_3, partly as a result of magnetic frustration. For example, the *interlayer* interchain superexchange in Sr_2CuO_3 is fully frustrated *despite* the orthorhombic symmetry, again in contrast to the situation in orthorhombic La_2CuO_4 where the *interlayer* superexchange is not frustrated. This is true because, considering a given Cu^{+2} ion, the four nearest-neighbor Cu^{+2} ions in the nearest neighbor chains in adjacent layers are *equidistant* in Sr_2CuO_3, whereas in La_2CuO_4 there are *two* such distances. In Sr_2CuO_3 the *intralayer* interchain interaction is, on the other hand, not frustrated, but is still expected to be rather weak due to the absence of intervening oxygen ions between adjacent Cu^{+2} ions. Thus in general one expects Sr_2CuO_3 to be more Heisenberg-like than La_2CuO_4, the latter nevertheless being considered one of the best examples of a spin 1/2 2-D Heisenberg antiferromagnet [101]. Therefore, we should expect Sr_2CuO_3 to be an excellent realization of a 1-D Heisenberg antiferromagnet and it seems very reasonable to attempt to describe its magnetic susceptibility with the Bonner-Fisher model for a spin 1/2 Heisenberg antiferromagnetic chain.

In order to fit the susceptibility data shown in Fig. 5.7 over a wide temperature range, we assume that the observed temperature dependent magnetic susceptibility, $\chi(T)$, consist of several terms:

$$\chi(T) = \chi_{dia} + \chi_{VV} + \chi_{spin}(T) + \chi_{Pauli} + \chi_{Landau} \cdot \tag{5.2}$$

In the absence of conduction electrons, the Pauli paramagnetism and Landau diamagnetism should be negligible. χ_{dia} is the core diamagnetic susceptibility, χ_{VV} is the Van Vleck paramagnetic susceptibility, and $\chi_{spin}(T)$ is the spin susceptibility. The values of χ_{dia} and χ_{VV} are assumed to be temperature-independent. The χ_{dia} values used were found in standard tables [102]. Furthermore the spin susceptibility was separated into two parts:

$$\chi_{spin}(T) = \rho \cdot (\chi_{CW}) + (1 - \rho) \cdot (\chi_{BF}) \tag{5.3}$$

where χ_{CW} is a Curie-Weiss-like component arising from finite length chains which consist of an odd number of Cu^{+2} spins [79], isolated Cu^{+2} spins, and/or other paramagnetic impurities, and χ_{BF} is the susceptibility of an $S = 1/2$ infinite isotropic Heisenberg chain (the Bonner-Fisher susceptibility [79],[103]). The coefficient ρ represents the defect/impurity level. There are no analytical solutions for the magnetic susceptibility of Heisenberg chains [79]. However, a useful closed-form approximation to χ_{BF} has been suggested [104] to be

$$\chi_{BF} = \frac{Ng^2\mu_B^2}{\mathrm{k}_B T} \frac{0.25 + 0.14995X + 0.30094X^2}{1 + 1.9862X + 0.68854X^2 + 6.0626X^3} \tag{5.4}$$

with $X = \frac{|J|}{k_B T}$. The Curie-Weiss-like term is

$$\chi_{CW} = \frac{Ng^2 S(S+1)\mu_B^2}{3\mathrm{k}_B(T - \theta)} \cdot \tag{5.5}$$

Assuming that $g = 2.1$, a typical value for cuprates [11],[105], and $S = 1/2$, we determine the following parameters by fitting Eq. (5.3) to the magnetic susceptibility data in Fig. 5.7 after subtracting the core diamagnetism:

$$\rho = 1.14 \times 10^{-3} \ (i.e., \textit{impurity level} = 0.11\%) \tag{5.6}$$

$$\theta = -7.81 \text{ K}; \tag{5.7}$$

$$|J|/\mathrm{k}_B = 1307 \text{ K}; \tag{5.8}$$

$$\chi_{VV} = 2.28 \times 10^{-5} \frac{\mathrm{cm}^3}{\mathrm{mole}} . \tag{5.9}$$

The value of χ_{VV} is comparable to that of other single Cu-O layer cuprates [106]. The fit using these parameter values is shown superimposed on the data in Fig. 5.7. The fit function has been extended to temperatures high enough to include the broad peak in the susceptibility arising from the appearance of short range 1-D order with decreasing temperature. Futhermore, several curves calculated assuming different values of J are plotted to give a sense of the sensitivity of the fit to this important parameter. From these curves we estimate the value of $|J|/\mathrm{k_B}$ to be (1300 ± 200) K.

As mentioned previously, a Curie-Weiss-type term can originate from several sources including nearly isolated Cu^{2+} ions associated with oxygen defects (oxygen vacancies or excess oxygen), some other kinds of lattice defects, or magnetic impurites. However, an equally plausible explanation is that the Curie-Weiss-like behavior comes from the random termination of Cu-O chains. As Bonner and Fisher have discussed [79], if the resulting chains have an even number of Cu^{2+} spins, then the total spin on the chain in the antiferromagnetically ordered state is zero at $T = 0$. If, however, the chains have an odd number of Cu^{2+} spins, then in the antiferromagnetically ordered state the net spin on the chain is 1/2. Such chains of odd length

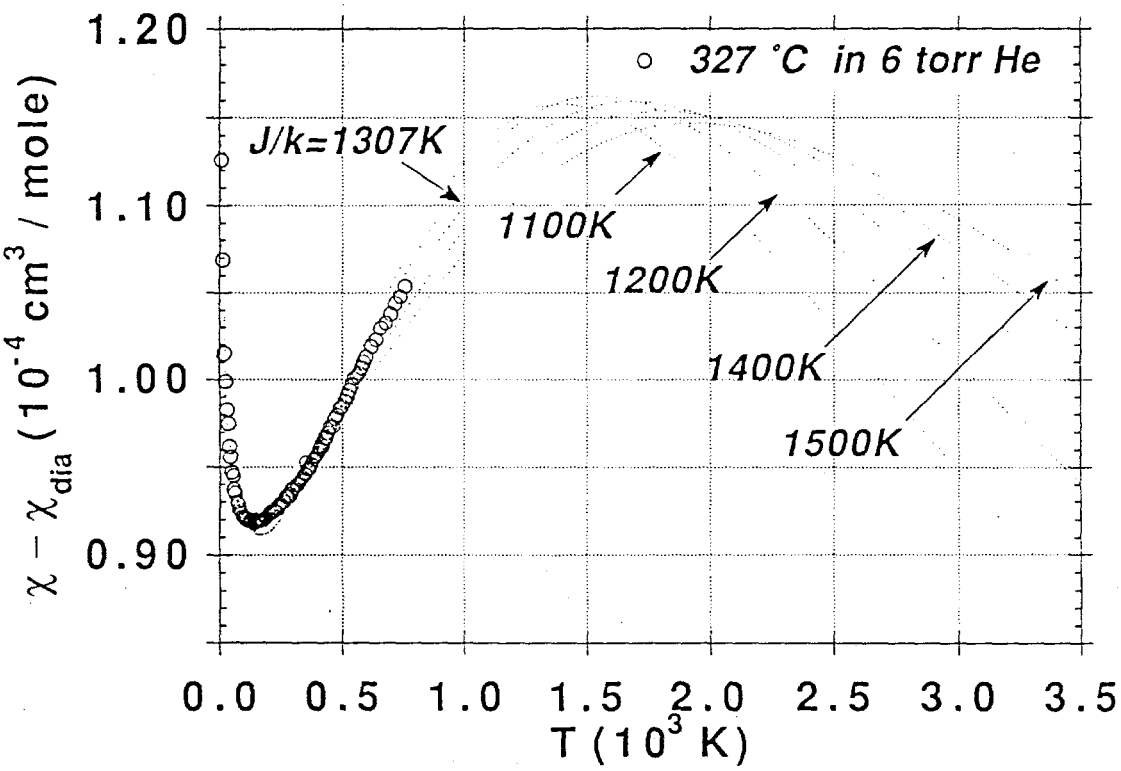

Figure 5.7: The magnetic susceptibility (χ - χ_{dia}) versus temperature up to 800 K for the sample annealed under 6 torr helium. The experimental data are represented by open circles, while the theoretical curves described in the text are shown by dotted lines.

will make contributions to the magnetic susceptibility which are Curie-Weiss-like, although both the amplitude of the susceptibility divergence and the temperature at which the divergence occurs are depressed with increasing chain length by Cu^{2+}-Cu^{2+} antiferromagnetic interactions. In the opposite limit, "chains" which have a length of only one Cu^{2+} ion will precisely exhibit Curie-Weiss behavior. To avoid the additional complications necessary to model contributions to the magnetic susceptibility arising from chains with a random distribution of lengths, we have chosen to represent the impurity spin susceptibility for Sr_2CuO_3 simply as a Curie-Weiss term which adequately represents the contributions from odd length finite chains, as well as additional contributions due to isolated Cu^{+2} ions and/or impurites. This simplification minimizes the number of refinement parameters, and the quality of the fit indicates it to be a reasonable approximation.

The results of these measurements thus indicate that Sr_2CuO_3 is an excellent realization of a 1-D spin 1/2 Heisenberg antiferromagnet. In fact, it may be the best realization of such a system reported to date. In order to place Sr_2CuO_3 in the context of other 1-D antiferromagnets, Table 5.3 shows parameters for several such systems which have appeared in the literature [99]. J_1 and J_2 are the two interchain magnetic coupling constants in orthogonal directions (in the b and c directions in Sr_2CuO_3). For all materials other than Sr_2CuO_3 in Table 5.3 we have assumed that $J_1 = J_2$. We have also calculated independent values of J_1 and J_2 for Sr_2CuO_3, assuming only dipolar interaction coupling, using the expression

$$J = -\sum_i \frac{\mu \cdot \mu_i (3cos^2\phi_i - 1)}{r_i^3} \tag{5.10}$$

where the sum is over the Cu moments μ_i in the same ($J = J_1$) or different ($J =$

Table 5.3: J, J_1, J_2 and T_N values for several linear chain antiferromagnets compared with the values for Sr_2CuO_3. Note that J_1 and J_2 for Sr_2CuO_3 are the values estimated assuming only dipolar coupling between the Cu^{2+} spins.

	T_N(K)	J(K)	S(spin)	I(η_1,η_2)	η_1, η_2	J_1(K), J_2(K)
Sr_2CuO_3	0.028	1307	1/2	4.7×10^4	2.8×10^{-5},	0.036,
					5.1×10^{-7}	6.6×10^{-4}
Sr_2CuO_3	5	1307	1/2	260	6.06×10^{-6}	7.88×10^{-3}
TMMC	0.84	6.5	5/2	90.3	5.03×10^{-5}	3.27×10^{-4}
$BrMnBr_3$	8.8	12	5/2	15.9	1.62×10^{-3}	1.94×10^{-2}
$CsMnBr_3$	8.3	9.6	5/2	13.5	2.25×10^{-3}	2.16×10^{-2}
$CuCl_2{\cdot}2NC_5H_5$	1.7	13	1/2	7.65	7.00×10^{-3}	9.10×10^{-2}
$CsNiCl_3$	4.5	11	1.0	6.52	9.64×10^{-3}	1.06×10^{-1}
$KCuF_3$	39.8	203	1/2	6.40	1.42×10^{-2}	3.2
$KCuF_3$					1.0×10^{-2}	1.9
$RbNiCl_3$	11	11	1.0	2.67	5.67×10^{-2}	0.634

J_2) layers, r_i is the distance between the moment μ and the moment μ_i, and ϕ_i is the angle between r_i and the a axis. For this calculation the magnetic structure was assumed to be the same as that reported for $Sr_2CuO_2Cl_2$ [109]. The summation in Eq. (5.10) included Cu^{+2} moments within a distance r_i sufficient to achieve convergence.

Values of J_1 ($= J_2$) in Table 5.3 were calculated from the following expressions [110]-[112]

$$\frac{kT_N}{|J|} = \frac{4S(S+1)/3}{I(\eta_1, \eta_2)} \tag{5.11}$$

where $\eta_1 = J_1/J$, $\eta_2 = J_2/J$, and

$$I(\eta_1, \eta_2) = \frac{1}{\pi^3} \int\int\int_0^\pi \frac{dq_x dq_y dq_z}{\eta_1(1 - cosq_x) + \eta_2(1 - cosq_y) + (1 - cosq_z)} . \tag{5.12}$$

For the case where $J/J_1 \gg 1$, and $J_1/J_2 \geq 1$, Eq. 5.12 can be approximated by [112]

$$I(\eta_1, \eta_2) = \frac{0.64}{\sqrt{\eta_1}}[1 + 0.253ln(\frac{\eta_1}{\eta_2})] . \tag{5.13}$$

For $J/J_1 \geq 10$, and $J_1/J_2 \geq 10$, we find that Eq. (5.13) is accurate to better than 5%. Thus the interchain coupling energies can be estimated using the experimental values of T_N and J in Eqs. (5.11) and (5.13).

The fact that we observe no evidence for 3-D magnetic order in our samples above $T = 2$ K would be consistent with the value of $T_N = 0.028$ K from Eq. (5.11), calculated assuming only interchain dipolar magnetic coupling (Table 5.4). The much larger value of $T_N = 5$ K reported in Ref. [90] would thus imply that there is interchain coupling, in addition to that due to the magnetic dipole interaction, in Sr_2CuO_3 (see Table 5.3). Additional measurements, including magnetic susceptibility, specific heat and neutron diffraction, to temperatures lower than 2 K

would be of great interest in the study of 3-D magnetic order in this system.

We note here that any long range three dimensional antiferromagentic structure adopted by Sr_2CuO_3 must be one in which the Cu^{+2} moments order antiferromagnetically within each chain; that is, a ferromagnetic intrachain interaction with an antiferromagnetic interchain interaction would not be consistent with our magnetic susceptibility data. Our low temperature structural data provide conclusive evidence that the magnetic properties of this material are not influenced by complications such as structural phase transformation or stablization of a spin-Peierls state, as occurs in $CuGeO_3$ [113]. A number of other spin 1/2 Heisenberg chains based upon Cu^{+2} have also been reported [98],[99],[106], but all of these compounds are not oxides and have much smaller values of J. The value measure here, $|J|/k_B \approx 1300$ K, is quite large and comparable to that measured in the 2-D cuprate systems. It should be pointed out here that in the layered cuprate literature the prefactor of the sum over nearest neighbor pairs in the Hamiltonian of Eq. (5.1) has the factor of two missing. Thus one should compare $2J$ (2600 K) for Sr_2CuO_3 with J ($\sim$ 1500 K) in the layered cuprate literature. It is an open question why the nearest neighbor Cu-Cu superexchange interaction in Sr_2CuO_3 is significantly larger than in the antiferromagnetic layered cuprate systems.

Finally, the evolution of the magnetic and electronic dimensionalities in $Sr_2CuO_{3+\delta}$ as a function of δ is a very important subject for future study. Although there are apparently several superconducting phases [85],[114],[115] in this system, their crystal structures, particularly the precise oxygen ordering arrangements, have yet to be determined. Thus the intriguing question of how a 1-D antiferromagnet evolves into a high temperature superconductor in this system upon doping remains to be

answered.

Conclusion

Magnetic susceptibility measurements for $Sr_2CuO_{3\pm\delta}$ were made from 2 K to 800 K, and a strong dependence upon oxygen content (δ) was observed. Samples synthesized under oxygen, followed by various nitrogen treatments, exhibited markedly different Curie-Weiss-type terms, and we discuss possible origins for this behavior. High temperature magnetic susceptibility measurements for the sample with the smallest Curie-Weiss-type term clearly show the increase with temperature expected from the Bonner-Fisher model for a spin-1/2 one dimensional Heisenberg antiferromagnet. This is the first direct experimental observation of 1-D magnetic behavior in this system. The in-chain superexchange coupling constant, as determined by a fit to the Bonner-Fisher model, is $|J|/k_B \approx 1300 \pm 200$ K, comparable to the values observed in the two dimensional layered cuprates. Estimates of the interchain magnetic interaction indicate that this material may be the best realization of a 1-D spin 1/2 Heisenberg antiferromagnet reported to date. Low temperature neutron and synchrotron x-ray powder diffraction studies of Sr_2CuO_3 indicate that the low temperature structure of this system has Immm space group symmetry, the same structure reported at room temperature, indicating that this material, in contrast to La_2CuO_4, does not undergo any structural transformations upon cooling. The absence of crystallographic distortions precludes a magnetic anisotropy contribution from a Dzyaloshinsky-Moriya interaction, implying that Sr_2CuO_3 should be a nearly ideal spin 1/2 antiferromagnetic Heisenberg chain compound, in agreement with the magnetic susceptibility results. A search for the presence of long range three

dimensional antiferromagnetic order by magnetic neutron powder diffraction at temperatures as low as 1.5 K was not successful, although we estimate an upper limit for the size of the ordered moment which could have been detected to be $\sim 0.1\ \mu_B$ per Cu^{+2} ion.

CHAPTER 6. MAGNETIC PROPERTIES OF Sr_2IrO_4

Interest in spin-$\frac{1}{2}$ two-dimensional Heisenberg antiferromagnets has greatly increased in recent years due to the discovery of high-temperature superconductivity in copper oxides which, in their insulating (undoped) phases, fall into this magnetic category. Although a number of oxides are known with the La_2CuO_4 (K_2NiF_4) structure, no spin-$\frac{1}{2}$ two-dimensional antiferromagnetic oxides other than the cuprates have been thoroughly studied [101]. In order to deepen our understanding of the magnetic properties of the cuprates, and to expand the range of materials which might exhibit high-temperature superconductivity, we are investigating other metal oxides which would be expected to have one unpaired *d* electron per metal ion. Here we describe our results for Sr_2IrO_4.

Sr_2IrO_4, which has the K_2NiF_4 structure, [116] has octahedrally coordinated Ir^{4+} ions. The electronic configuration of the Ir^{4+} ions is $[Xe]4f^{14}5d^5$. Due to the large crystal field and very large spin-orbit coupling, [117] the Ir^{4+} ion should be in the low-spin configuration t_{2g}^5, with the ground state being $^2T_2$. This state is split by spin-orbit coupling and the tetragonal crystal field (see below) into three Kramers doublets. Thus, the ground state for the Ir^{4+} ion in Sr_2IrO_4 is expected to be a spin-$\frac{1}{2}$ Kramers doublet, where the unpaired spin occupies a half-filled d_{xy} band, similar to the situation found for Cu^{2+} in La_2CuO_4. [118]

The sample was prepared by the Dupont group using standard solid-state synthetic techniques. [116] Magnetic susceptibility measurements were made with a Quantum Design SQUID magnetometer at Dupont and our Oxford Instruments Faraday balance. We note that preliminary electrical resistivity measurements indicate that Sr_2IrO_4 is an insulator, although further measurements on single crystals are highly desirable.

In Fig. 6.1(top) we show the temperature dependence of the magnetic susceptibility. There is a distinct magnetic transition at approximately 250 K. In order to clarify the nature of this magnetic transition, in Fig. 6.1(bottom) we show magnetic hysteresis measurements for this sample at a temperature of 5 K. There is a significant magnetic hysteresis, demonstrating that the magnetic structure has a ferromagnetic component. The magnitude of the ferromagnetic moment estimated from these data is far too small (10^{-2} Bohr magnetons per Ir ion) to attribute to full ferromagnetically aligned spin-1/2 Ir^{4+} ions, which should have a magnetic moment of 1.1 Bohr magnetons, perhaps renormalized downward by quantum fluctuations as in La_2CuO_4. Instead it seems more reasonable to attribute the ferromagnetic behavior to canted antiferromagnetism. The magnetic transition we observe is thus probably due to the appearance of long-range three-dimensional antiferromagnetic order of the Ir^{4+} moments. Furthermore, since Ir^{4+} should be a spin-1/2 ion, it has no first order single-ion magnetic anisotropy, and therefore the magnetic properties of Sr_2IrO_4 are expected to be Heisenberg like. If this is so, Sr_2IrO_4 would be, to our knowledge, the second spin-1/2 two-dimensional Heisenberg antiferromagnetic oxide reported (in addition to the layered copper oxides), although the layered vanadates (for example, Sr_2VO_4) may also belong to this category. Moun spin rotation measurements should

be made to verify the magnetic ordering temperature.

Without single-ion anisotropy to cause moment canting, a different origin must be found for the appearance of weak ferromagnetism in this system. The most likely cause is a Dzyloshinsky-Moriya (DM) interaction which arises as a result of the structural distortion. The rotational distortion destroys the inversion center which exists midway between the Ir^{4+} ions along the (100) and (010) directions for I4/mmm symmetry and thereby permits an antisymmetric superexchange term to appear in the spin Hamiltonian due to the DM interaction. A DM interaction also generates canted Cu^{2+} moments as a direct result of the tilting distortion of the CuO_6 octahedra in La_2CuO_4.

The strength of the Dzyaloshinsky-Moriya interaction is proportional to the amount of anisotropy in the Landé g factor, $|D| \sim (\delta g/g)J$, where $\delta g = g - 2$. Since anisotropy of g is a consequence of spin-orbit coupling, and the spin-orbit coupling in Ir^{4+} is large (~ 2000 cm $^{-1}$), it is expected that the Dzyaloshinsky-Moriya interaction in this 5d system is comparable to or larger than that for 3d Cu^{2+} in La_2CuO_4 (spin-orbit coupling ~ 800 cm^{-1}). Furthermore, the relative magnitudes of the rotational distortions of the IrO_6 octahedra in Sr_2IrO_4 ($\sim 11^o$) and the CuO_6 octahedra in La_2CuO_4 ($\sim 3^o$) also lead one to expect a larger DM interaction in the former material. These facts are consistent with our observation of a canted moment in Sr_2IrO_4 one order of magnitude larger than that observed in La_2CuO_4 ($\sim 10^{-3}$ Bohr magnetons).

Fig. 6.1(top) also shows the high-temperature magnetic susceptibility of Sr_2IrO_4. The susceptibility decreases with temperature above the Néel temperature, but not in a fashion consistent with Curie-Weiss behavior. Similar data above the Néel tem-

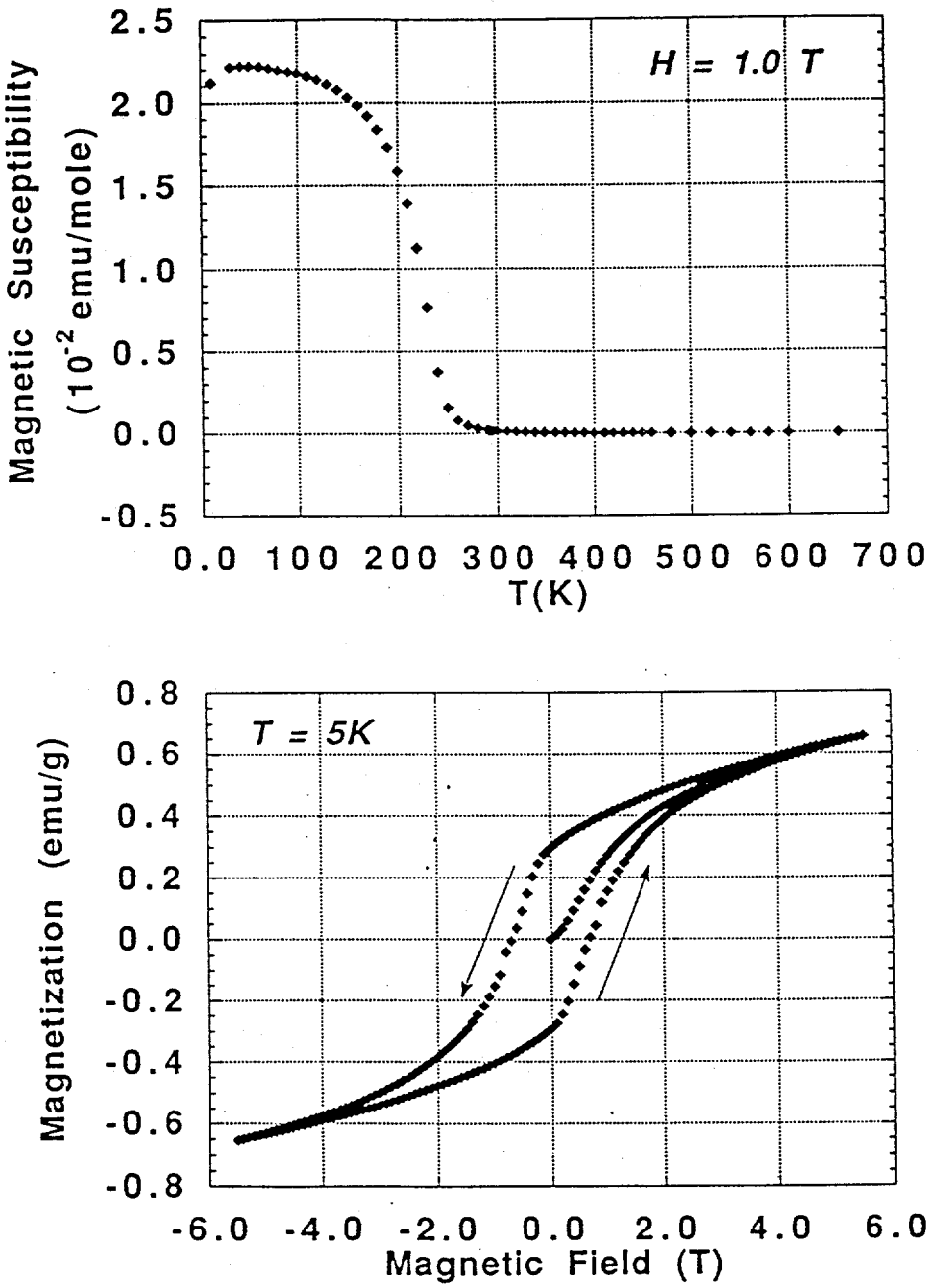

Figure 6.1: (Top) Magnetic susceptibility versus temperature T, data measured with a Faraday balance from 5 to 650 K. (Bottom) Magnetic hysteresis curve measured with a SQUID magnetometer at 5 K. The arrows indicate the direction in which the field is changing.

perature in La_2CuO_4, which also do not follow a Curie-Weiss temperature dependence, were interpreted by a theory which clarified the role of the canted weak ferromagnetism in determining the magnetic properties of that material at temperatures above and below the Néel temperature. However, in contrast to the situation in La_2CuO_4, where the canted moments are antiferromagneticaly aligned in successive layers, our data [Fig. 6.1(top)] indicate that in Sr_2IrO_4 the canted moments in successive layers are ferromagnetically aligned. This is similar to the results reported for $La_{2-x}Nd_xCuO_4$, where low-temperature structural phase transformations induce a magnetic transition from an antiferromagnetic to ferromagnetic interlayer arrangement of the Cu^{2+} spins.

It should be noted that a peak associated with two-dimensional short-range antiferromagnetic order does not appear in the susceptibility data above the Néel temperture in Sr_2IrO_4. Observation of such a peak would demonstrate the two-dimensional nature of this magnetic system, which is expected on the basis of its layered structure and the in-plane superexchange interaction between Ir^{4+} ions. If a peak lies at a temperature above the maximum temperature measured, we can estimate a lower limit for the in-plane magnetic superchange of $J_{ab} \geq 650$ K, a value not quite as large as that of La_2CuO_4 ($J_{ab} \sim 1500$ K). Nevertheless, the magnetic properties of Sr_2IrO_4 have much in common with those of La_2CuO_4 and should offer fertile ground for further comparative study.

In conclusion, Sr_2IrO_4 is a two-dimensional spin-1/2 Heisenberg antiferromagnet. This material, which has a structural distortion which leads to weak ferromagnetism, has much in common with copper-oxide high temperature superconductors and should serve as an important example of this class of low-dimensional antiferro-

magnetic oxides. In particular, study of Sr_2IrO_4 will further our understanding of the delicate connection between structural distortions and magnetism in such materials.

BIBLIOGRAPHY

[1] J. G. Bednorz and K. A. Müller, Z. Phys. B **46**, 189 (1986).

[2] M. K. Wu, J. R. Ashburn, C. J. Torng, P. H. Hor, R. L. Meng, L. Gao, Z. J. Huang, Y. Q. Wang, and C. W. Chu, Phys. Rev. Lett. **58**, 908 (1987); R. J. Cava, B. Batlogg, R. B. van Dover, D. W. Murphy, S. Sunshine, T. Siegrist, J. P. Remeika, E. A. Rietman, S. Zahurak, and G. P. Espinosa, Phys. Rev. Lett. **58**, 1676 (1987).

[3] B. D. Josephson, Phys. Lett. **1**, 251 (1962).

[4] L. D. Landau and E. M. Lifshitz, *Statistical Physics* (Pergamon Press, London, 1958).

[5] V. L. Ginzburg and L. D. Landau, Zh. Eksp. Teor. Fiz. **20**, 1064 (1950).

[6] R. Rajaraman, *An Introduction to Solitons and Instantons in Quantum Field Theory* (North-Holland, New York, 1982).

[7] H. Zijlstra, *Experimental Methods in Magnetism 2*, ed. E. P. Wohlfarth (John Wiley & Sons, New York, 1967), p. 94.

[8] L. Petersson and A. Ehrenberg, Rev. Sci. Instr. **56**, 575 (1985), and references cited.

[9] L. Forró, J. R. Cooper, B. Rothaemel, J. S. Schilling, M. Weger, and K. Bechgaard, Solid State Commun. **60**, 11 (1986).

[10] D. Wohlleben and M. B. Maple, Rev. Sci. Instr. **42**, 1573 (1971), and references cited.

[11] For a review, see D. C. Johnston, J. Magn. Magn. Mater. **100**, 218 (1991).

[12] L. N. Mulay and M. Klemkowsky, *High Temperature Superconductivity. The First Two Years*, ed. R. M. Metzger (Gordon and Breach, New York, 1988), p. 165.

[13] S. A. Shaheen, R. Tucker, and X. Xu, J. Appl. Phys. **73**, 5638 (1993).

[14] W. Mexner and K. Heinemann, Rev. Sci. Instr. **64**, 3336 (1993).

[15] A. Wulfes, Ch. Böttger, J. Hesse, J. Sievert, and H. Ahlers, J. Magn. Magn. Mater. **104**, 2069 (1991); J. Hesse, Ch. Böttger, J. Sievert, and H. Ahlers, Phys. Stat. Sol. (a) **135**, 343 (1993).

[16] R. Srinivasan and S. Usha, J. Phys. E: Sci. Instrum. **19**, 930 (1986).

[17] H. Zhou, Ph. D. Thesis, Univ. of Calif. San Diego (1988).

[18] U. Köbler and F. Deloie, *Design and Operation of a Novel Faraday-magnetometer Using Superconducting Coils*, Oxford Instruments.

[19] A. Roth, *Vacuum Technology* (North-Holland, New York, 1976).

[20] M. Knudsen, Ann. Phys. **31**, 205 (1910); M. Knudsen, Ann. Phys. **32**, 890 (1910); M. Knudsen, Ann. Phys. **33**, 1435 (1910).

[21] *Cryomagnetic System General Operating Procedures*, Oxford Instruments.

[22] L. F. Mattheiss, E. M. Gyorgy, and D. W. Johnson, Jr., Phys. Rev. B **37**, 3745 (1988).

[23] D. G. Hinks, B. Dabrowski, J. D. Jorgensen, A. W. Mitchell, D. R. Richards, and Donglu Shi, *Nature* (London) **333**, 30 (1988); R. J. Cava, B. Batlogg, J. J. Krajewski, R. C. Farrow, L. W. Rupp, Jr., A. E. White, K. T. Short, W. F. Peck, Jr., and T. Y. Kometani, *Nature* (London) **332**, 814 (1988).

[24] D. G. Hinks, D. R. Richards, B. Dabrowski, A. W. Mitchell, J. D. Jorgensen and D. T. Marx, Physica C **156**, 447 (1988).

[25] B. Batlogg, R. J. Cava, L. W. Rupp, Jr., A. M. Mujsce, J. J. Krajeski, J. P. Remeika, W. F. Peck, Jr., A. S. Cooper, and G. P. Espinosa, Phys. Rev. Lett. **14**, 1670 (1988).

[26] J. F. Zasadzinski, N. Tralshawala, D. G. Hinks, B. Dabrowski, A. W. Mitchell, and D. R. Richards, Physica C **156**, 519 (1989).

[27] L. Krusin-Elbaum, R. L. Greene, F. Holtzberg, A. P. Malozemoff, and Y. Yeshurun, Phys. Rev. Lett. **62**, 217 (1989).

[28] Sreeparna Mitra, J. H. Cho, W. C. Lee, D. C. Johnston, and V. G. Kogan, Phys. Rev. B **40**, 2674 (1989).

[29] Y. J. Uemura, V. J. Emery, A. R. Moodenbaugh, M. Suenaga, D. C. Johnston, A. J. Jacobson, J. T. Lewandowski, J. H. Brewer, R. F. Kiefl, S. R. Kreitzman, G. M. Luke, T. Riseman, and C. E. Stronach, Phys. Rev. Lett. **62**, 2317 (1989).

[30] G. Aeppli, R. J. Cava, E. J. Ansaldo, J. H. Brewer, S. R. Kreitzman, G. M. Luke, D. R. Noakes, and R. F. Kiefl, Phys. Rev. B **35**, 7129 (1987).

[31] F. N. Gygax, B. Hitti, E. Lippelt, A. Schenck, D. Cattani, J. Cors, M. Decroux, Ø. Fischer, and S. Barth, Europhys. Lett. 4, 473 (1987).

[32] D. R. Harshman, G. Aeppli, E. J. Ansaldo, B. Batlogg, J. H. Brewer, J. F. Caeolan, R. J. Cava, and M. Celio, Phys. Rev. B **36**, 2386 (1987).

[33] W. J. Kossler, J. R. Kempton, X. H. Yu, H. E. Schone, Y. J. Uemura, A. R. Moodenbaugh, M. Suenaga, and C. E. Stronach, Phys. Rev. B **35**, 7133 (1987).

[34] R. F. Kiefl, T. M. Riseman, G. Aeppli, E. J. Ansado, J. F. Carolan, R. J. Cava, W. N. Hardy, D. R. Harshman, N. Kaplan, J. R. Kempton, S. R. Kreitzman, G. M. Luke, B. X. Yang, and D. L. Williams, Physica C **143**, 757 (1988).

[35] P. Birrer, J. E. Schirber, B. Morosin, and D. S. Ginley, Physica C **158**, 230 (1989).

[36] Z. D. Hao, J. Clem, M. W. McElfresh, L. Civale, A. P. Malozemoff, and F. Holtzberg, Phys. Rev. B **43**, 2844 (1991).

[37] S. Pei, J. D. Jorgensen, B. Dabrowski, D. G. Hinks, D. G. Richards, A. W. Mitchell, J. M. Newsam, S. K. Sinha, D. Vaknin, and A. J. Jacobson, Phys. Rev. B **41**, 4126 (1990).

[38] E. H. Brandt, Phys. Rev. B **37**, 2349 (1988).

[39] D. R. Harshman, L. F. Schneemeyer, J. V. Waszczak, G. Aeppli, R. J. Cava, B. Batlogg, L. W. Rupp, E. J. Ansaldo, and D. L. Williams, Phys. Rev. B **39**, 851 (1989).

[40] For a review, see Y. J. Uemura, J. Appl. Phys. **64**, 6088 (1988).

[41] Y. J. Uemura, B. J. Sternlieb, D. E. Cox, J. H. Kempton, R. F. Kiefl, S. R. Kreitzman, G. M. Luke, P. Mulhern, T. Riseman, D. L. Williams, W. J. Kossler, X. H. Yu, C. E. Stronach, M. A. Subramanian, J. Gopalakrishnan, and A. W. Sleight, *Nature* **335**, 151 (1988).

[42] U. Welp, W. K. Kwok, G. W. Crabtree, H. Claus, K. G. Vandervoort, B. Dabrowski, A. W. Mitchell, D. R. Richards, D. T. Marx, and D. G. Hinks, Physica C **156**, 27 (1988).

[43] Y. J. Uemura, L. P. Le, G. M. Luke, B. J. Sternlieb, W. D. Wu, J. H. Brewer, T. M. Riseman, C. L. Seaman, M. B. Maple, M. Ishikawa, D. G. Hinks, J. D. Jorgensen, G. Saito, and H. Yamauchi, Phys. Rev. Lett. **66**, 2665 (1991).

[44] T. A. Vanderah, editor, *Chemistry of Superconductor Materials* (Noyes, Park Ridge, NJ, 1992).

[45] D. Vaknin, S. K. Sinha, D. E. Moncton, D. C. Johnston, J. M. Newsam, C. R. Safinya, and H. E. King, Jr., Phys. Rev. Lett. **58**, 2802 (1987).

[46] G. Shirane, R. J. Birgeneau, Y. Endoh, P. Gehring, M. A. Kastner, K. Kitazawa, H. Kojima, I. Tanaka, T. R. Thurston, and K. Yamada, Phys. Rev. Lett. **63**, 330 (1989).

[47] For a review, see R. J. Birgeneau and G. Shirane, in *Physical Properties of High Temperature Superconductors I*, ed. D. M. Ginsberg (World Scientific, Singapore, 1989), p. 151.

[48] G. Shirane, Y. Endoh, R. J. Birgeneau, M. A. Kastner, Y. Hidaka, M. Oda, M. Suzuki, and T. Murakami, Phys. Rev. Lett. **59**, 1613 (1991).

[49] P. W. Anderson, Science **235**, 1196 (1987); J. R. Schrieffer, X.-G. Wen, and S.-C. Zhang, Phys. Rev. Lett. **60**, 944 (1988); D. J. Scalapino, J. Phys. Chem. Solids **54**, 10 (1993); P. Monthoux and D. Pines, Phys. Rev. B **49**, 4261 (1994).

[50] P. W. Anderson, Phys. Rev. **79**, 350 (1950).

[51] J. B. Goodenough, *Magnetism and the Chemical Bond* (Interscience, New York, 1963).

[52] A. Aharony, R. J. Birgeneau, A. Coniglio, M. A. Kastner, and H. E. Stanley, Phys. Rev. Lett. **60**, 1330 (1988).

[53] D. Klemm, M. Letz, E. Sigmund, and G. S. Zavt, Phys. Rev. B **50**, 7046 (1994), and references cited.

[54] B. Büchner, M. Breuer, A. Freimuth, and A. P. Kampf, Phys. Rev. Lett. **73**, 1841 (1994).

[55] F. Mizuno, H. Masuda, I. Hirabayashi, S. Tanaka, M. Hasegawa, and U. Mizutani, Nature **345**, 788 (1990); H. Masuda, F. Mizuno, I. Hirabayashi, and S. Tanaka, Phys. Rev. B **43**, 7871 (1991).

[56] F. Sapiña, J. Rodriguez-Carvajal, M. J. Sanchis, R. Ibáñez, A. Beltrán, and D. Beltrán, Solid State Commun. **74**, 779 (1990).

[57] K. Seedhar and P. Ganguly, Inorg. Chem. **27**, 2261 (1988).

[58] K. Okuda, S. Noguchi, K. Konishi, H. Deguchi, and K. Takeda, J. Magn. Magn. Mater. **104-107**, 817 (1992).

[59] R. Hoffman, R. Hoppe, and W. Schäfer, Z. Anorg. Allg. Chem. **578**, 18 (1989).

[60] R. Kipka and Hk. Müller-Buschbaum, Z. Naturforsh. **32b**, 121 (1977); for a review, see Hk. Müller-Buschbaum, Angew. Chem. Int. Ed. Engl. **16**, 674 (1977).

[61] M. T. Weller and D. R. Lines, J. Solid State Chem. **82**, 21 (1989).

[62] E. F. Paulus, G. Miehe, H. Fuess, I. Yehia, and U. Lochner, J. Solid State Chem. **90**, 17 (1991).

[63] M. A. G. Aranda and J. P. Attfield, unpublished.

[64] S. Eriksson, L. Johansson, L. Borjesson, and M. Kakihana, Physica C **162-164**, 59 (1989).

[65] For a review, see W. Wong-Ng and R. S. Roth, Physica C (to be published).

[66] X.-L. Wang, J. A. Fernandez-Baca, Z. R. Wang, D. Vaknin, and D. C. Johnston, unpublished.

[67] D. Eckert, A. Junod, T. Graf, and J. Muller, Physica C **153**, 1038 (1988); for a review, see R. A. Fisher, J. E. Gordon, and N. E. Phillips, J. Supercond. **1**, 231 (1988).

[68] H. N. Migeon, F. Jeannot, M. Zanne, and J. Aubry, Rev. Chim. Min. **13**, 440 (1976); H. N. Migeon, M. Zanne, F. Jeannot, and C. Gleitzer, Rev. Chim. Min. **14**, 498 (1977).

[69] M. Wu, Q. Su, G. Hu, Y. Ren, and H. Wang, J. Solid State Chem. **110**, 389 (1994).

[70] D. C. Vier, S. B. Oseroff, C. T. Salling, J. F. Smyth, S. Schultz, Y. Dalichouch, B. W. Lee, M. B. Maple, Z. Fisk, and J. D. Thompson, Phys. Rev. **B 36**, 8888 (1987).

[71] R. N. de Mesquita, J. H. Castilho, G. E. Barberis, C. Rettori, I. Torriani, M. C. Terrile, H. Basso, and O. R. Nascimento, Phys. Rev. B **39**, 6694 (1989).

[72] S. Petricek, N. Bukovec, and P. Bukovec, J. Solid State Chem. **99**, 58 (1992).

[73] D. Vaknin, unpublished results.

[74] Z.-R. Wang, X.-L. Wang, J. A. Fernandez-Baca, D. C. Johnston, and D. Vaknin, Science **264**, 402 (1994).

[75] P. W. Selwood, *Magnetochemistry*, 2^{nd} edition (Interscience, New York, 1956), p. 78.

[76] D. C. Johnston, T. Matsumoto, Y. Yamaguchi, Y. Hidaka, and T. Morakami, in *Electronic Properties and Mechanisms of High Temperature Superconductors*, edited by T. Oguchi, K. Kadowaki and T. Sasaki (Elsevier, Amsterdam, 1992), p. 301.

[77] A. Bino, D. C. Johnston, D. P. Goshorn, T. R. Halbert, and E. I. Stiefel, Science **241**, 1479 (1988).

[78] C. Kittel, *Introduction to Solid State Physics*, 6th edition (Wiley, New York, 1986).

[79] J. C. Bonner and M. E. Fisher, Phys. Rev. **135**, A640 (1964).

[80] J. H. Van Vleck, *Theory of Electric and Magnetic Susceptibilities* (Oxford University Press, London, 1965).

[81] D. Gotteschi, A. Caneschi, L. Pardi, and R. Sessoli, Science **265**, 1054 (1994), and references cited.

[82] R. Gottschall and R. Schöllhorn, Solid State Ionics **59**, 93 (1993).

[83] G. Shirane, Acta. Cryst. **12**, 282 (1985).

[84] A. H. Morrish, *The Physical Principles of Magnetism* (John Willey & Sons, New York, 1965).

[85] Z. Hiroi, M. Takano, M. Azuma, and Y. Takeda, Nature **364**, 315 (1993).

[86] Chr. L. Teske and Hk. Muller-Büschbaum, Z. Anorg. Allg. Chem. **371**, 325 (1969).

[87] The diffractometer was operated in the high resolution mode described by D. E. Cox, B. H. Toby, and M. M. Eddy, J. Phys. **41**, 117 (1988).

[88] Y. J. Shin, E. D. Manova, J. M. Dance, P. Dordor, J.-C. Grenier, E. Marquestaut, J. P. Doumerc, M. Pouchard, and P. Hagenmuller, Z. Anorg. Allg. Chem. **616**, 201 (1992).

[89] S. Kondoh, K. Fukuda, and M. Sato, Solid State Commun. **65**, 1163 (1988).

[90] A. Keren, L. P. Le, G. M. Luke, B. J. Sternlieb, W. D. Wu, Y. J. Uemura, S. Tajima, and S. Uchida, Phys. Rev. B **48**, 12926 (1993).

[91] M. T. Weller and D. R. Lines, J. Solid State Chem. **82**, 21 (1989).

[92] Ch. Kruger, W. Reichelt, A. Almes, U. Konig, H. Oppermann, and H. Scheler, J. Solid State Chem. **96**, 67 (1992); D. R. Lines, M. T. Weller, D. B. Currie and D. M. Osborne, Mater. Res. Bull. **26**, 323 (1991).

[93] I. Dzyaloshinsky, J. Phys. Chem. Solids **4**, 241 (1958); T. Moriya, Phys. Rev. **120**, 91 (1960); T. Moriya, in *Magnetism*, edited by G. T. Rado and H. Suhl (Academic, New York, 1963), Vol. I, Chap. 3.

[94] Structural refinements were made using the GSAS software package [A. C. Larsen and R. B. von Dreele, LANCE, Los Alamos National Laboratory (1990)].

[95] D. Vaknin, S. K. Sinha, D. E. Moncton, D. C. Johnston, J. M. Newsam, C. R. Safinya, and H. E. King, Jr., Phys. Rev. Lett. **58**, 2802 (1987); B. X. Yang, S. Mitsuda, G. Shirane, Y. Yamaguchi, H. Yamauchi, and Y. Syono, J. Phys. Soc. Jpn. **56**, 2283 (1987).

[96] G. Aeppli and D. J. Buttrey, Phys. Rev. Lett. **61**, 203 (1988).

[97] D. E. Cox, G. Shirane, R. J. Birgeneau, and J. B. MacChesney, Phys. Rev. **188**, 930 (1969).

[98] M. T. Hutchings, E. J. Samuelsen, G. Shirane, and K. Hirakawa, Phys. Rev. **188**, 919 (1969).

[99] L. J. De Jongh and A. R. Miedema, Adv. Phys. **23**, 1 (1974); M. Steiner, J. Villain, and C. G. Windsor, ibid. **25**, 87 (1976).

[100] T. Thio, T. R. Thurston, N. W. Preyer, P. J. Picone, M. A. Kastner, H. P. Jenssen, D. R. Gabbe, M. Sato, K. Fukuda, S. Shamoto, Y. Endoh, K. Yamada, and G. Shirane, Phys. Rev. B **38**, 905 (1988).

[101] R. J. Birgeneau and G. Shirane, in *Physical Properties of High Temperature Superconductors I*, edited by D. M. Ginsberg (World Scientific, Singapore, 1989), Ch. 3.

[102] E. A. Boudreaux and L. N. Mulay, *Theory and Applications of Molecular Paramagnetism* (Wiley, New York, 1976), p. 494.

[103] R. L. Carlin, *Magnetochemistry* (Springer-Verlag, Berlin, 1986).

[104] W. E. Estes, D. P. Gavel, W. E. Hatfield, and D. J. Godjson, Inorg. Chem. **17**, 1415 (1978).

[105] H. Ohta, N. Yamauchi, M. Motokawa, M. Azuma and M. Takano, J. Phys. Soc. Jpn. **61**, 3370 (1992).

[106] C. Allgeier and J. S. Schilling, Phys. Rev. B **48**, 9747 (1993).

[107] C. J. Glinka, V. J. Minkiewicz, D. E. Cox, and C. P. Khatak, AIP Conf. Proc. **10**, 659 (1972); M. Eibschutz, R. C. Sterwood, F. S. L. Hsu, and D. E. Cox, AIP Conf. Proc. **10**, 684 (1972).

[108] S. K. Satija, J. D. Axe, G. Shirane, H. Yoshizawa, and K. Hirakawa, Phys. Rev. B **21**, 2001 (1980).

[109] D. Vaknin, S. K. Sinha, C. Stassis, L. L. Miller, and D. C. Johnston, Phys. Rev. B **41**, 1926 (1990).

[110] T. Oguchi, Phys. Rev. **133**, A1098 (1964).

[111] E. Montroll, *Proc. Third Berkeley Symp. on Mathematical Statistics and Probability* (University of California Press, Berkeley, CA, 1956), Vol. 3.

[112] M. J. Hennessy, C. D. McElwee, and P. M. Richards, Phys. Rev. B **7**, 930 (1973).

[113] M. Hase, I. Terasaki, and K. Uchinokura, Phys. Rev. Lett. **70**, 3651 (1993).

[114] P. Laffez, S. Adachi, H. Yamauchi, and N. Mori, in Proc. Int. Conf. "Superconducting Materials" (ICMAS-93), edited by J. Etourneau, J. B. Torrance, and H. Yamauchi (IITT International, Paris, 1993).

[115] T. Ami and M. K. Crawford, unpublished data.

[116] J. J. Randall, L. Katz, and R. Ward, J. Am. Chem. Soc. **79**, 266 (1957).

[117] K. W. H. Stevens, Proc. Royal Soc. London, Ser. A **219**, 542 (1954).

[118] It should be noted that the unpaired spin for Cu^{2+} resides in an e_g $3d$ orbital $(d_{x^2-y^2})$.

[119] D. E. Cox, B. H. Toby, and M. M. Eddy, Aust. J. Phys. **41**, 117 (1988).